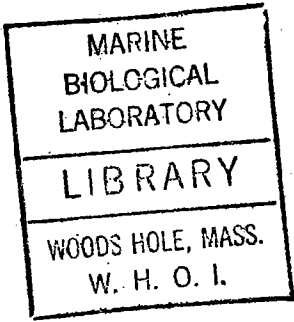


GC  
7.1  
I54  
1971

EXPERIMENTS IN A ROTATING SOURCE-SINK ANNULUS



by

RICHARD GRANT INGRAM

B.S., McGill University  
(1965)

M.S., McGill University  
(1967)

SUBMITTED IN PARTIAL FULFILLMENT OF THE  
REQUIREMENTS FOR THE DEGREE OF  
DOCTOR OF PHILOSOPHY

at the

MASSACHUSETTS INSTITUTE OF TECHNOLOGY

and the

WOODS HOLE OCEANOGRAPHIC INSTITUTION

August, 1971

Signature of Author

*Richard Grant Ingram*

Joint Program in Oceanography, Massachusetts  
Institute of Technology - Woods Hole Oceanographic  
Institution, Department of Earth and  
Planetary Sciences, and Department of Meteorology,  
Massachusetts Institute of Technology,  
August, 1971

Certified by

*Erik Mollo - Director*

Thesis Supervisor

Accepted by

*Norman A Phillips*

Chairman, Joint Oceanography Committee in the  
Earth Sciences, Massachusetts Institute of  
Technology - Woods Hole Oceanographic Institution

Lindgren



# EXPERIMENTS IN A ROTATING SOURCE-SINK ANNULUS

by

Richard Grant Ingram

Submitted to the Joint Oceanographic Committee in the Earth Sciences, Massachusetts Institute of Technology and Woods Hole Oceanographic Institution, on August 16, 1971, in partial fulfillment of the requirements for the degree of Doctor of Philosophy.

## ABSTRACT

An experimental investigation of the different flow regimes in a rotating source-sink annulus is described. Both the steady and transient velocities are measured over a large range of Ekman Reynolds number and Rossby number. Differing probe configurations are used to investigate the corresponding motions in spatially separated regions of the annulus.

The steady interior circulation field exhibits a strong dependence on the imposed flux values. The non-dimensional circulation increases with radius over a certain radial range for higher system Rossby number. The observed profile changes are related to the existence of an unstable Ekman layer at some inner radial position.

The thickness of the observed Ekman layers is typically 85% of the theoretical scale height. For higher local Reynolds number ( $Re_L$ ), the thickness is generally much smaller. The width of the sidewall boundary layer adjacent to the sink increases with larger system Rossby number. Adjacent to the source, the radial boundary layer is wider than that at the sink wall.

Observed oscillations are separable into three types. For  $Re_L > 50$ , instability waves are observed in the Ekman layer flow. In the same  $Re_L$  range, inertial oscillations are detected in the interior region of the annulus. The observed inertial wave frequency at differing radial positions is explained by incorporating Doppler shift corrections and taking account of the steady circulation profiles. The radial wavelength of the inertial waves corresponds to the length of the Class A Ekman layer instability. For small values of  $Re_L$  and local Rossby number, an axisymmetric disturbance, with a characteristic frequency slightly greater than the rotation rate, is observed at the outer radial positions.

Thesis Supervisor: Erik Mollo-Christensen  
Title: Professor of Meteorology

## ACKNOWLEDGEMENTS

The author would like to express appreciation to his advisor, Professor Erik Mollo-Christensen, for many interesting discussions and insights into this work.

He would also like to acknowledge the technical help offered by Ken Morey with the electronics and by Ed Bean with the machine work.

The long hours of typing by Susan Berson in the final days were instrumental in completing the thesis. Most thanks must go to my wife, Bea, who drafted most of the diagrams and provided undying encouragement at every step in the final hectic days.

During his four years at M.I.T., the author and his work was supported by a grant from the National Science Foundation.

## TABLE OF CONTENTS

		<u>Page</u>
	ABSTRACT	2
	ACKNOWLEDGEMENT	3
I.	INTRODUCTION	9
II.	BACKGROUND LITERATURE	13
III.	EXPERIMENTAL EQUIPMENT	24
	3.1. The Rotating Annulus	24
	3.2. New Techniques	24
IV.	MEAN VELOCITY STRUCTURE IN THE ANNULUS	30
	4.1. Radial Structure of Vertically Independent Flows	30
	4.1.1 Theoretical Predictions	30
	4.1.2 Observed Velocity and Circulation Profiles	31
	4.1.3 Comparison and Discussion	32
	4.2. Vertical Structure of Velocity Adjacent to Horizontal Boundaries	52
	4.2.1 Theoretical Predictions	52
	4.2.2 Observed Vertical Structure	55
	4.2.3 Discussion	62
	4.3. Summary of Mean Conditions	67
V.	WAVE AND INSTABILITY PHENOMENA	69
	5.1. General Oscillatory Activity	69
	5.1.1 Wave Intensity in the Interior and Side-Wall Regions	70
	5.1.2 Variation of Wave Amplitude with Height in the Ekman Layer	70

5.2.	Wave Spectra	72
5.2.1	Introduction	72
5.2.2	Spectra Distortion and Hysteresis	78
5.3.	The "Body-Boundary" Modes	81
5.4.	A series of Representative Spectra of Velocity Fluctuations	89
5.5.	Wave Spectra within the Ekman Layer and Related Interior Motion	104
5.5.1	Reynolds Number Dependence of Ekman Layer Spectra	104
5.5.2	Comparison of Interior and Ekman Layer Spectral Results	123
5.6.	Measurements of Azimuthal Wave Number by Cross-Correlation	126
VI.	DISCUSSION	132
6.1.	Interior Circulation Profile	133
6.2.	Low Reynolds Number Waves at Outer Radii	134
6.3.	Inertial Oscillations	136
6.4.	Boundary Layers	137
6.5.	Flows in a Rotating Source-Sink Annulus	138
6.6.	Geophysical Relevance	140
6.7.	Future Work	141
APPENDIX I	Experimental Set-Up and Methods	143
APPENDIX II	Data Collection Methods	154
APPENDIX III	Wall Proximity Effects	162
APPENDIX IV	Transient Response Times	164
BIBLIOGRAPHY		166
BIOGRAPHICAL SKETCH		170

## LIST OF FIGURES

<u>Figure</u>		<u>Page</u>
2.1	Horizontal Cross Section of Annulus	14
2.2	Idealized Flow Pattern	15
3.1	Rotating Tank	25
3.2	Schematic of Circuitry	26
4.1	Zonal Velocity Profiles	33
4.2 - .11	Circulation Profiles (10 parts)	34
4.12	Comparison of Circulation Profiles	45
4.13	Technique of Locating Side-Wall Boundary Layer	50
4.14	Theoretical Steady Ekman Layer Profile	54
4.15	Non-Linear Modification of Ekman Layer	5
4.16A	Ekman Layer Profile, R = 18.5", Zonal	56
4.16B	Ekman Layer Profile, R = 21.6", Zonal	57
4.17A	Ekman Layer Profile, R = 4.63", Radial	58
4.17B	Ekman Layer Profile, R = 4.63", Zonal	59
4.18A	Ekman Layer Profile, R = 6.00", Radial	60
4.18B	Ekman Layer Profile, R = 6.00", Zonal	61
5.1	Hysteresis Effects	80
5.2	Hot Wire Voltage Output Showing Hysteresis Effects	82
5.3	Spectral Representation of Low Reynolds Number Waves	85
5.4	Observed Low Reynolds Number Waves	86
5.5	Spectral Output, R = 7.07"	91
5.6	Spectral Output, R = 9.57"	92
5.7	Spectral Output, R = 13.80"	93
5.8	Spectral Output, R = 15.45"	94

LIST OF FIGURES (Cont.)

<u>Figure</u>		<u>Page</u>
5.9	Spectral Output, $R = 17.80''$	95
5.10	Spectral Output, $R = 19.82''$	96
5.11	Spectral Output, $R = 13.80$ , $z = 0.10$ cm	97
5.12	Spectral Output for Constant Flux, 1725 cc/sec	98
5.13	Combined Spectral Results vs System Rossby Number	100
5.14	Observed Frequency vs $\epsilon_L$	103
5.16A	Low Reynolds Number Ekman Layer Spectra	107
5.16B	Low Reynolds Number Ekman Layer Spectra	108
5.17	Hot Wire Voltage Output	110
5.18	Expanded Time Scale (High Re)	111
5.19	Ekman Layer Spectra, $R = 6.00''$	112
5.20	Ekman Layer Spectra, $R = 6.00''$	114
5.21	Ekman Layer Spectra, $R = 4.50''$	115
5.22	Ekman Layer Spectra, $R = 4.50''$	116
5.23	Critical Reynolds Number vs Rossby Number for Ekman Layer Instabilities (Tatro)	118
5.24	Critical Reynolds Number vs Rossby Number for Ekman Layer Instabilities (Caldwell & van Atta)	119
5.25	Ekman Layer Spectra (Caldwell & van Atta)	121
5.26	Ekman Layer Spectra for High Reynolds Number Flow	122
5.27A	Interior and Ekman Layer Spectral Comparison	124
5.27B	Interior and Ekman Layer Spectral Comparison	125
5.28	Auto-Spectra of Probe Outputs During Cross-Correlation Measurements: Ekman Layer	128
5.29	Cross-Correlation Configuration: Vertical Separation	129

LIST OF FIGURES (Cont.)

<u>Figure</u>	<u>Page</u>
App. I.1. - Probe Designs	146
App. I.2. - Probe Mobility	147
App. I.3. - High Velocity Wind Tunnel	150
App. I.4. - Low Velocity Wind Tunnel	151



## CHAPTER I

## Introduction

The motions observed in both the seas and the atmosphere exhibit a wide range of scales, and are found to depend on an interplay of many factors. In order to avoid an inordinate degree of complexity most investigators isolate a single process to study in detail. The synthesis of independent works may then bring greater understanding to the overall picture. The present work will focus on mean geostrophic flows, the inherent boundary layers, and the structure of waves emitted into the interior through the use of a laboratory model. Concurrent characteristics of stratification and turbulence, found in nature, will not be examined. As with most laboratory simulations of a geophysical process, the model itself evolves peripheral problems, which, in the opinion of the present writer, are interesting in themselves, but seemingly have little relevance to the original phenomena. The aim remains throughout, to relate the experimental findings to analogous geophysical effects.

The structure of the boundary layers formed at the air-sea interface and the ocean's bottom was first described theoretically by Ekman (1905). This important work showed the significant role played by the earth's rotation in influencing large scale ocean circulation. It was also in Ekman's paper that the existence of a skewed boundary layer of uniform thickness at the ocean's top and bottom was postulated. These boundary layers, which result from a balance of viscous and Coriolis forces, are known as "Ekman layers". Ekman also found that the transient response of a rotating system to a change in forcing was the generation of inertial waves in the interior portion of the flow. This concept resembles earlier theories of Kelvin (1880).

Since Ekman's time, the concept of a steady Ekman layer has been used as a tool in explaining many of the features observed in oceanic phenomena. In general, the observational evidence showing the existence of such layers on a local scale has been difficult to come by. There is little doubt that a skewed boundary layer exists; Brennecke (1921) in the Weddell Sea, and Swallow and Bruce (1966) in the area of the Somali current have both observed it. More recently, Gonella (1968) found a clearly defined Ekman-like spiral in the wind mixed layer, at large wind speeds from a fixed buoy in the Mediterranean. The discrepancies usually arise in the comparison of vertical structure, with the actual spiral showing only a slight resemblance to theory. The reasons why this lack exists is readily found in the nature of the driving forces - such as the wind, the spectra of which usually shows most of its energy at frequencies much higher than that of inertial (Ingram, 1967). To date, Hunkin's (1966) observations under Drift Station Alpha in the Arctic Ocean, provide the best fit between nature and classical theory; whereby the massive inertia of the ice island damps out smaller scale transients, so that the forcing appears quasi-steady.

The inertial oscillations mentioned by Ekman and others were unobserved in the open oceans for many years. However, their existence has been detected in smaller seas (Gustafson & Kullenberg, 1933). Only in the last decade has a large amount of information been compiled about their structure in the deep ocean, resulting mainly from the implementation of long term moored current meters. Hunkins (1966), Knauss (1964), Webster (1963), Day and Webster (1965), and Pollard and Millard (1970) are amongst those who have both observed, and in some cases, attempted to explain the amplitude and spatial coherence of these motions.

During the last three decades, experimental and theoretical work on

"laboratory" Ekman layers has been advancing at a rate chronologically similar to the observational program. Two models have been used; a rotating disk in still air, and a rotating annulus with an axisymmetric peripheral source and sink.

The annular configuration produces an interior potential vortex bounded by non-divergent Ekman layers on the horizontal solid boundaries. It was hypothesized that in such an experimental set-up, both the steady and unsteady boundary layers could be observed, and perhaps, the dynamical features could be compared to analogous structure in nature. However, the experimental and natural environments differ substantially in their viscous properties. Since in the laboratory, the viscous action is predominantly of a laminar form, whereas in the sea, "turbulent eddy" viscosity dominates. Furthermore, stratification, which plays a significant role in the ocean, is a difficult parameter to model experimentally in a source sink annulus.

Using a source sink annulus, as indicated above, it is possible to study the transfer of energy from boundary layers to the interior. This energy transfer is accomplished by the Reynolds stresses generated through instabilities of the Ekman layer. The occurrence of these instabilities has been studied (Faller, 1963), and found to be the function of the Ekman layer, rotational Reynolds number. Since a mechanism exists for exciting interior wave motions it would seem appropriate to inquire if analogous oceanic phenomena may be explained similarly. The energies produced by similar dynamics in the ocean are small when compared to the competing mechanisms; nevertheless, their contribution may be important under optimum conditions (see Faller [1963]).

Early annulus experimenters, employing mainly dye techniques in water were able to observe qualitative features of the steady flow and some quasi-steady disturbances. In most cases, these experiments employed equipment having a free surface. More recently a quantitative approach has been used in annuli having a rigid top and bottom. These latter findings have introduced many more queries as to the dynamics of source sink annulus flows. Until the underlying physics is explained, it is difficult to compare experimental results to geophysical observations. With this in mind, the present work is an attempt to both observe and explain the transient and steady motions in all regions of the annulus.

The study of vortices is not a new one to M.I.T., as in the 1860's, William Barton Rogers, founder of the school, was involved in this work and published a paper in the field. With such an ancestry, it is appropriate that some of the above aims should be furthered at this institution.

## CHAPTER II

## Background Literature

The experimental work done previously in the field of Ekman layer instabilities has followed two paths, both from a configurational and a chronological sense. Earlier work, which resulted from an interest in the dynamics of flow over a delta wing and quickly rotating objects, focused on the motions produced by a disk rotating in still air. Later, source-sink rotating annuli, with the sink located peripherally on the inner cylinder and the source likewise on the outer wall, were used to study laminar Ekman layers and their inherent instabilities:

The early experiments in rotating boundary layers were those of Theodorsen and Regier (1944), using a fixed hot wire anemometer probe located over a rotating disk in air. They found a transition Reynolds number for the boundary flow at which sinusoidal oscillations were generated. In a similar manner, Smith (1945) made hot wire anemometer measurements over a rotating disk, but at different radii and with a double probe. He found a range of critical Reynolds number, for instability onset, slightly lower, but comparable to the values of Theodorsen and Regier. Using the double probe, Smith was able to measure the phase velocity and orientation of the disturbances. It was found that they propagated inward at an angle of  $14^\circ$  from the azimuthal direction with a speed of order 0.2 of the azimuthal velocity. Although the results shown are similar to those depicted by Tatro (1966), the instability structure Smith found has characteristics of both the Class A and B waves mentioned by Greenspan (1968, sect. 6.3).

Later, Gregory, Stuart and Walker (1955) studied the onset of boundary layer instabilities using two techniques: china clay streaks and a sonic probe. In this paper, Stuart solved the inviscid stability problem for a rotating disk, by postulating that the instability was centered near the inflection point in the vertical velocity profile. He indicated that the instabilities took the form of a series of horizontal roll vortices in spiral bands and whose velocity, orientation and spacing were predictable theoretically. But for the lateral spacing, his results were well matched with experimental evidence.

The china clay techniques of observation allowed Gregory and Walker to view the disturbances as a group of equiangular spiral vortices distributed azimuthally on the disk, which would alternately provide regions of convergence and divergence. The critical Reynolds number ( $Re^1 = \frac{\Omega r \delta}{\nu} = \frac{r}{\delta}$ , where  $\delta$  = Ekman layer depth) was found to be 435, lower than those reported by previous workers. In another series of experiments, using a sonic probe to sense small pressure fluctuations, they obtained a range of 408 to 445 for the critical Reynolds number and a series of spectra showing a prevalence of rotation rate harmonics.

More recently, the path chosen by both theorists and experimenters has been a study of rotating source-sink annuli as seen in figure 2.1

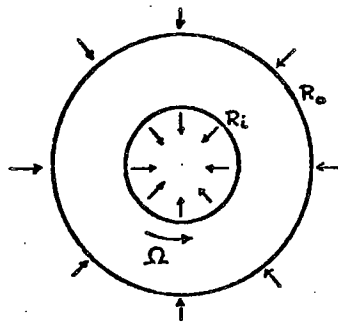


Figure 2.1. Horizontal cross-section of annulus, showing imposed mass flux through vertical walls.

The rationale for choosing this container is readily seen in the resulting flows. To ascertain the nature of these flows, we assume a geometry as shown in fig. 2.1, with the horizontal top and bottom walls separated by a distance  $H$ , and a constant flux  $Q$  imposed radially inward. Scaling velocity by  $\frac{Q}{2\pi R_i H}$ , where  $R_i$  = inner wall radius, and with axial symmetry, the dimensionless linear equations of motion in cylindrical coordinates (Greenspan [1968] sect. 1.2 and 2.3; also Lewellen [1965]) yields an interior azimuthal velocity proportional to  $1/r E^{1/2}$  (where  $r$  = radius and  $E = \nu/\Omega H^2$ ) and zero interior radial and vertical velocities. The resulting potential vortex is adjusted at the top and bottom walls by non-divergent Ekman layers, their passivity resulting from the zero vorticity interior. The radial flow takes place solely through the Ekman layers, similar to that shown in fig. 2.2 (Lewellen [1965]). The radial adjustment of the zonal velocity field near the source and sink areas is accomplished by the side wall boundary layers (Stewartson [1957]). From fig. 2.2 one sees that the flux transported through the Ekman layer is a convergent flow with its velocity increasing proportionally to the reciprocal of the radius. Defining an Ekman layer Reynolds number  $Re = \frac{U\delta}{\nu}$  (as previously defined), the value of which increases with decreasing radius, the possibility of  $Re$  reaching sufficient size as to produce

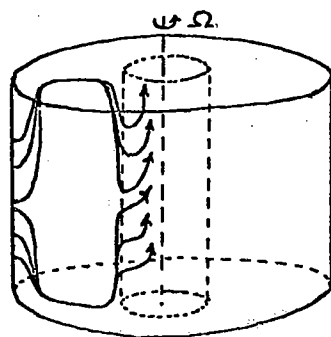


Figure 2.2  
Idealized Flow Pattern

an instability at some inner radius becomes realizable. Due mainly to the simplicity of these relations and the freedom of parameter choice, much attention was turned to annular models.

Stern (1960) first looked at the instability of laminar Ekman layers in a source sink annulus having a free surface (the rotational Froude number was assumed small as compared to unity). His analysis was mainly of a theoretical nature, although some crude experiments were performed. The occurrence of some "body-boundary" modes of instability, as he named them, was dependent on a critical Taylor ( $Ta = \frac{\Omega H^2}{\nu}$ ) and assumed to result from a shear instability which drew its energy from a coupling with the ageostrophic perturbation velocity. These waves differ from the "pure boundary" species (Faller [1963]), as they are found throughout the interior of the fluid. Stern found a lower limit of  $Ta$  equal to 2500 (and a  $Re$  of not more than 80) for the lowest mode. Although higher modes exist for larger Taylor number and lower Reynolds numbers, he was not able to predict their characteristics.

Arons, Ingersoll and Green (1961) found instabilities somewhat similar to those discussed by Stern. However, the observed critical Taylor number differed with the predicted value. Using a wide range of both Taylor and Reynolds number, in a partially water-filled annulus, they found a highly organized pattern of concentric cylindrical sheets of fluid. These sheets permeated the entire interior and boundary layer regions of the "critical" zone. The waves appeared in a Taylor number range of 1,290 to  $19 \times 10^3$  and an Ekman Reynolds number



range of 1.6 to 3.6. The instability wavelength was estimated to be proportional to a product of Ekman depth and the Taylor number to the one quarter power, as predicted by Stern.

Since the studies of Stern and Arons, et al, the low Reynolds number instability work has been superceded by an interest in the "pure" boundary instabilities (at higher critical  $Re\#$ ). This has been done to such an extent, that the influence of the "body-boundary" waves experiments (although often at similar  $Ta\#$ ) has been neglected, and no observations of their occurrence reported. Specifically, Tatro (1966) states that the mechanism mentioned by Stern is not relevant to his observational results.

Faller (1963) was the first to look at the boundary layer species of instability with a partially water-filled rotating annulus. Using dye techniques to observe boundary layer motions, he estimated critical Reynolds number be varying both the flux and rotation rates. The Reynolds number was calculated assuming all flux was transported through an ideal Ekman layer of thickness,  $(\frac{\nu}{S})^{1/2}$ . By photographing the instabilities, which converged towards the sink, Faller was able to estimate both the wavelengths (9.6 to 12.6  $\delta$ ) and the wave front orientation (approx.  $14.5^\circ$  to the left of the azimuthal flow.) The critical Reynolds number for wave onset was approximately 125, after which, slowly moving spiral-like roll vortices appeared. A numerical study of the circulation, employing a power series expansion in Rossby number, predicted no radial interior flow to second order.

Barcilon (1965) obtained analytic solutions of the perturbation

equations for a non-divergent Ekman layer. He was unable to estimate accurately the critical Reynolds numbers, since his method of solution required an assumption of large Reynolds number for closure.

Lilly (1966) investigated Ekman instabilities by a perturbation analysis and numerically solved the resultant eigenvalue problem for the complete and a truncated set of equations. Both solutions showed an instability, the former at a Reynolds number 55, the latter at 93. Furthermore, stationary waves were found to be unstable for Reynolds numbers greater than 115. This instability (class B, Greenspan [1961]) disappears at higher flow rates and is thus viscous in nature. Having a greater wavelength and phase velocity than those of the class B, the predicted class A waves are more difficult to observe by dye techniques than the former. The influence of these waves was found to extend well into the interior (5 or 6  $\delta$ ). Lilly's analysis played a significant role in both confirming experimental, and furthering theoretical studies of the pure boundary instabilities.

At the same time, Faller and Kaylor (1966) derived numerical solutions for the time dependent non-linear equations of motion with perturbations on an initially laminar Ekman layer. They confirmed Lilly's finding of the class A waves' critical Reynolds number, their range being 50 to 70. The class B waves occurred for Reynolds numbers in the range of 110 to 130. Their work also predicted the previously observed wavelength and orientation of the waves. As Lilly (1966) stated, the chief merit of this non-linear solution was to allow a study of finite amplitude disturbances.

The presence of the two instability mechanisms predicted by Lilly<sup>19</sup> at Reynolds numbers of the same order of magnitude had led to some confusion in analyzing qualitative results. These shortcomings were alleviated when Tatro (1966) conducted the first quantitative measurements in a rotating source-sink annulus, using air as the ambient fluid. In contrast to earlier work with free surfaces, this model used a plex-glass tank having a rigid top. By employing a silk screen baffle as the peripheral source, Tatro varied the flux (by vacuum cleaner suction) and the rotation rate to produce the desired variability in flow parameters. Using hot wire anemometers he was able to describe the velocity profile of the interior as well as of the top and bottom boundary layers. The results showed a marked discrepancy between the actual geostrophic interior and that predicted theoretically (Faller [1963]). Also, Tatro observed that the class A waves occurred at a local Reynolds number equal to 56.3 plus a factor equal to 58.4 times the local Rossby number. Their wavelength was 25 to 33  $\delta$ , a phase-speed of 0.16 times the local interior geostrophic flow, and the orientation of the wave fronts 0 to  $(-)$ 8° from the interior azimuthal flow. Similarly, the class B wavelength is 11.8  $\delta$ , phase speed of 0.034 times the interior flow, orientation of 14.6° from the geostrophic flow, and a critical Reynolds number equal to 124.5 plus a small factor dependent on Rossby number. He also observed some inertial wave-like disturbances in the interior and a somewhat indefinite transition to turbulence at higher Reynolds numbers of order 200.

Green and Mollo-Christensen (1970) carried on work similar to that of Tatro (1966) but with a larger tank and greater flexibility in probe positioning. Their emphasis was on the exchange of energy between unstable Ekman layers (presence of class A, and at times class B waves) and the interior flow. Some spectra at different radii in the interior, for constant flux and rotation rate, showed inertial wave energy at dominant frequencies which were not readily explainable. By comparing some of the predicted inertial mode frequencies to those observed, an equivalence was established. This is not unexpected, as the inertial modes of a rotating cylinder are denumerably infinite in the range of 0 to  $2\Omega$  (Greenspan [1968]). The generated inertial waves are found to be important in altering the Ekman layer structure and vice versa, such that an equilibrium flow configuration evolves. A linear increase of the non-dimensional dominant wave frequency for a limited range of system Rossby number was attributed to Doppler effects. Their observations of the steady interior flow show circulation profiles differing greatly from the idealized potential vortex flow and a mean Ekman layer thickness of  $1.7 \delta$ . In contrast to Tatro (1966) the authors found no dependence of the boundary layer thickness on radius (i.e., local Rossby and Reynolds number). Green and Mollo-Christensen feel that the unsteadiness of the Ekman layers, due to the impingement of inertial waves, alters the existing theoretical predictions, which neglect wave radiation. No critical Reynolds' numbers are given for instability onset, although Green (1968) suggested that the class A waves were responsible for the disturbances observed.

In a recent paper, Caldwell and Van Atta (1970) using techniques similar to Tatro and Mollo-Christensen (1967) investigated the onset of the class A waves and their spectral characteristics. In close agreement with Tatro (1966), the critical Reynolds number was found to be 56.7. Both of the observed values agree well with the value predicted numerically by Lilly (1966). The wave frequencies found by Caldwell and Van Atta are much higher than those alluded to by Tatro (1966). The class B waves are not observed. Caldwell and Van Atta also present mean zonal velocity profiles for the interior (radially) and the horizontal boundary layers (vertically). The latter are found to match the ideal Ekman layer with amazing similarity and exhibit no radial dependence for Reynolds numbers below critical values. They observed a sudden onset of turbulence in the boundary layer at a Reynolds number of 148.

The mean circulations obtained by Caldwell and Van Atta in the interior somewhat resemble those of Green and Mollo-Christensen, although the former are much smoother (Caldwell and Van Atta do not show actual points of observation). No interior spectra are presented. Caldwell and Van Atta give a chart summarizing the pertinent experimental and theoretical Ekman layer instability (high  $Re\#$ ) work in rotating annuli, which serves as an excellent history of the field to this time.

The diversity and similarity of work in rotating annuli leads to much speculation about extraneous influences on the flow observations and conditions. As Lilly (1966) states, the initial dye studies inadvertently but effectively filtered out evidence of the quickly moving class A disturbances. The china clay technique used by Gregory, et al

(1955) on a rotating disk was only sensitive to stationary bands. Differences in the results of quantitative studies of the annulus are due mainly to the influence of apparatus configuration in altering the basic flow.

On surveying the similar onset criteria found by these workers (hot wire methods in annuli) for the class A waves, Lilly's (1966) assertion that this instability will always find suitable shear conditions in the lower part of the Ekman layer, is substantiated. However, non-linear modifications of the Ekman layer structure, mentioned by Barcilon (1970) may in some cases inhibit the formation of class B waves, which are generated in the upper part of the boundary layer.

The large discrepancy in critical Reynolds numbers between annulus and disk experiments is attributable only to its means of computation. The value of  $Re^1$  for the class B waves found by Tatro (1966) is of order 370 and by Faller (1963), of order 450. These compare favorably with Smith (1945), who observed 483 and Gregory, et al, (1955) who found 435 as their critical Reynolds number ( $Re^1$ ). The prime denotes the difference in its calculation.

Hide (1968) studied the non-linear modifications to source-sink flows of various geometries and carried out some interesting qualitative experiments. He predicted that the side wall boundary layer adjacent the source was liable to be thicker at higher Rossby numbers. No equivalent change was expected in the sink region. Recently, Dudis and Davis (1971) have re-examined Ekman layer instabilities by appealing to the energy theory. Their numerical solution ( $Re_c =$

18.3) differs greatly from the linear results ( $Re_c = 55$ ) of Lilly (1966)<sup>23</sup>.

This range allows for the onset of sub-critical instabilities. Dudis and Davis are unable to confirm existence in the literature; however, they comment that similar problems have shown experimental verification

## CHAPTER III

## Experimental Equipment

## 3.1 The Rotating Annulus

The annular configuration used in the present work is pictured schematically in figure 3.1. Dimensionally, the tank was 24 cm. high and had an inner and outer radius of 8.5 and 61.8 cm., respectively. For most of the experiments, the source was at the outer radial position and the sink at the inner location. These boundaries were composed of one inch thick reticulated polymethane foam. A negative radial pressure gradient was imposed between these vertical walls by a vacuum system connected to the central hub. The tank was rotated about its center by a variable speed motor.

The resulting flows in the annulus were monitored by constant temperature hot wire anemometer probes. The relative positioning of the sensors allowed a thorough analysis of the velocity structure. Figure 3.2 gives a flow chart description of the associated electronic equipment. A complete discussion of the experimental setup and methods is found in Appendix I.

## 3.2 New Techniques

A number of the experimental methods used in this work are different from those employed previously. This section gives a brief account of these innovative techniques. However, the individual topics are covered in much greater detail in Appendix I.



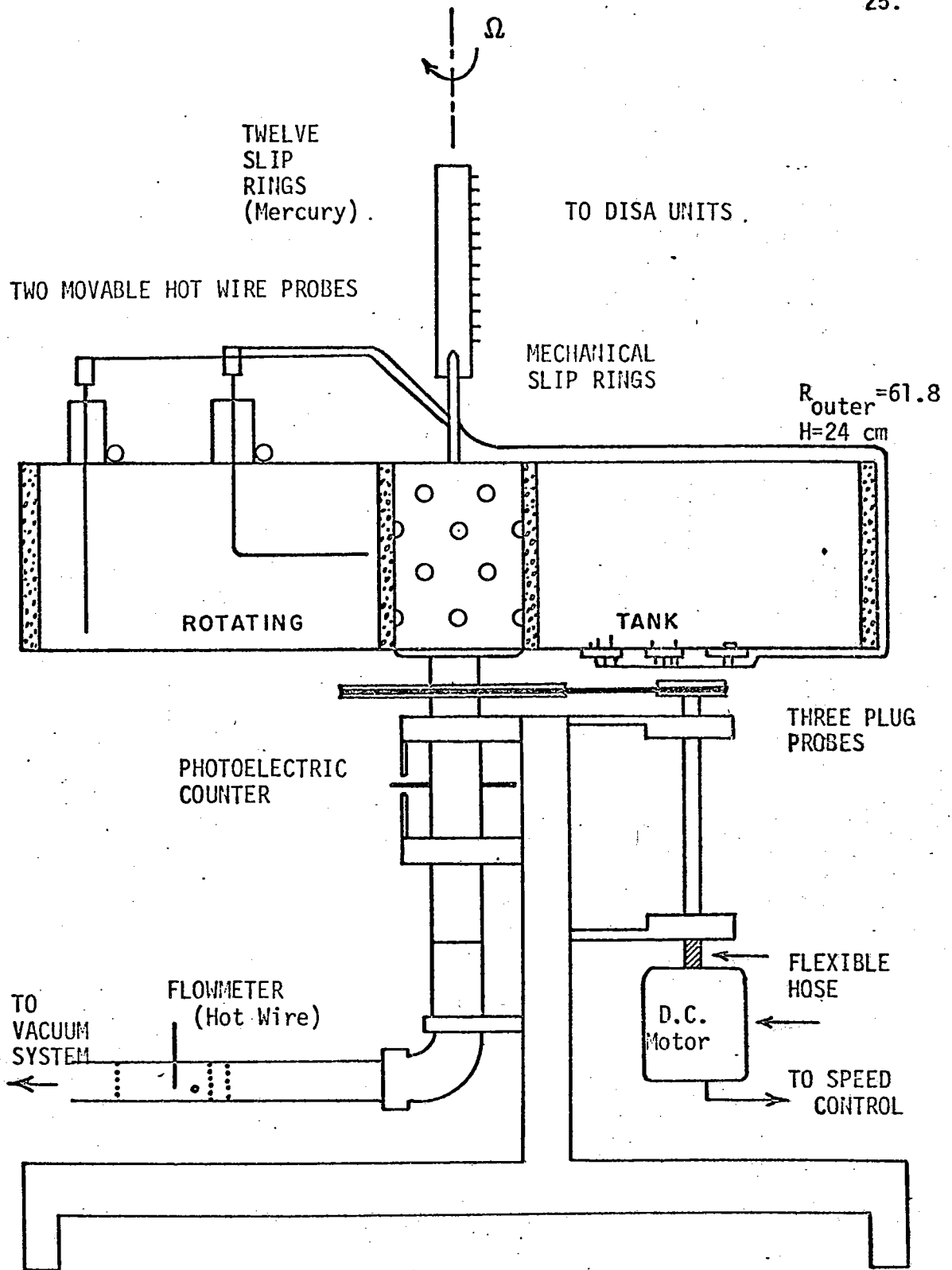
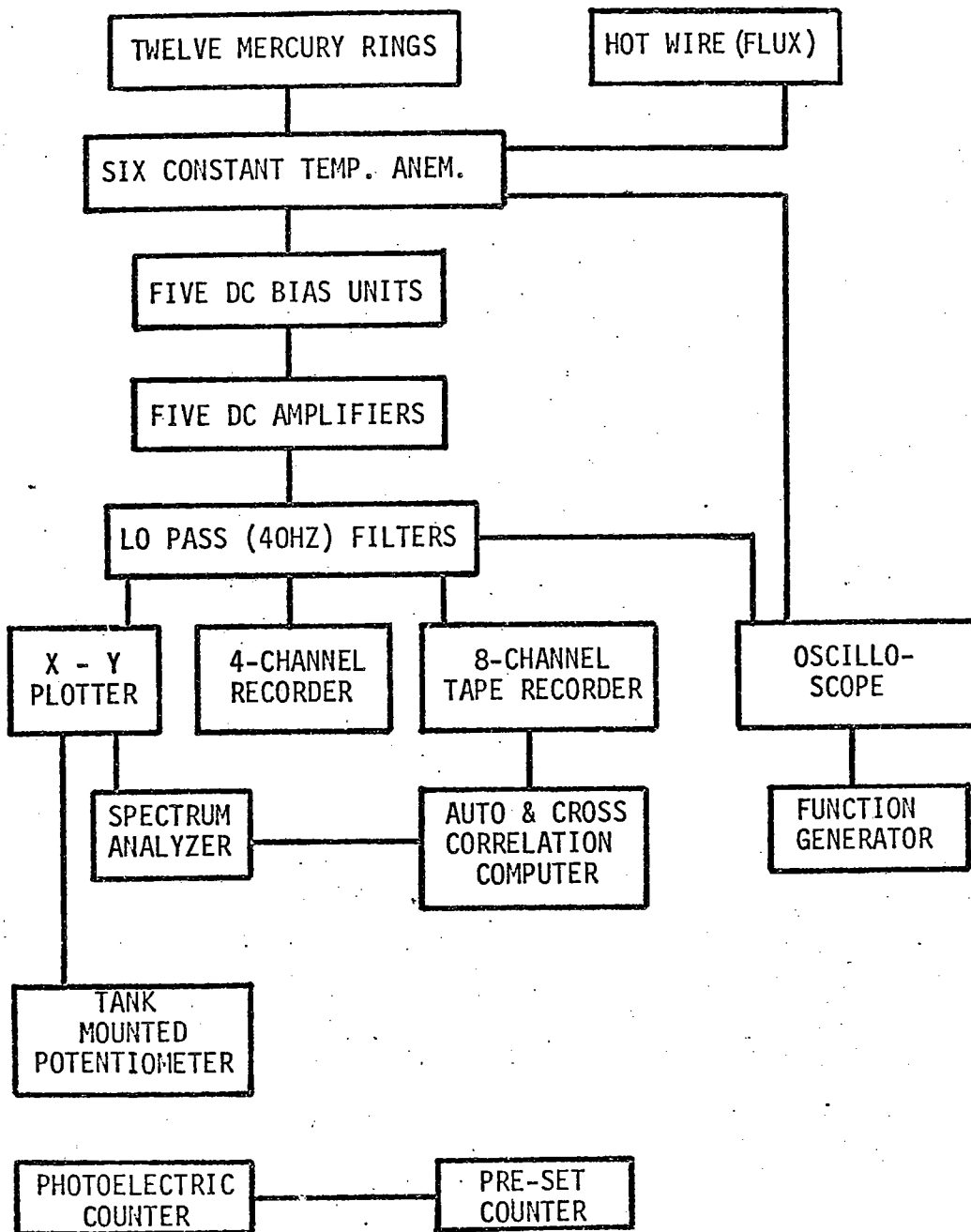


Figure 3.1



SCHEMATIC OF CIRCUITRY.

FIGURE 3.2

- a. Rotation Rate. Through utilization of a photoelectric counter to measure rotation rate, a significantly higher degree of accuracy (10 times greater) was obtained, than in earlier, similar experiments.
- b. Probe design. A single (extended) probe was constructed with the capability to measure interior velocities at all radial positions, within a short time. The resultant scatter in the circulation profiles was shown to be minimal. Previously reported observations, with single fixed sensors, were subject to ambient temperature changes, which distorted individual velocity distributions for a constant flux and rotation rate. Furthermore, uniform conditions of flux and rotation rate were not always assured when using the latter technique. Past measurements of velocity within the Ekman layer have been subject to errors in probe height determination. To overcome this difficulty, a sensor with a third leg was manufactured. This leg was longer than the probe needles and served as an accurate measure for the vertical distance. An added advantage of this design was the elimination of possible probe damage from impact with the lower wall.

Small plexiglass mounted probes were used for some of the cross-correlation work in the Ekman layer. Similar hot wires used for the interior measurements allowed a more detailed view of the flow than possible with the top-mounted probes. Figure AI.1 shows the probe configurations employed in this work.

- c. Wall Proximity Effects. In the past, Tatro (1966) and Green (1968) have observed anomalous hot wire response, for measurements close to the top and bottom walls. This distortion resulted in an observed increase in velocity for decreasing height in the Ekman layer. The effect has led to some errors in estimating onset criteria for the Ekman layer instabilities (Green and Mollo-Christensen [1970]). By calibrating the heat losses under conditions of "no flow", Dryden's (1936) method was used to correct the observed voltages. This technique gave a vertical distribution of velocity comparable to theoretical prediction.
- d. Low Velocity Work. Past experimenters using hot wires, have assumed a linear relationship between the square of recorded voltage and the square root of the perpendicularly impinging flow velocity. This simple dependence fails for velocities below 25cm/sec. Linear extrapolation into the velocity range of 0 - 25cm/sec. has been a source of much experimental error. No calibrations were possible in this range since previous workers used vortex shedding methods, which fail below 25cm/sec. Presently, a new low velocity wind tunnel was designed employing an entirely different calibration technique. Using this method, accurate calibration curves from 1 to 100 cm/sec. were possible. No linearization was necessary.

A detailed account of observation techniques is included in Appendix II. The present experimental set-up was

not amenable to flow visualization using smoke, dyes, etc. The aluminum plates and the necessity of having a baffle on the outer radial wall gives little opportunity for using any combination of mirrors and cameras. A clear plexiglass insert would be one solution, if sufficient lighting was available. Tatro (1966) has conducted some smoke experiments in a similar tank, which had plexiglass discs as top and bottom walls. Numerous experiments using dye techniques in water-filled annuli have been reported.

## CHAPTER IV

## Mean Velocity Structure in the Annulus

In general, each observation was composed of a mean velocity, with a variety of superimposed wave motions. The time-averaged mean velocity of this signal was found to be independent of the azimuthal coordinate, and exhibited a vertical and radial structure in the boundary regions, similar to the theoretical predictions. Although, the results presented in this section are simply averages of the actual flow, the role played by the transients in altering this mean structure may be an important one.

As discussed in Chapter III, the influence of ambient temperature changes and non-uniform conditions can explain the irregularity of some profiles in the literature. By utilization of the extended probe (see section 3.2), this inconsistency was eliminated in the present work. Having removed this important source of error, the changes resulting from viscous and non-linear modifications were more readily seen. A thorough discussion of the observation methods used for the mean velocity work is given in Appendix II.

#### 4.1 Radial Structure of Vertically Independent Flows

##### 4.1.1 Theoretical Predictions

Given the geometry, pictured in figure 2.2, with a peripheral source and sink, one expects on theoretical grounds, that an inviscid potential vortex is formed in the interior (Lewellen [1965]). The interior in this case is a region excluding the top and bottom Ekman layers, and the side wall layers adjacent to the source and sink. As

found in Chapter II, the steady linear dynamics supports only a zonally-directed geostrophic interior flow, with the radial transport being accommodated solely in the Ekman layers. The idealized interior velocity field takes the following form (Greenspan [1968]):

$$V_I = \frac{S}{2\pi R \delta} \quad (\text{equation 4.1})$$

where  $V_I$  = theoretical zonal flow (relative to tank)

$S$  = volume flux

$R$  = local radius

$\delta$  = Ekman layer thickness ( $[\frac{2\nu}{\Omega}]^{1/2}$ )

Employing this relation, one readily finds that the dimensional circulation, ( $\Gamma' = V_I R$ ), is independent of radius, for a fixed flux and rotation. However, a majority of the results shown in this chapter will compare the non-dimensional circulation ( $\Gamma$ ) with radius. Using equation 4.1, we define  $\Gamma$  as follows:

$$\Gamma = \frac{(V_M R)}{(V_I R)} = \frac{2\pi V_M \delta R}{S} \quad (\text{equation 4.2})$$

where  $\Gamma$  = non-dimensional circulation

$V_M$  = observed zonal velocity (rotating frame)

A closer look at equation 4.2 shows that  $\Gamma$  also gives the non-dimensional zonal velocity field ( $V_M/V_I$ ). If  $\Gamma$  is assumed equal to one, we expect the azimuthal velocity  $V_M$  to vary inversely as  $R$ , and the Ekman boundary layers to be non-divergent. Adjacent to the source and sink regions  $\Gamma$  decreases as a result of the side-wall boundary layers (Stewartson [1957]).

#### 4.1.2 Observed Velocity and Circulation Profiles

Figure 4.1 shows dimensional zonal velocity versus radius for

seven increasing values of flux at a constant rotation. Although the radial dependence of this velocity field is similar to theoretical prediction, a further interpretation is difficult. The non-dimensional circulation profiles  $\Gamma(r)$  are more suitable for comparison with theory. Graphs 4.2 - 4.11 show  $\Gamma$  (with error bars), as obtained from equation 4.2, versus non-dimensional radius ( $r=R/R_0$ ). In terms of this radial coordinate, the sink and source are located at 0.13 and 1.0, respectively. The asymmetry of the error bars results from rounding off the circulation values to the nearest one-hundredth.

The circulation profiles show a noticeably lower value than predicted theoretically. Typical values of  $\Gamma$  at mid-radial positions range from 0.55 to 0.75. However, adjacent to both the source and sink a marked decrease in  $\Gamma$  is apparent. Within the range of  $r=0.35$  to 0.75,  $\Gamma$  is found to increase with radius at the higher flux rates. This is in contrast to the lower fluxes, where a nearly constant distribution of  $\Gamma$  is obtained.

#### 4.1.3 Comparison and Discussion

A comparison of the present and previous work to theoretical prediction shows a definite difference from the relation determined in equation 4.1. This discrepancy can be related to the influence of non-linearities, and also to viscous action adjacent to the tank walls. Since  $\Gamma$  is found to vary with radius, divergences in the Ekman layer are produced. A calculation of the resulting induced vertical mass flux (Greenspan [1968]), shows typical velocities of order 1% of the mean zonal flow, for the relative interior vorticities present. To the present time, the influence of wave radiation in altering the mean flow has not been included in any theoretical model.



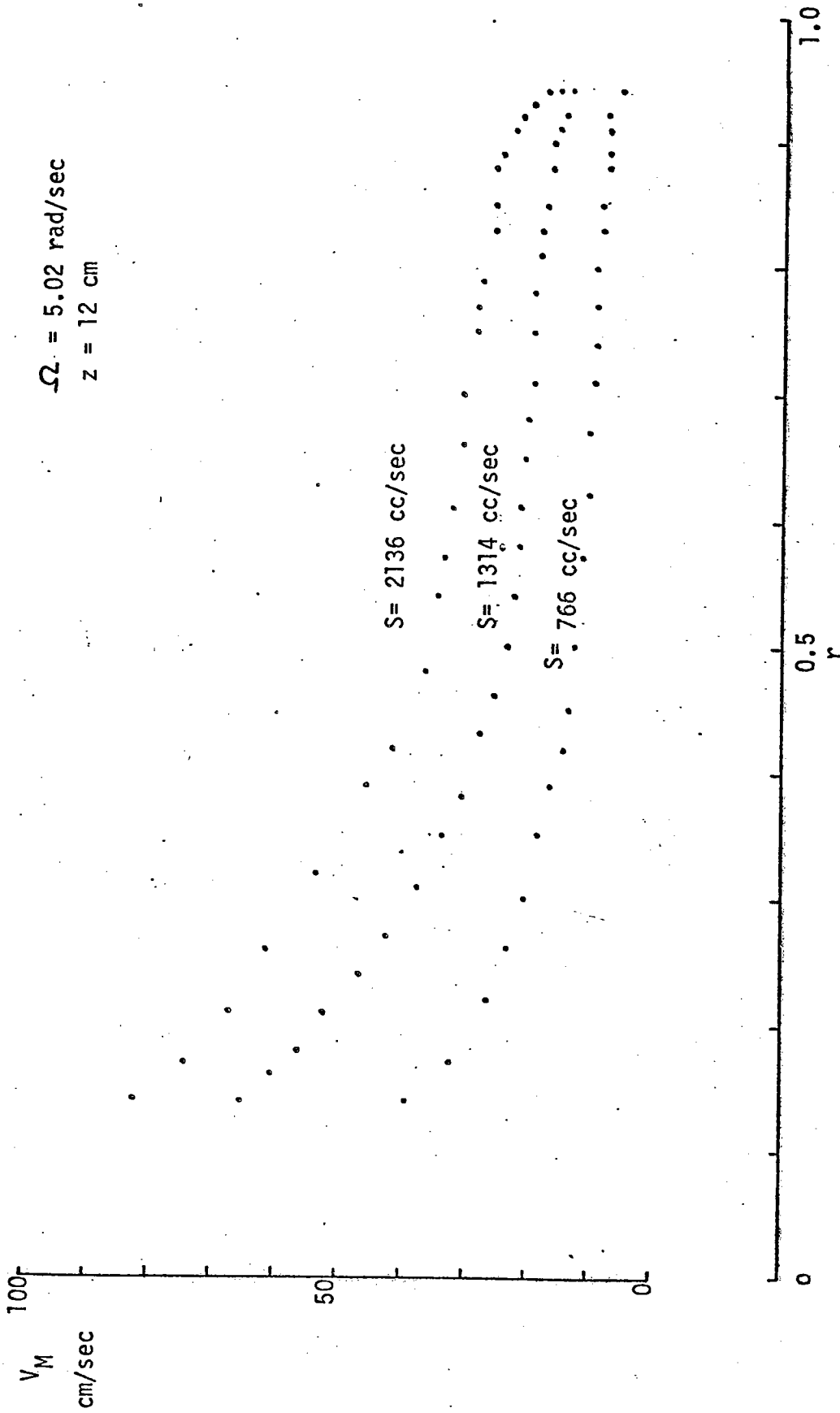


FIGURE 4.1 - ZONAL VELOCITY PROFILES

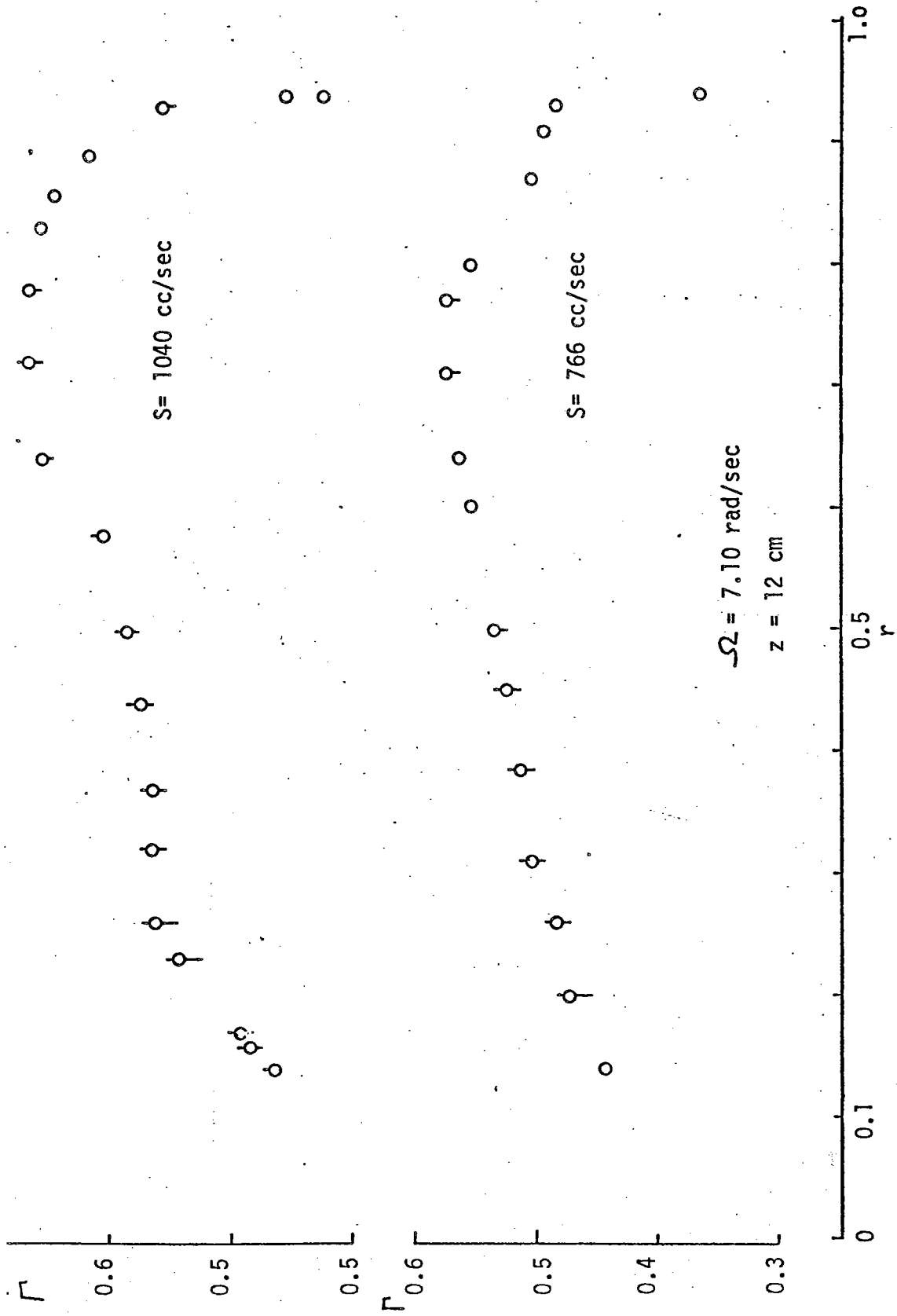


FIGURE 4.2 - CIRCULATION PROFILE

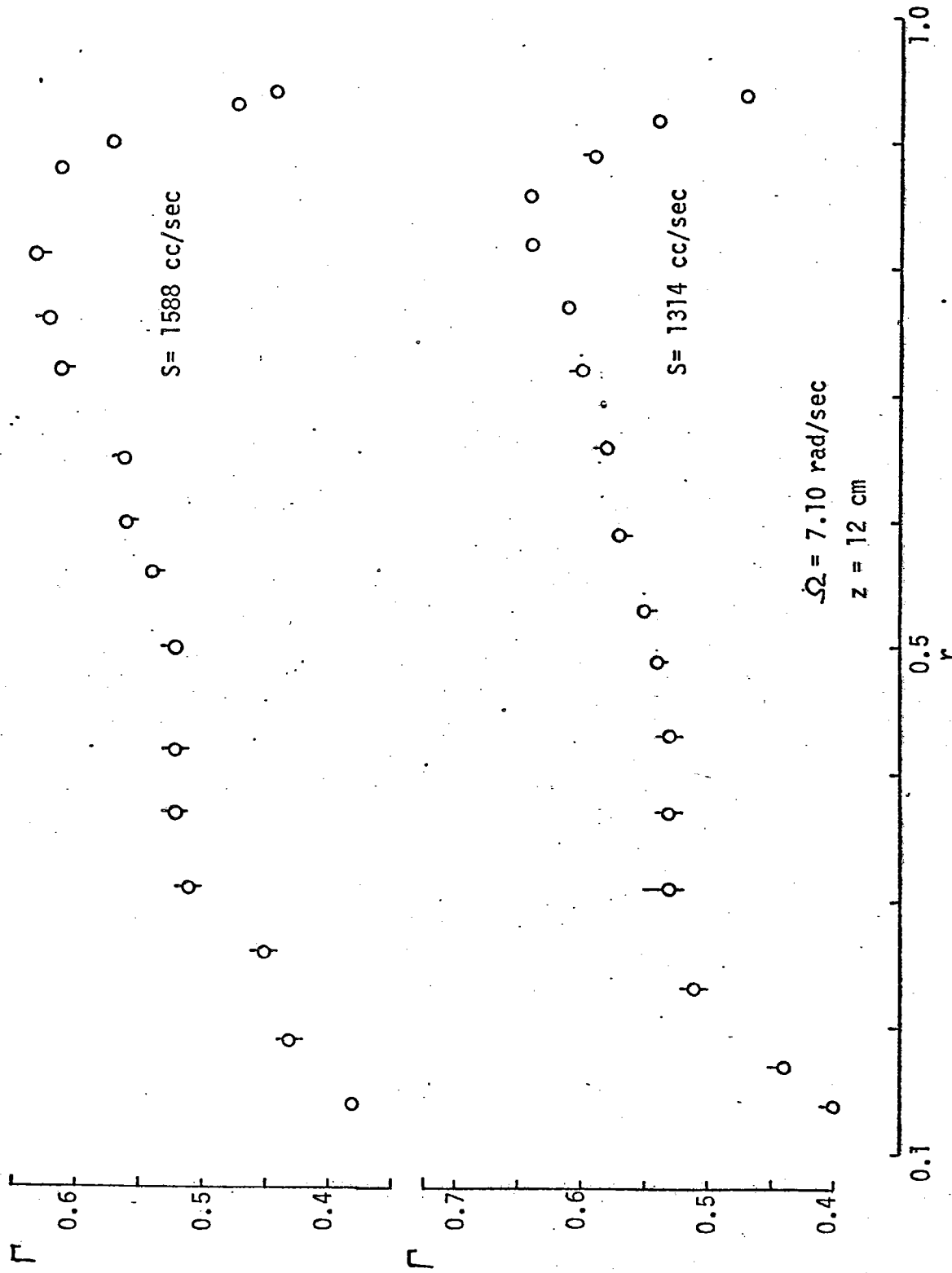


FIGURE 4.3 - CIRCULATION PROFILE

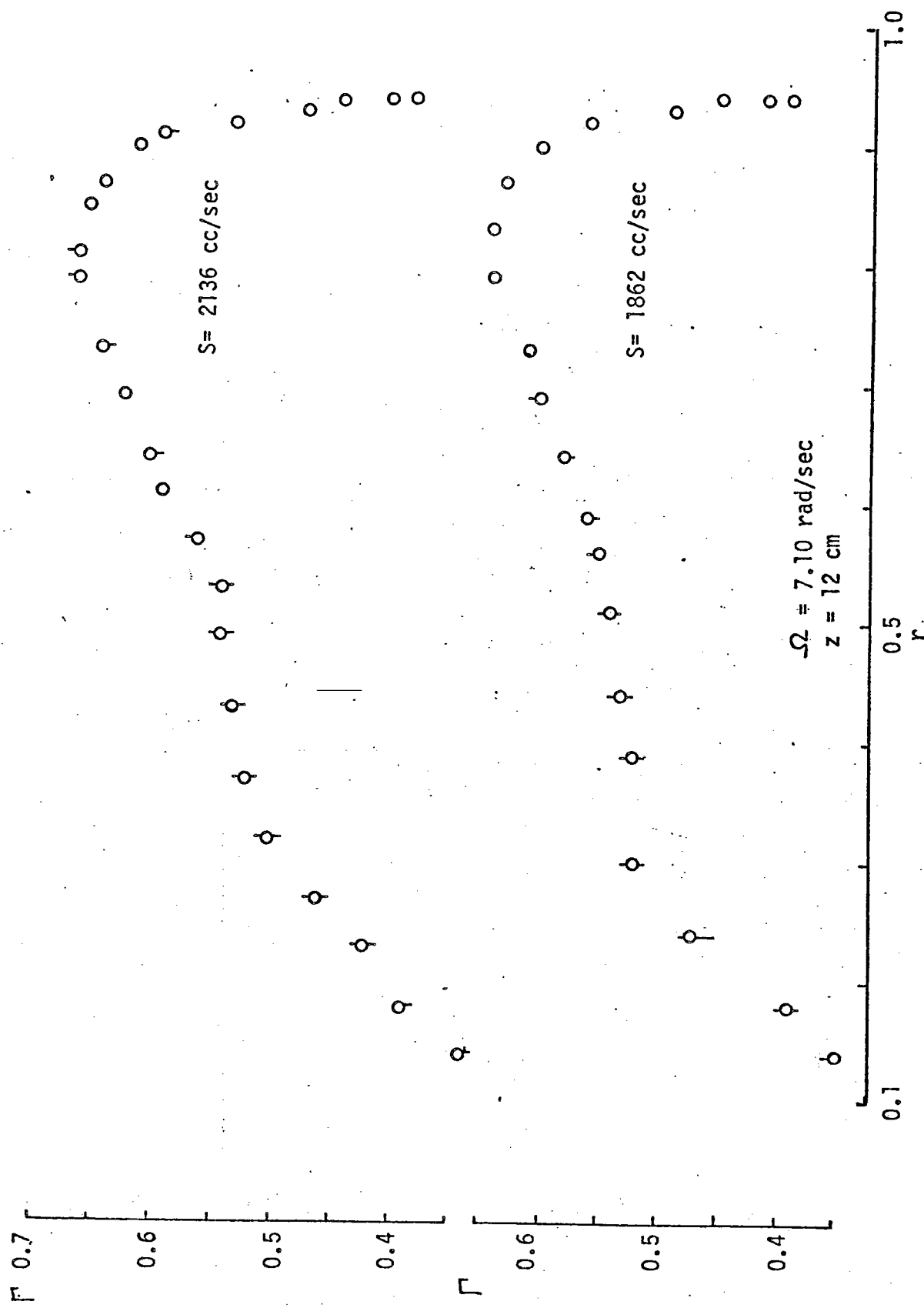


FIGURE 4.4 - CIRCULATION PROFILE

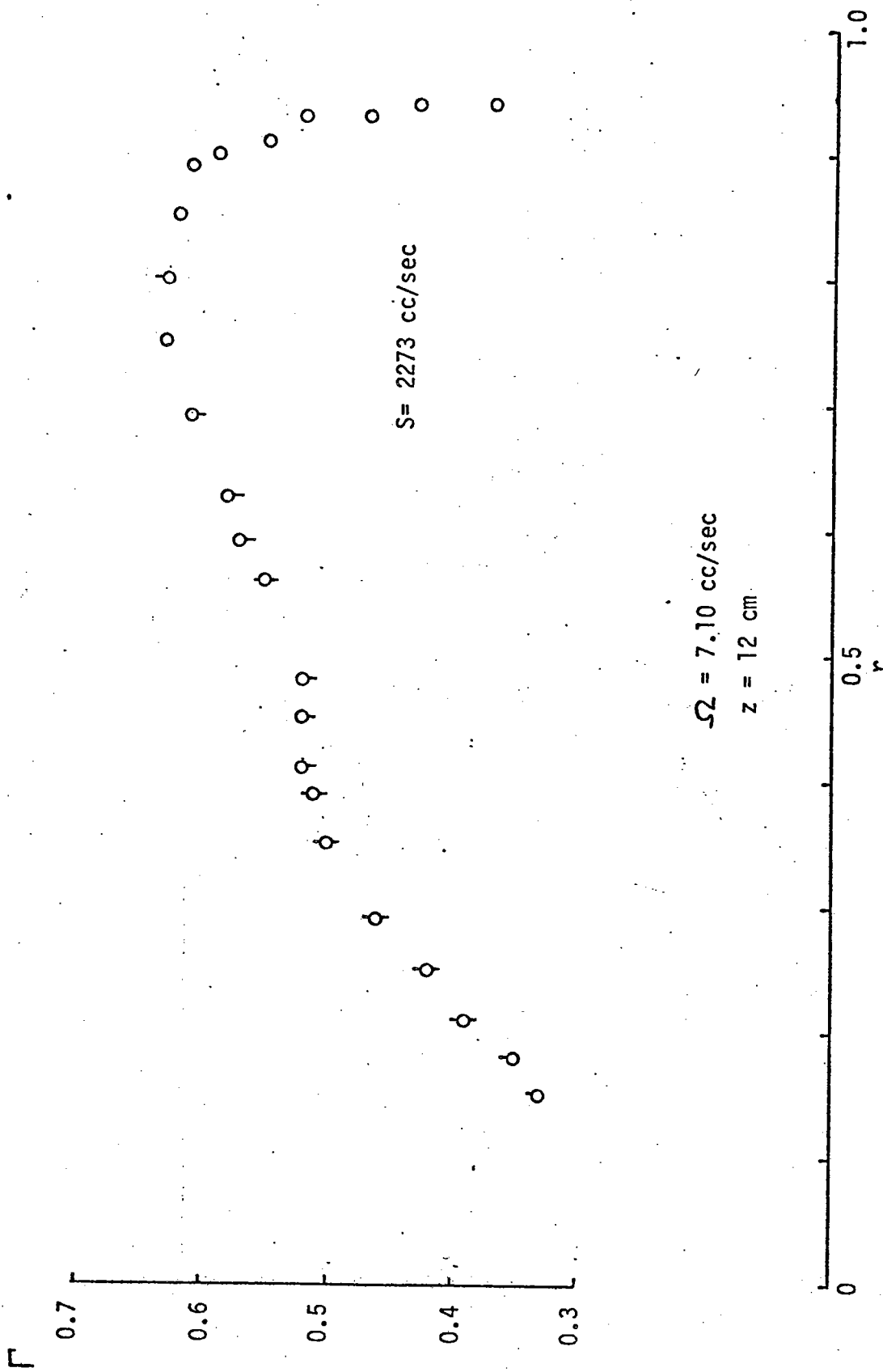


FIGURE 4.5 - CIRCULATION PROFILE

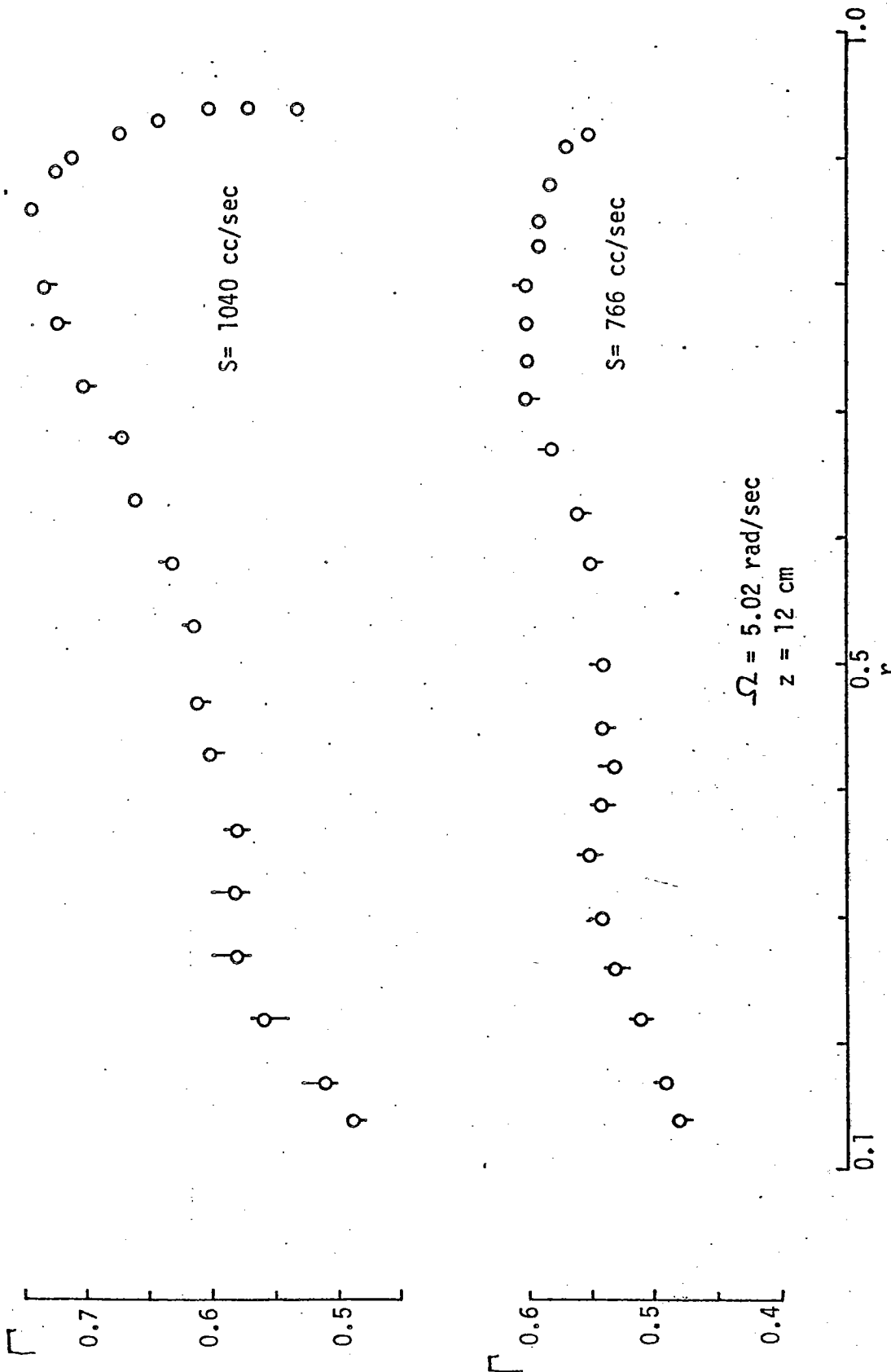


FIGURE 4.6 - CIRCULATION PROFILE

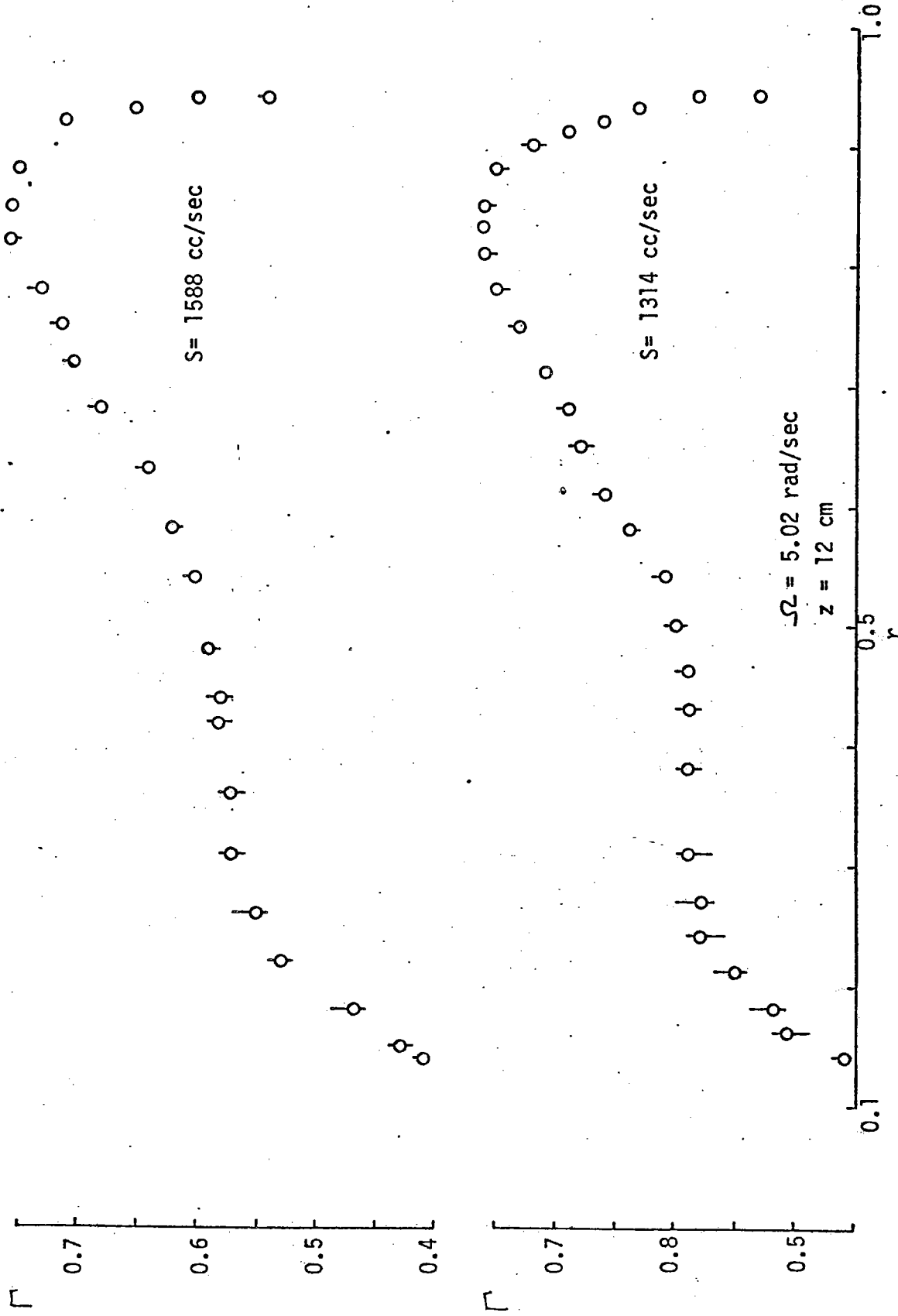


FIGURE 4.7 - CIRCULATION PROFILE

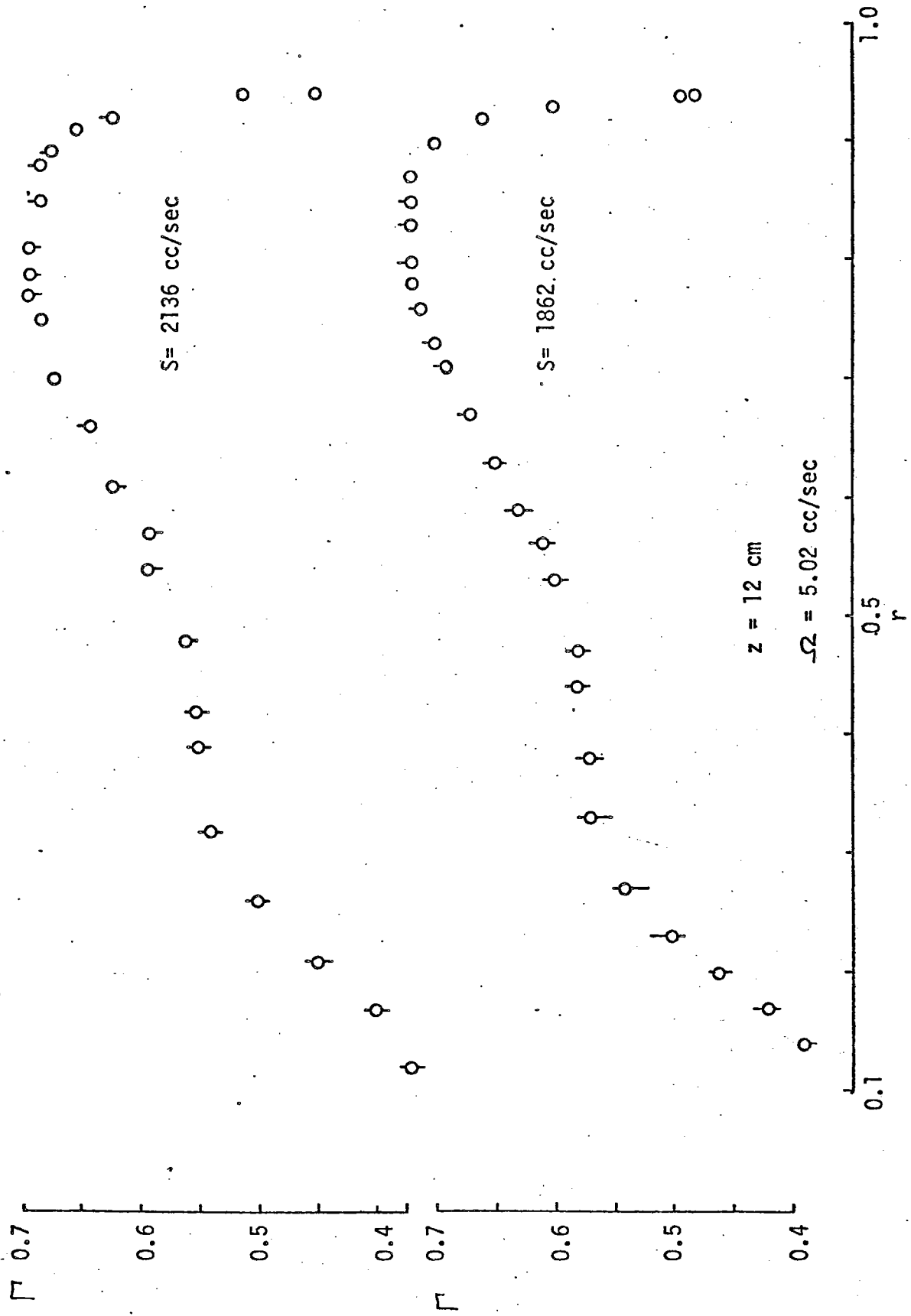


FIGURE 4.8 - CIRCULATION PROFILE

$z = 12$  cm

$\Omega = 5.02$  cc/sec



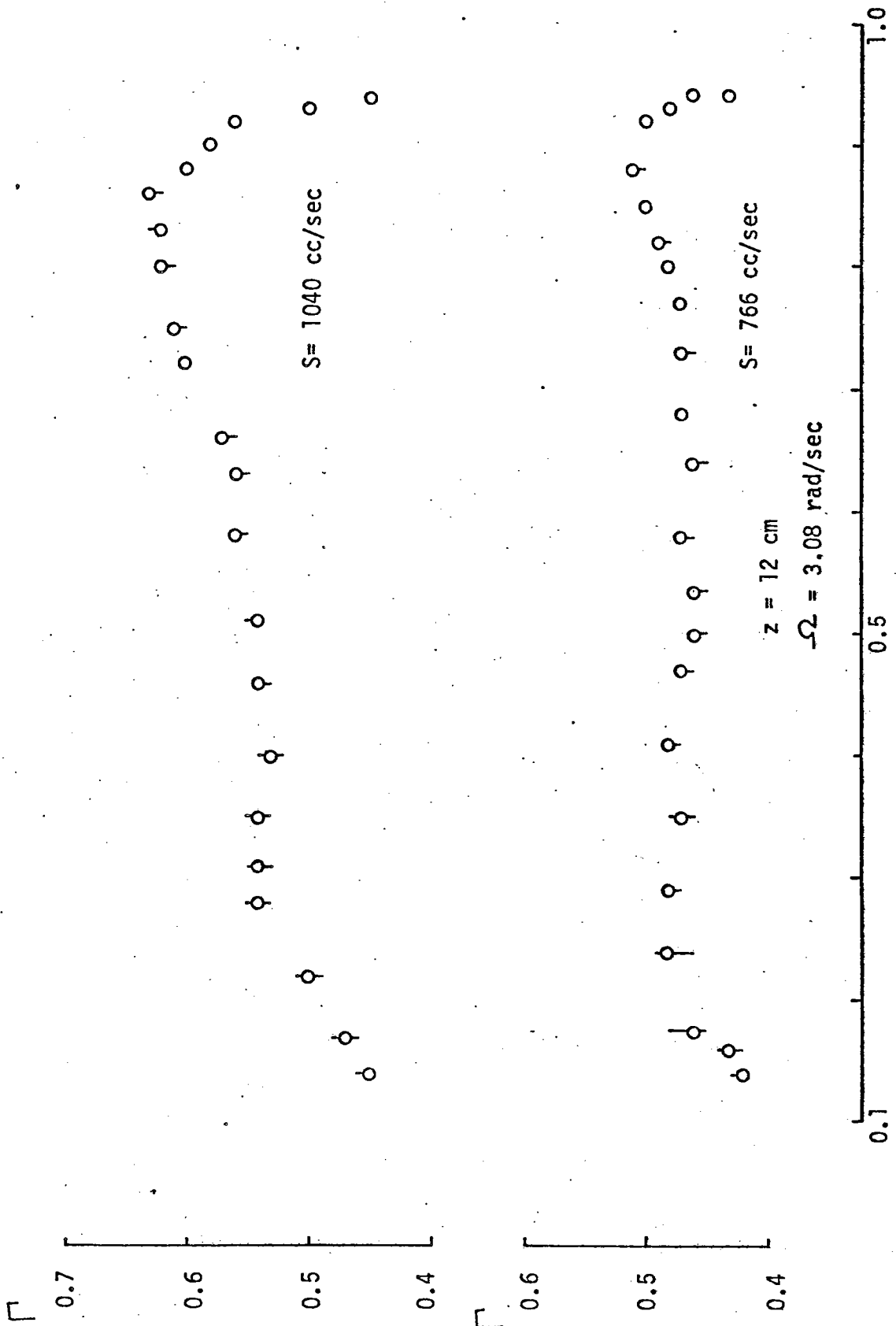


FIGURE 4.9 - CIRCULATION PROFILE

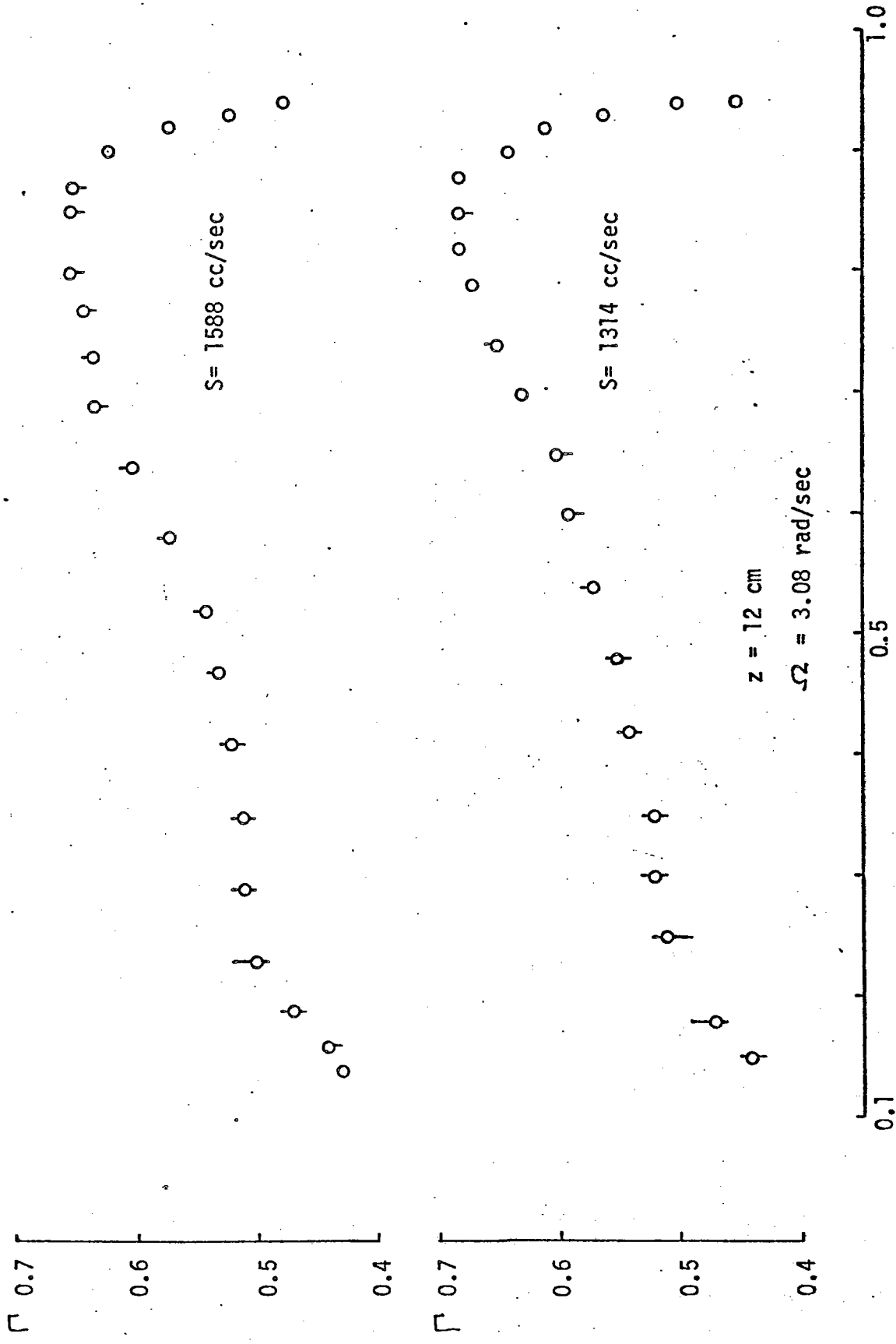


FIGURE 4.10 - CIRCULATION PROFILE

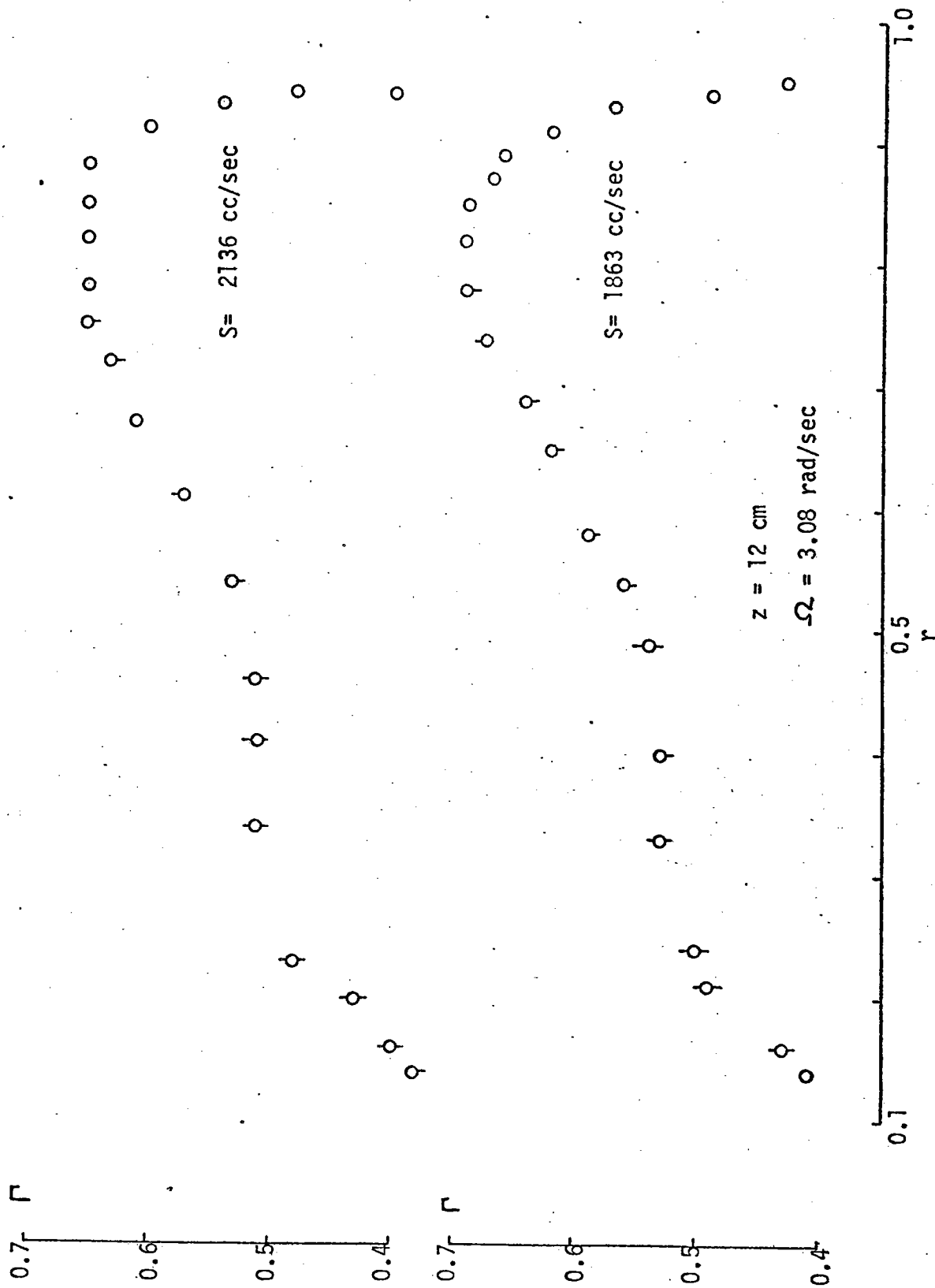


FIGURE 4.11 - CIRCULATION PROFILE

Past observations of the circulation profile have been of a somewhat sketchy nature. Generally, results have been obtained over a limited range of flux and rotation. Tatro (1966) published only a single profile of velocity (dimensional) against radius. However, by using his results, it was possible to compute a mean value of  $\Gamma$  as 0.7, and also show that  $\Gamma$  increased over a certain radial range. Tatro's work focused on the interior region, excluding the sidewall boundary layer regions.

From a limited number of profiles, Green (1968) obtained radial dependence of circulation in marked contrast to the present findings. For the lowest flux value (680 cc/sec.), Green observed a large increase in  $\Gamma$  with radius from  $r=0.2$  to  $0.92$ , whereas at the higher flux (1310 cc/sec.), his profile was flat from  $r=0.2$  to  $0.5$  and showed only a gradual increase over the remaining radial range. He attempted to explain this  $\Gamma$  distribution by the existence of unstable Ekman layers in regions of constant circulation. Figures 4.2 - 4.11 reveal a completely opposite response than Green's to changes of flux. At the lower fluxes (766 cc/sec.), the profile is almost flat, while at the higher values (2000 cc/sec.),  $\Gamma$  is found to increase with radius over certain ranges. In replotting Green's (1968) results, Green and Mollo-Christensen (1970) obtained a large amount of scatter in their profiles. None of the structure observed by Green is found in the circulation profiles of the later report. This discrepancy is unexplained. Figure 4.12 shows a comparison of the circulation profiles from the three aforementioned works.

The scatter in Green and Mollo-Christensen's results is explained by the small differences in operating conditions encountered when using single fixed probes (see Section 3.2). Although

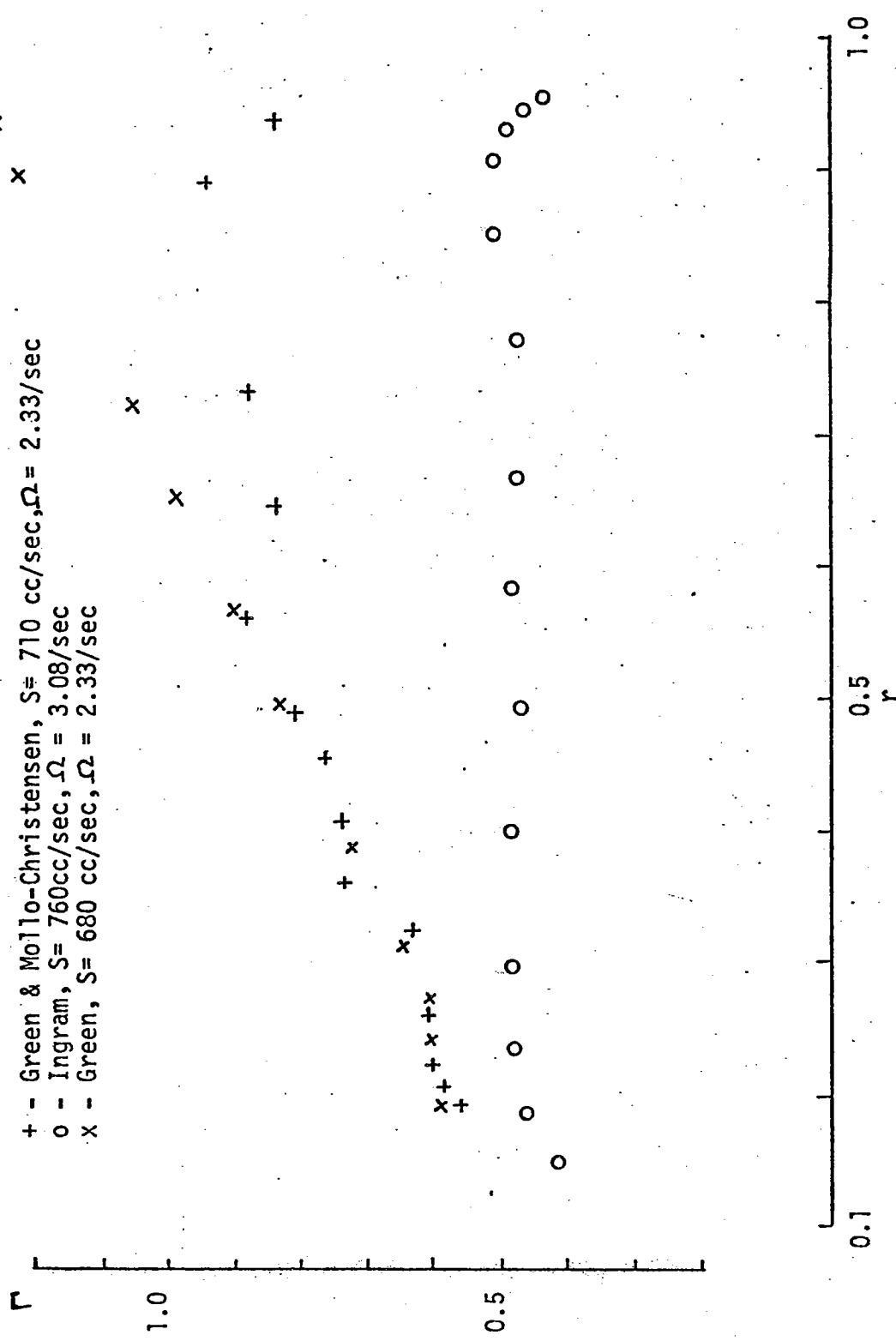


FIGURE 4.12 - COMPARISON OF CIRCULATION PROFILES

most of their profiles were taken at low flux rates,  $\Gamma$  is found to vary widely. The "typical" values of non-dimensional circulation obtained by Green and Mollo-Christensen are comparable to both Tatro's and those shown presently. However, the unstable circulation distribution,  $\frac{d\Gamma}{dr} < 0$  (Chandrasekhar [1961]) encountered in many of Green and Mollo-Christensen's results is not observed in figures 4.2 - 4.11.

Caldwell and van Atta (1970) obtain two series of five profiles, one with an effective tank radius of 109 cm and the other with a 190.5 cm radius. The results obtained using the smaller tank were discarded because of an unstable circulation distribution spanning over half the tank. The authors claim that centrifugal instabilities caused the unwanted response. The larger tank produced stable profiles at all radii less than 40 cm from the tank's outer vertical screen. No mention is made of side-wall boundary layers. Adjacent to the sink, their profiles do not show the expected Stewartson layer response (Hide [1968]), even to within 0.5 cm of the vertical screen. However, the smoothness of the interior profiles is a marked improvement over Green and Mollo-Christensen's results (1970). Caldwell and van Atta's work shows the superiority of continuously monitoring probes over fixed sensors. Although there is confusion in the article as to which hotwire configuration was used, their result format implies use of an extended probe (see Section 3.2).

Using their larger tank, Caldwell and van Atta show graphs of dimensional circulation ( $2\pi$  times  $\Gamma'$ ) against actual radius. Since no flux values are provided, the non-dimensional parameter,  $\Gamma$ ,

is uncomputable for comparative purposes. However, their curves are somewhat similar to those seen in fig. 4.2 - 4.11. At the higher fluxes they find a positive slope of  $\Gamma'$  with R. In contrast to Green (1968),  $\frac{d\Gamma'}{dR}$  shows a steady increase from the lowest flow rate. Although the overall structure of Caldwell and van Atta's profiles is comparable to the present work, the detailed distribution is dissimilar. Only in the radial range of 0.35 - 0.50 (non-dimensional) is the  $\frac{d\Gamma'}{dr}$  relationship on flux equivalent for both studies. Caldwell and van Atta find no change of slope  $\frac{d\Gamma'}{dR}$  from the inner vertical screen to  $r = 0.50$ , whereas figures 4.2 - 4.11 show a definite area of constant circulation and a side wall boundary layer in the range  $r = 0.13 - 0.35$ . Lack of suitable screening may have led to the unexplained profiles encountered by Caldwell and van Atta. Similarly, the large inertial boundary layer (adjacent to the source) produced in both their small and large tanks could result from insufficient care to eliminate jet effects on the outer screen. Although, Caldwell and van Atta ignore results from  $r = 0.80$  to 1.00, the influence of instabilities in this region can distort profiles at radially inward locations. Significantly, the change in slope of  $\frac{d\Gamma'}{dR}$  (at  $r = 0.55$  in the large tank) for both of their tanks occurs 60 - 70 cm from the outer screen. Although the present tank is 61.8 cm in radius, a comparison of the profiles seen by Caldwell and van Atta in their 107 cm tank (discarded by them for being too small) and figures 4.2 - 4.11 show no resemblance.

A notable characteristic of the present work is a flattening of the circulation profile radially outward from the inner side wall

boundary layer to the  $\frac{d\Gamma}{dr} > 0$  region. In the literature, only Faller's (1965) numerical work shows any indication of a slope change in this region. This correction, dependent on local Rossby number, was presented in terms of velocity:

$$V_{\text{Faller}} = V_I \left( 1 - \frac{3\epsilon_L}{10} + \frac{233\epsilon_L^2}{600} \right) \quad (\text{Eq.4.3})$$

$$\text{where } \epsilon_L = S/2\pi R^2 \Omega \delta$$

The present circulation profiles do not correspond to this curve, although the value of  $\epsilon_L$  obtained for the change of slope is comparable. Furthermore, the observed velocities are 25 to 30% lower than those predicted by Faller.

The detailed structure of sidewall boundary layers in a rotating source-sink annulus, as a function of Rossby number, has not been reported previously in the literature. Linear theory predicts the formation of Stewartson layers with thicknesses of order  $E^{1/3}$  and  $E^{1/4}$  (Greenspan, [1968]), adjacent to both the source and sink walls. For example, the non-dimensional zonal velocity correction resulting from the  $E^{1/4}$  layer adjacent to the source has a radial dependence of  $\exp(+\sqrt{2} E^{-1/4} (r-1))$ . In Table 4-1, the observed thickness of the sidewall boundary layers is shown. For comparative purposes, values of  $\epsilon_{\text{sys}}$  ( $\epsilon_L$  evaluated at  $R=R_0$ ) and  $E^{1/4}$  are also included. The thickness of each boundary layer was calculated using the position of a detected change in slope of  $d\Gamma/dr$ , as seen in Fig. 4.13. In this particular case, (Fig. 4.13) a second (thinner) boundary layer is also observed. However, this thinner boundary layer was not considered in detail because of insufficient data coverage. No evidence of the thinner boundary layer was found adjacent



TABLE 4-1

## Observed Non-dimensional Thickness of Side-Wall Boundary Layers

<u>FLUX (cc/sec)</u>	<u>ROT(rad/sec)</u>	<u><math>\epsilon_{sys}</math></u>	<u><math>E^{1/4}</math></u>	<u>Observed Thickness</u>	
				<u>Source</u>	<u>Sink</u>
.766	7.10	.03	.09	.20	.07
1040	7.10	.04	.09	.21	.10
1314	7.10	.05	.09	.15	.09
1588	7.10	.07	.09	.19	.09
1862	7.10	.08	.09	.17	.11
2136	7.10	.09	.09	.17	.15
2273	7.10	.10	.09	.17	.17
.766	5.02	.04	.10	.20	.10
1040	5.02	.05	.10	.14	.11
1314	5.02	.07	.10	.17	.12
1588	5.02	.08	.10	.15	.13
1862	5.02	.09	.10	.17	.15
2136	5.02	.11	.10	.19	.17
.766	3.08	.05	.11	.12	.09
1040	3.08	.07	.11	.17	.12
1314	3.08	.09	.11	.18	.12
1588	3.08	.10	.11	.20	.11
1862	3.08	.12	.11	.15	.13
2136	3.08	.14	.11	.18	.14

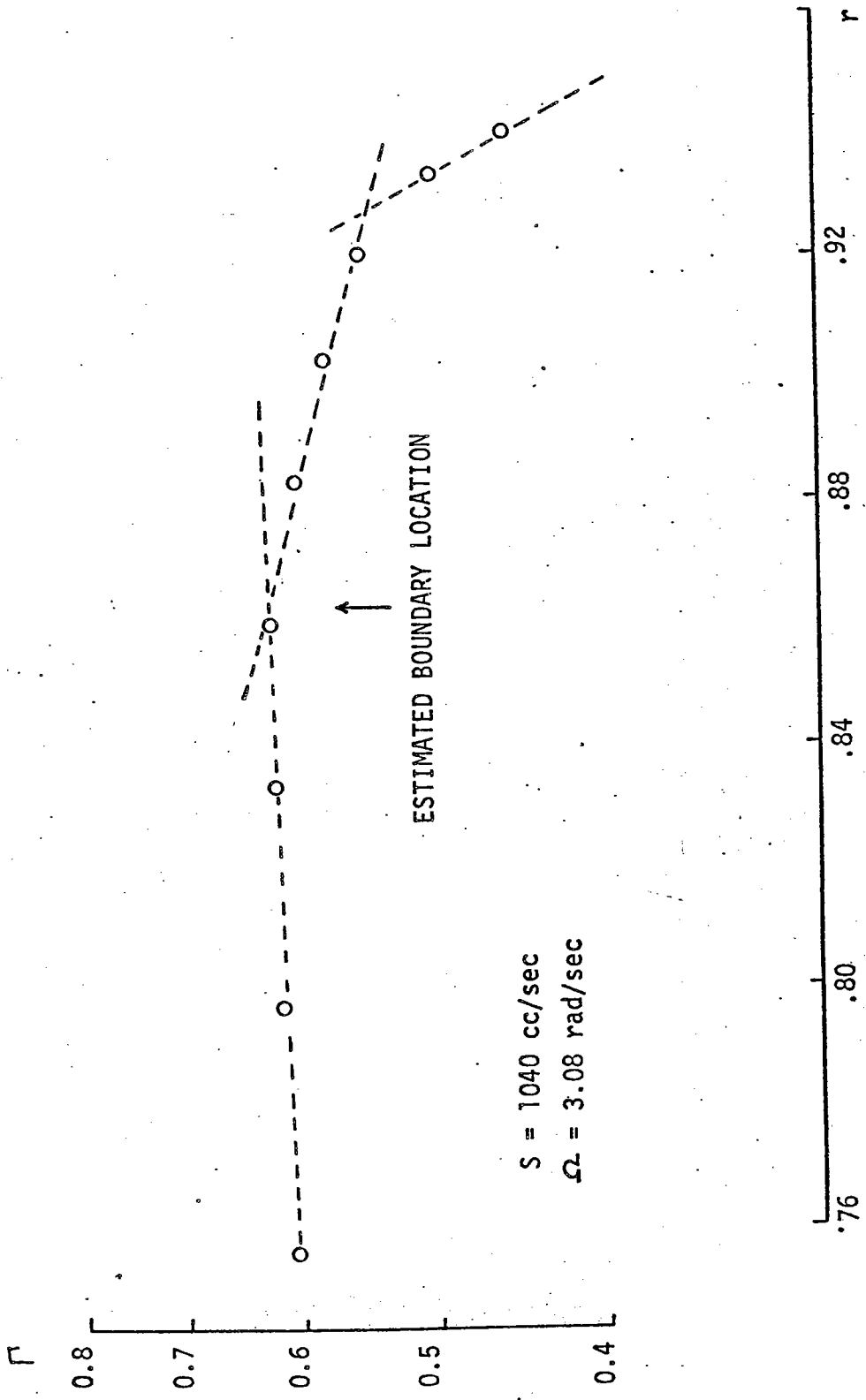


FIGURE 4.13 - TECHNIQUE OF LOCATING SIDEWALL BOUNDARY LAYER (SEMI-LOGARITHMIC PLOT).

to the sink. In contrast, the thicker sidewall boundary layers, shown in Table 4-1, were observed in all of the circulation profiles, both adjacent to the sink and the source. The characteristic slope ( $d \ln(v)/dr$ ) of the thicker layer shown in Fig. 4.13 is  $-4$ , which compares unfavorably with the linearly predicted slope value of  $-\sqrt{2} E^{-1/4} = -12$  for the  $E^{1/4}$  Stewartson layer, using Greenspan's non-dimensionalization.

From Table 4-1, the source sidewall layers are found to be significantly thicker than those adjacent to the sink. A general tendency for thicker boundary layers with increasing Rossby number is noted in the sink region. However, no systematic dependence on system Rossby number is found for the outer layer.

The sidewall boundary layers found by Caldwell and van Atta, using their smaller tank, which under certain flow conditions, had a non-dimensional thickness of 0.50, are not explained by the non-linear predictions of Hide (1968). However, Hide commented that "jet" effects often play a dominant role in expanding the sidewall layers. This layer thickening results from the fluid not being "spun-up" before injection from the source to the interior. The unstable vorticity distribution produced then generates large eddies at the outer radii. Caldwell and van Atta mention observing similar large eddies in this region, but use the fact as a rationale for building a larger tank. Jet effects are minimized in the present work since the fluid passes through a large thickness of polyurthane foam before entering the annulus. Green (1968), using a similar material, verified experimentally that the injected fluid was "spun-up". This feature may explain the radically different profiles obtained by Caldwell and van Atta both near the sink and the source. Since they give no observations for the outer 35 cm of their larger tank, a definitive

comparison is not possible.

The circulation values (Fig. 4.2 - 4.11) were subject to the largest errors at the smaller radii. This was due mainly to the estimation of probe position as taken from the X-Y recorder. The region of increasing circulation was unquestionably present, and was shown to play a significant role in the wave dynamics (Chapter V). This feature may be a high Rossby number effect as mentioned by Greenspan (1968), but the dependency is a complex one.

Summarizing, the profiles of circulation demonstrate a greater amount of structure than predicted theoretically. The sidewall boundary layer adjacent to the sink is of order  $E^{1/4}$  in thickness. In contrast, the thickness of the source sidewall layer is generally twice as wide. This difference is not explained quantitatively by Barcilon's (1970) work. However, both Barcilon and Hide (1968) claim that the source boundary layer is the only one subject to non-linear modification. In explaining the absence of a similar radial structure in the work of Green (1968), calibration techniques may be at fault. The assumed linear relation between  $U^{1/2}$  and  $E^2$ , when calibrating (see Chapter III) at low speeds, is grossly in error. Obviously, the high flow speeds encountered near the sink do not allow a similar explanation for the absence of an inner sidewall layer in Caldwell and van Atta's work. Nevertheless, this distortion may be attributable to their inner screen. Since a vertically oriented probe cannot differentiate between radial and zonal velocities, a "jet effect" in the area of the sink would alter their observed circulation profile.

## 4.2 Vertical Structure of Velocity Adjacent to Horizontal Boundaries

### 4.2.1 Theoretical Predictions

Adjacent to any horizontal flat boundary in a homogeneous rotating fluid, an Ekman layer is formed. The characteristic thickness

of this velocity adjustment region is  $(\frac{\nu}{\Omega})^{1/2}$  (Lewellen [1965]). In the source-sink annulus, these Ekman layers are found on both the top and bottom walls. Their vertical structure is as follows (Greenspan [1968]):

$$\frac{u}{V_{\infty}} = e^{-z/\delta} \sin z/\delta \quad (\text{equation 4.4})$$

$$\frac{v}{V_{\infty}} = (1 - e^{-z/\delta} \cos z/\delta) \quad (\text{equation 4.5})$$

where  $u, v$  = radial and zonal components of velocity field

$V_{\infty}$  = interior zonal flow (outside Ekman layer region)

$z$  = vertical coordinate (measured positive inward from wall)

$\delta$  = Ekman layer thickness ( $[\frac{\nu}{\Omega}]^{1/2}$ )

A graphical representation of equations 4.4 and 4.5 yields a distribution of velocity with height as seen in fig. 4.14.

A slight departure from the theoretical profile has been predicted by Barcilon (1970), based on a non-linear modification. Figure 4.15 shows this influence as a function of the interior vorticity.

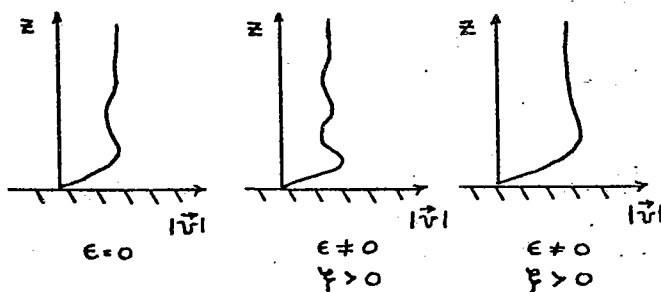


Fig. 4.15 Ekman layer changes as a function of  $\epsilon$  and vertical vorticity. (Barcilon [1970])

The expansion procedure used by Barcilon is questionable since lower order terms dropped in the momentum equation are kept in the uniformity condition required for transition to the interior (A. Bennett, personal communication). By including these terms many "wiggles"

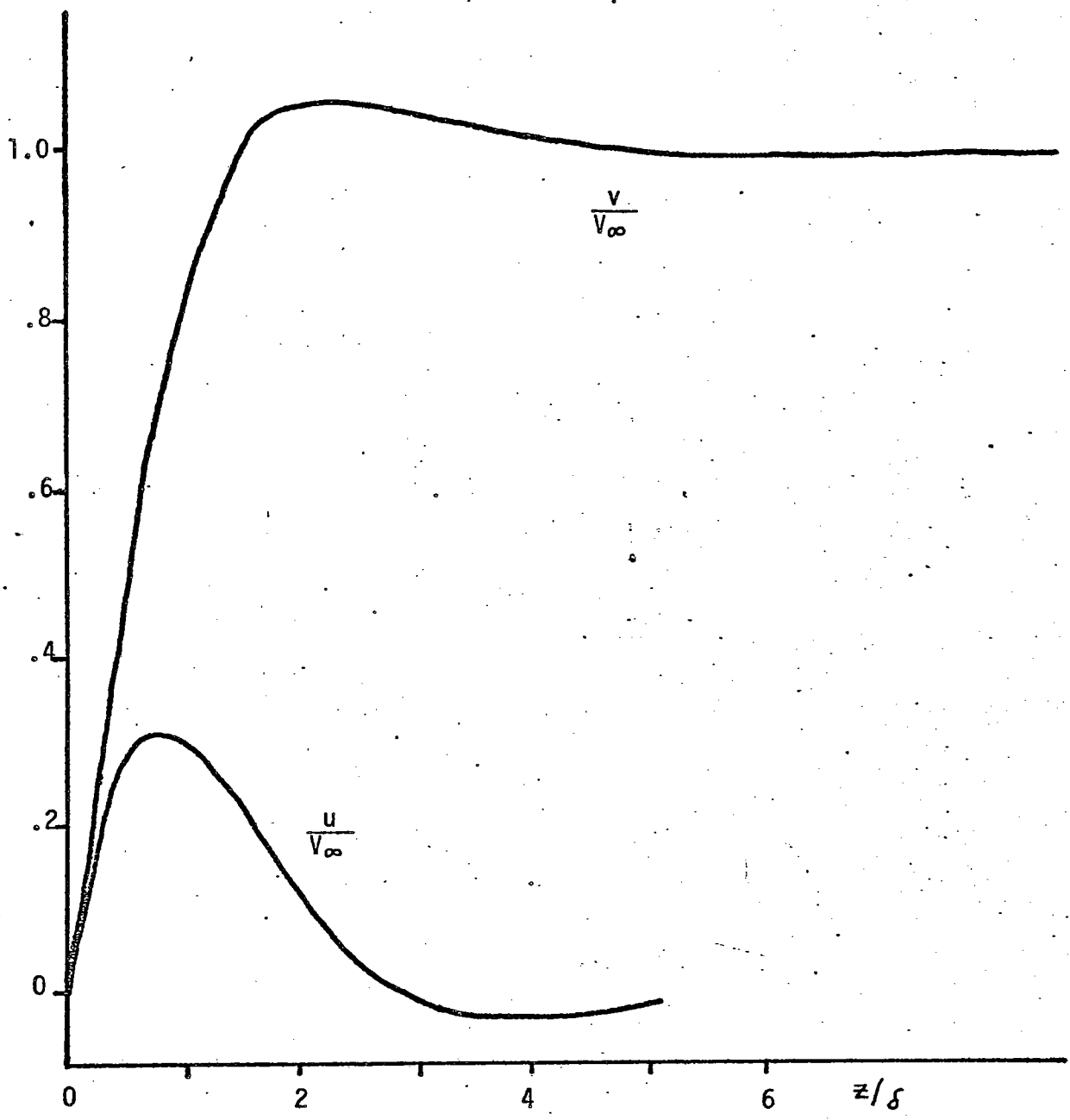


FIGURE 4.14

THEORETICAL STEADY EKMAN LAYER PROFILE

u: radial

v: azimuthal

$V_\infty$ : azimuthal interior flow

of the type shown in figure 4.15 are expected. The constructive and destructive interference of these "wiggles" yields an Ekman layer profile which is different from Barcilon's prediction.

To date, no mention has been made in the literature of any alterations in the Ekman layer structure resulting from incident inertial waves.

#### 4.2.2. Observed Vertical Structure

Incorporating the heat loss correction methods summarized in Chapter III, 26 azimuthal and 2 radial profiles were taken adjacent to the lower boundary. The sparseness of radial profiles is a result of the inherent technical problems (Appendix II). The two radial sets were obtained close to the sink, where the high interior velocity afforded better resolution. A number of similar observations, for lower interior speeds, were difficult to interpret. However, the position of the radial velocity maximum in this unreported work, varied little from the two profiles shown. Figure 4.16 shows two series of observed azimuthal velocities, and the theoretical Ekman layer curve (equation 4.5). Profile #23 shows a much higher degree of "wiggleness" than is general in most other results. This is attributable to the lower flow speeds attained at the outer radii and possibly to the higher system Rossby number (low rotation). Figures 4.17 and 4.18 show similar graphs of zonal velocity against non-dimensional height as well as the radial velocity distribution (compared to equation 4.4). These profiles are taken in two dynamically different regions. The former is within the side-wall boundary layer, while the latter is in the highest local

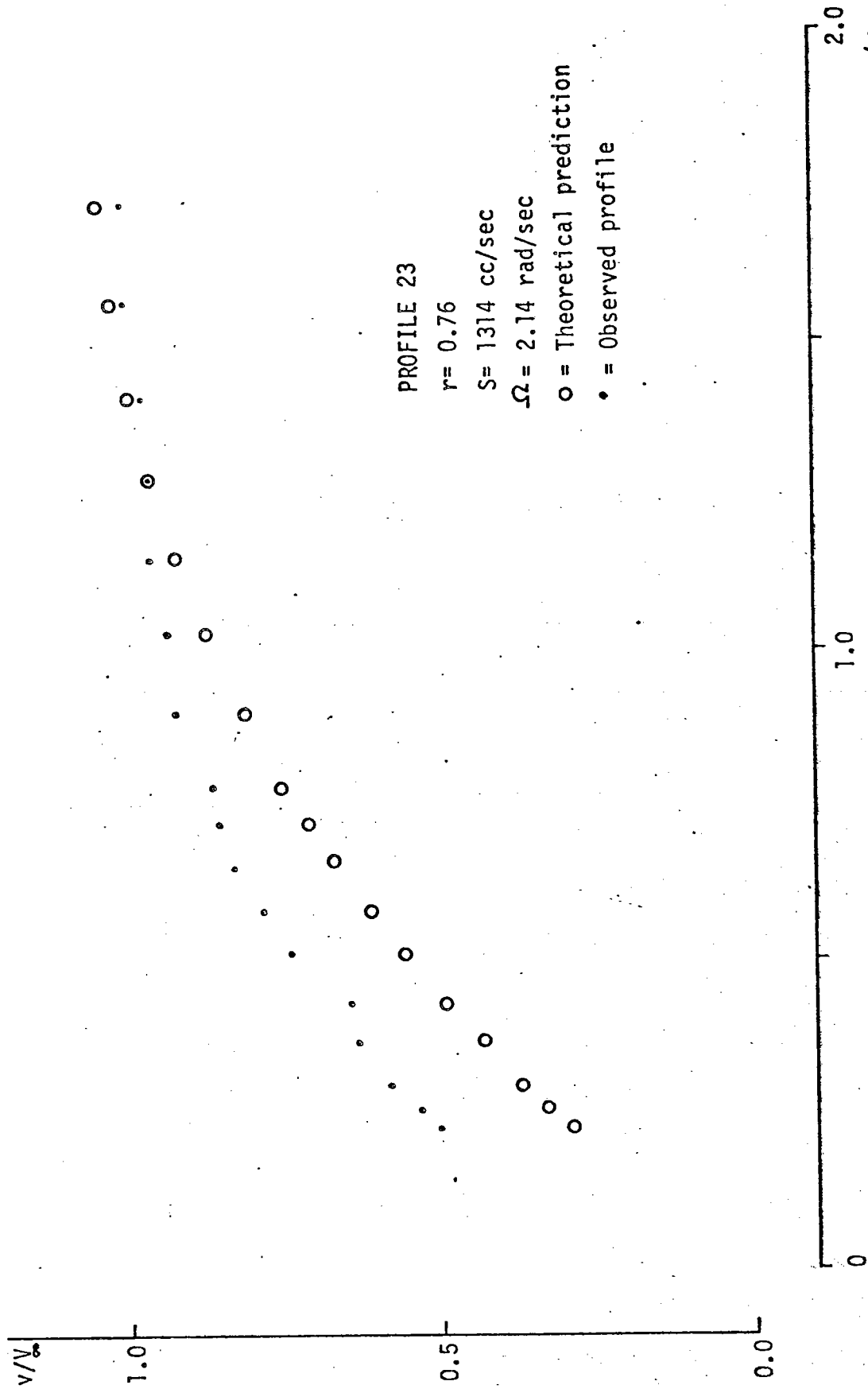


FIGURE 4.16A- EKMAN LAYER PROFILE,  
 $R = 18.5''$ , ZONAL VELOCITY



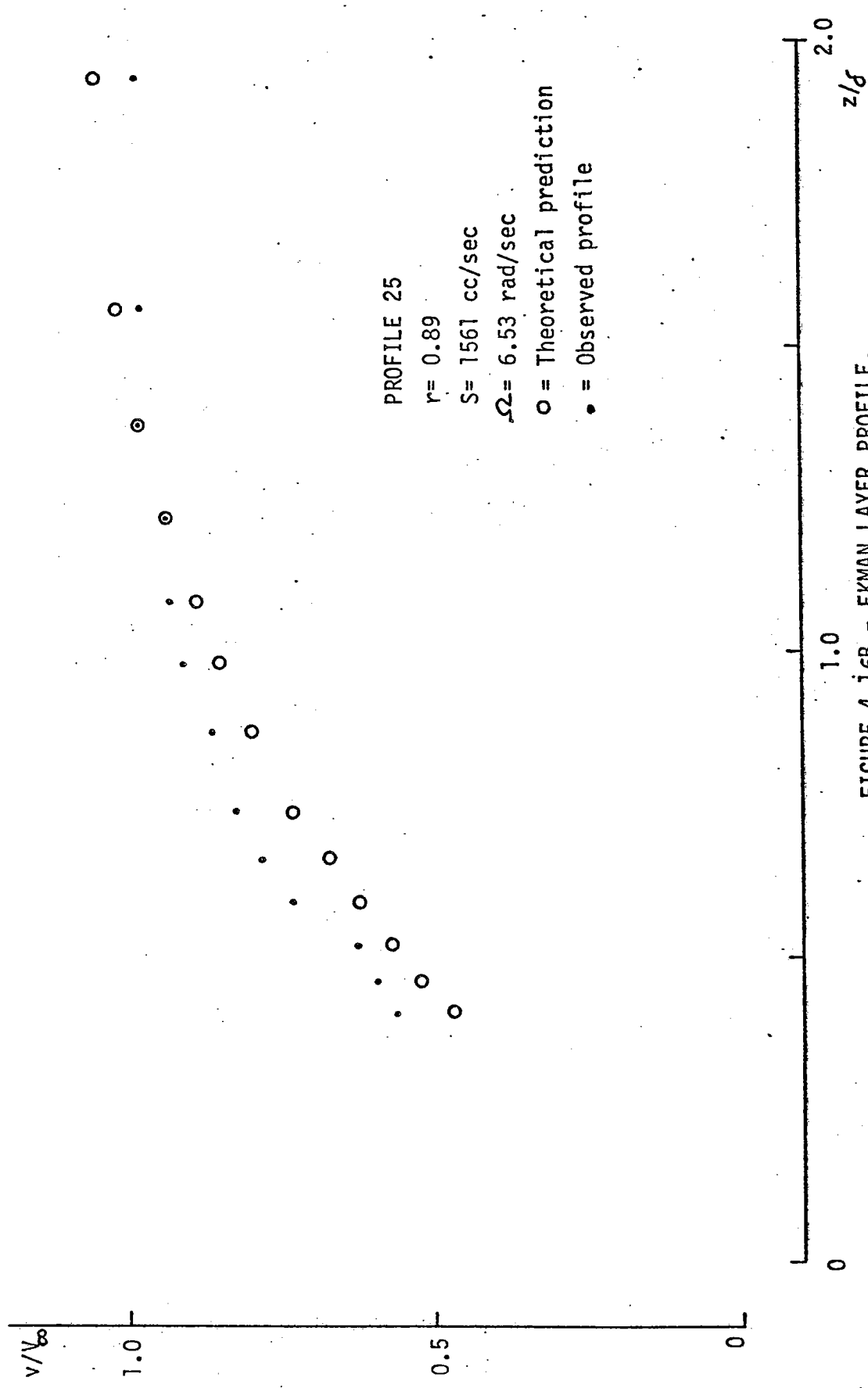


FIGURE 4.16B - EKMAN LAYER PROFILE,  
 $R = 21.6''$ , ZONAL VELOCITY

$u/V_\infty$

1.0

0.5

0

PROFILE #1

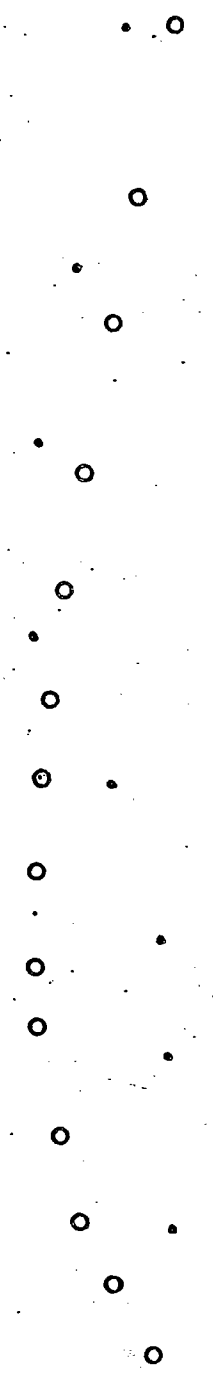
$R = 4.63''$

$S = 1588 \text{ cc/sec}$

$\Omega = 5.15 \text{ rad/sec}$

o = Theoretical prediction

• = Observed profile



2.0

1.0  
 $z/\delta$

FIGURE 4.17A - EKMAN LAYER PROFILE,  $R = 4.63''$ , RADIAL VELOCITY

$R = 4.63''$

$S = 1588$  cc/sec

$\Omega = 5.15$  rad/sec

o = Theoretical prediction

• = Observed profile

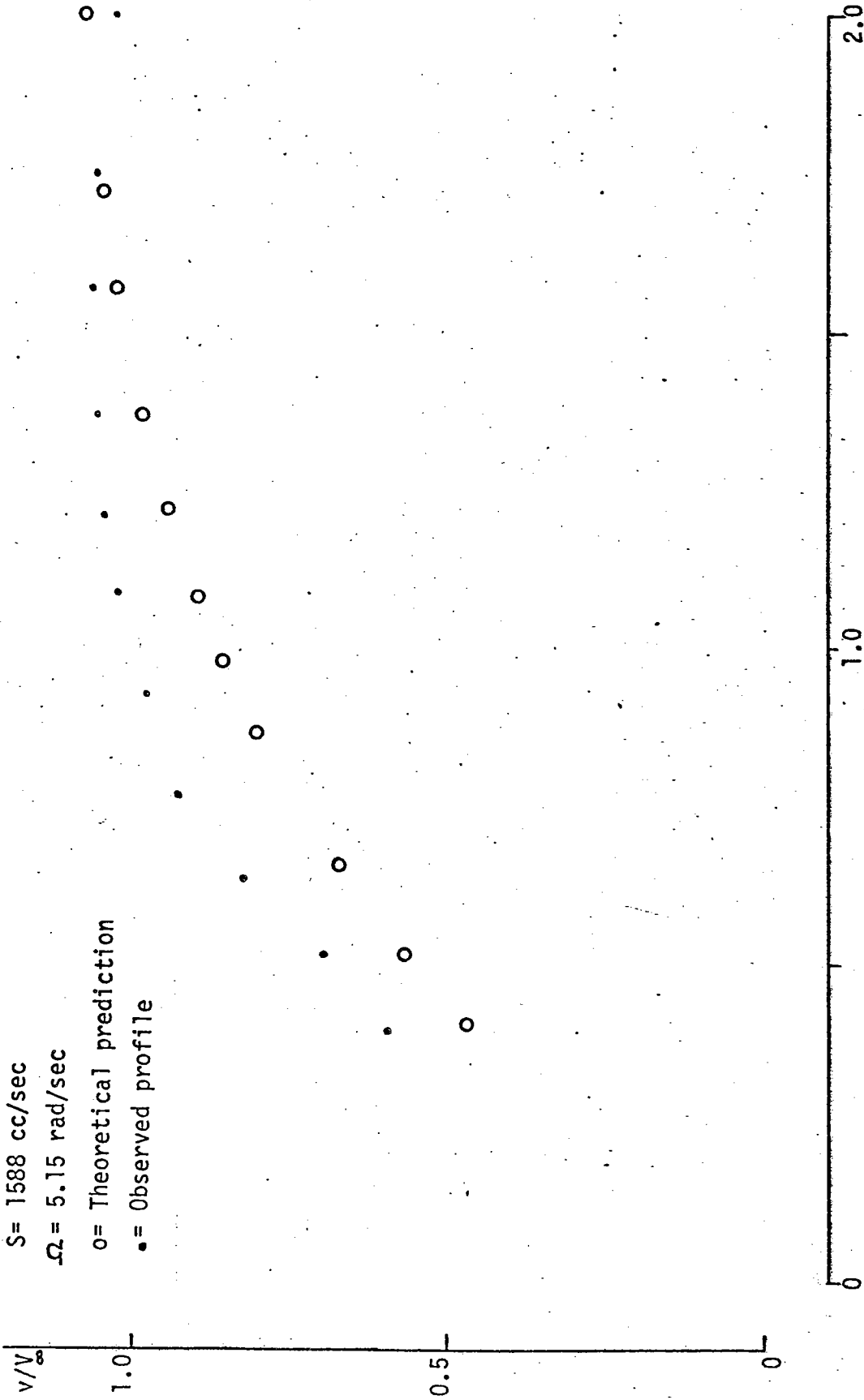


FIGURE 4.17B - EKMAN LAYER PROFILE,  $R = 4.63''$   
ZONAL VELOCITY

R = 6.00"

S = 2273 cc/sec

$\Omega = 4.90$  rad/sec

o = Theoretical prediction

• = Observed profile

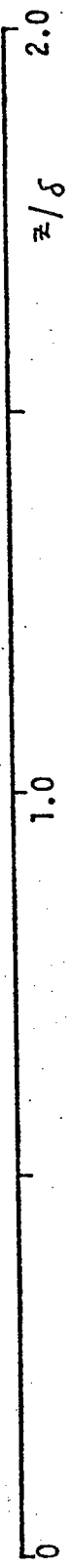
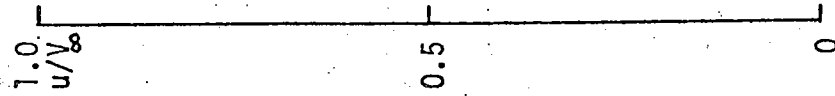


FIGURE 4.18A - EKMAN LAYER PROFILE, R = 6.00"  
RADIAL VELOCITY

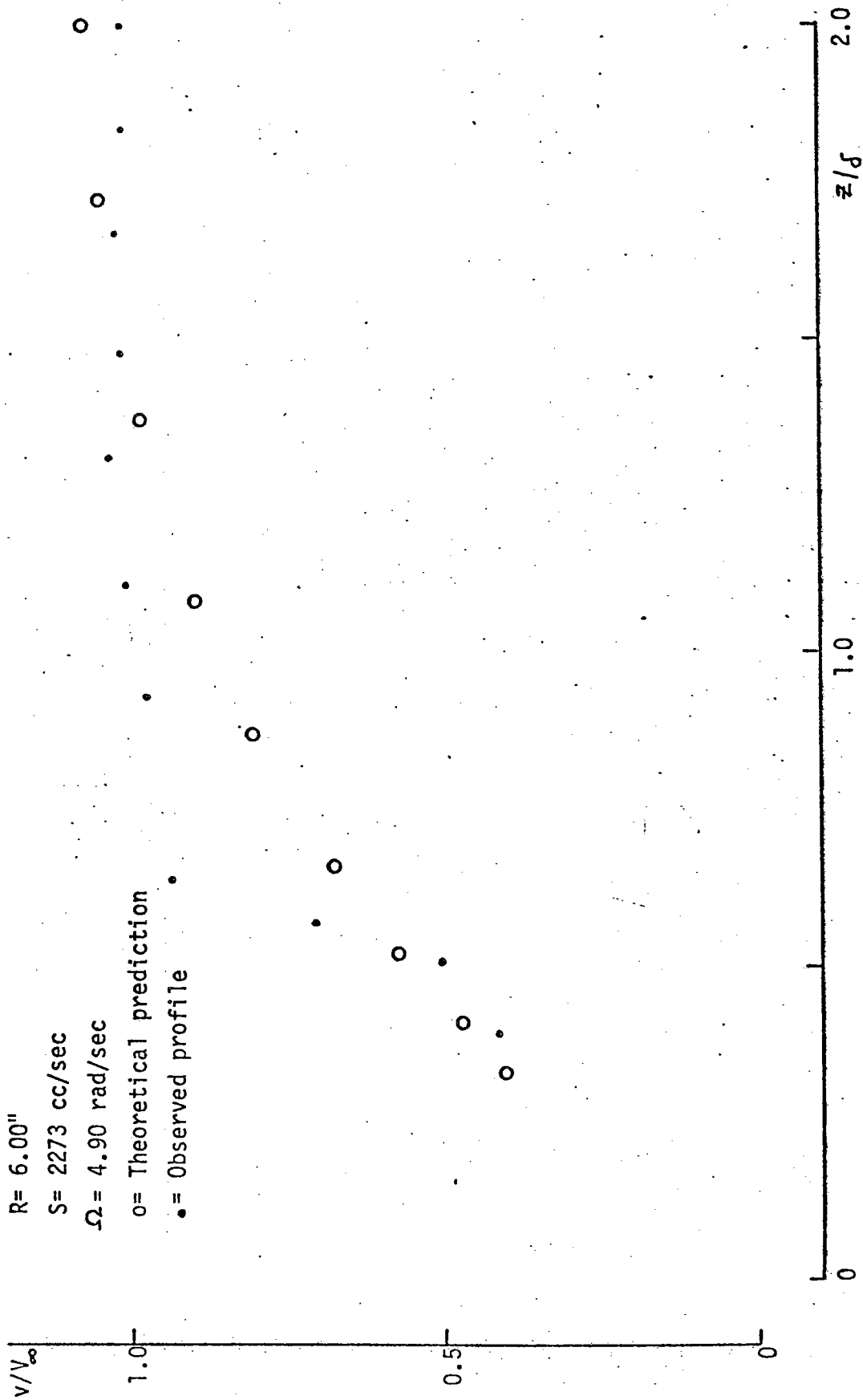


FIGURE 4.18B - EKMAN LAYER PROFILE,  $R = 6.00''$ , ZONAL VELOCITY

Reynolds number region of the tank.

Table 4-2 shows a synoptic view of all the zonal Ekman layer velocity profiles obtained. This chart gives the ratio of measured Ekman layer thickness ( $\delta_m$ ) to the theoretical prediction ( $\delta$ ), as well as the actual and theoretically predicted Reynolds and Rossby numbers (assumes  $\Gamma = 1.0$  in equation 4.2) Both sets of these parameters are included, since the wide diversity of measurement techniques in the literature leaves only the ideal Re and Ro numbers as invariant between different experimental setups. The measured Ekman layer thickness ( $\delta_m$ ) is the vertical distance at which the observed zonal velocity is 86% of the interior value ( $V_\infty$ ).

#### 4.2.3 Discussion

The profiles confirm that the observed Ekman layers in the annulus closely match the prediction of equations 4.4 and 4.5. However, the measured boundary layer thickness is typically 15 - 20% smaller than the theoretical value. At the smaller radii, significantly thinner layers are observed. The modification predicted by Barcilon (1970) is not apparent, although, only a few of the profiles are in a parameter range suitable for comparison.

Tatro (1966) was the first experimenter to conduct Ekman layer studies in an annulus. He estimated the boundary layer thickness by observing the vertical position of the maximum radial velocity and multiplying this height by  $4/\pi$ . This technique can lead to erroneous thicknesses, as a result of heat losses near the wall. This influence is apparent on all of Tatro's Ekman layer profiles. It can explain his observation that the boundary layer thickness

TABLE 4-2

## Comparison of Observed and Theoretical Ekman Layers

(Part 1)

<u>PROFILE #</u>	<u>r</u>	<u>FLUX cc/sec</u>	<u>ROT rad/sec</u>	<u><math>\frac{\delta}{M/\delta}</math></u>	<u>MEASURED</u>		<u>THEORETICAL</u>	
					<u>Re<sub>L</sub></u>	<u><math>\epsilon_L</math></u>	<u>Re<sub>L</sub></u>	<u><math>\epsilon_L</math></u>
1	0.19	1588	5.15	0.70	50.4	.52	139	2.05
2	0.25	2273	4.90	0.62	93.7	.68	153	1.79
3	0.28	903	5.28	0.89	26.6	.24	54	.54
4	0.28	1314	5.53	0.93	44.2	.40	79	.77
5	0.32	766	3.89	0.83	17.1	.21	42	.41
6	0.32	766	3.77	0.85	15.1	.19	42	.41
7	0.32	1561	3.77	0.81	36.2	.45	86	.84
8	0.41	766	5.02	0.77	12.3	.11	33	.21
9	0.41	1561	5.02	0.77	28.2	.26	68	.46
10	0.41	766	3.89	0.73	12.0	.13	33	.24
11	0.41	1561	3.89	0.74	26.7	.29	68	.51
12	0.41	766	6.28	0.76	11.5	.11	33	.19
13	0.41	1561	6.41	0.78	29.3	.23	68	.37
14	0.43	1040	7.47	0.77	21.0	.16	43	.24
15	0.43	1451	7.66	0.84	36.4	.17	60	.30
16	0.57	1382	5.28	0.91	18.3	.08	41	.20
17	0.57	2273	5.15	0.89	29.2	.13	67	.33
18	0.71	1451	5.40	1.06	16.3	.07	34	.13

TABLE 4-2

(Part 2)

19	0.71	1999	5.53	0.89	20.0	.07	47	.18
20	0.76	1040	6.34	0.81	9.1	.04	24	.08
21	0.76	1561	6.41	0.86	16.4	.06	36	.11
22	0.76	1314	3.89	0.75	11.8	.07	30	.12
23	0.76	1314	2.14	0.76	13.4	.10	30	.17
24	0.76	2246	2.14	0.77	20.9	.16	51	.29
25	0.89	1561	6.53	0.87	9.1	.03	30	.08
26	0.89	1040	6.59	0.83	6.1	.02	20	.07



decreases with increasing flux. If one considers the heat loss to be invariant with the forced convection rate (see Appendix II), an increasing interior velocity would necessarily lower the observed location of the voltage maximum.

Green and Mollo-Christensen (1970) show four velocity profiles in the boundary layer. They found no change in the measured Ekman layer thickness ( $1.7\delta$ ), with differing Reynolds and Rossby number combinations. Their work was limited by indefinite probe height location and a linearly extrapolated low velocity calibration (see Chapter III). Since Ekman boundary layer is of order 2mm in thickness, positional accuracy is a critical factor. Similarly to Tatro, none of their readings were corrected for wall losses.

Of the profiles shown in the literature, Caldwell and van Atta's (1970) provide the closest resemblance to theoretical predictions. In a Reynolds number range of 33 to 131, the authors found a negligible difference (less than 3.5%) in the observed Ekman layer height from  $\delta$ . For a value of Re equal to 662, a slight decrease (10%) in height was noted (assuming a labeling error in their figure 7). Surprisingly, Caldwell and van Atta make no corrections for heat losses to the wall. In their article, they comment that no loss was apparent to within 0.02 cm of the boundary. As seen in Appendix III, studies using a similar plywood boundary for the tank wall, showed a sizeable loss at a height of 0.07 cm. This discrepancy is unexplained. Caldwell and van Atta plot only a single radial profile, because of the problems discussed previously. The authors do not discuss any problems associated with side-wise forced convection (see Appendix II). In agreement with Green

and Mollo-Christensen, they find no systematic change of Ekman layer thickness with radius.

The results of Table 4-2 show no consistent dependence on any of the system parameters. Similarly, Caldwell and van Atta were unable to relate their boundary layer thicknesses to the interior flow characteristics. For the higher Reynolds' number range, Caldwell and van Atta found the layer thickness to decrease (up 15% for  $Re_L = 662$ ). Table 4-2 does not include any comparative values of  $Re_L$ .

Within the sink side-wall layer, a significant decrease of the Ekman layer thickness was noted. Of the two profiles taken, the higher Reynolds number flow produced the thinner boundary layer. In contrast, no changes were observed within the source side-wall layer. Caldwell and van Atta show no results under similar flow conditions. Although some of their observations are within the theoretically predicted sink side-wall layer region, no Ekman layer modification was detected. As mentioned in section 4.1, Caldwell and van Atta did not observe a side-wall boundary layer adjacent to their sink and their outer layer was distorted by eddy motions.

The differences observed between the results of Caldwell and van Atta and those of Table 4-2 can be explained to some extent by the interior flow field. All of Caldwell and van Atta's observations were taken for a radially increasing circulation distribution. In contrast, with the varied interior structure shown in figures 4.2-4.11 an alteration in the Ekman layer profiles is expected.

In analyzing the influence of non-linearities to the Ekman layer, profiles 10, 11, 23 and 24 are the most suitable. The results

show no important changes of boundary layer thickness and no increased "wiggleness" in the individual point profiles. In actuality, the higher Rossby number Ekman layers, generally exhibit a greater degree of uniformity than the rest.

#### 4.3 Summary of Mean Conditions

The experimental flow conditions match the theoretical predictions of Lewellen (1965) and Greenspan (1968) more closely than previously reported in the literature (Green [1968], Green and Mollo-Christensen [1970], and Caldwell and van Atta [1970]).

The most striking feature of the interior circulation profiles was the positive vorticity region apparent in the higher Rossby number observations. As predicted by linear theory, the circulation was virtually independent of radius for small Rossby number. In all experiments, sidewall boundary layers were observed adjacent to the source and sink. The source boundary layer was found to be significantly thicker than the predicted Stewartson  $E^{1/4}$  - layer. On the horizontal walls, Ekman layers are observed under all flow conditions. Their thickness is of order 15% thinner than the theoretical prediction.

Since the circulation is typically 60-70% of that predicted theoretically, the  $Re\#$  and  $Ro\#$  are greatly overestimated if an ideal profile is employed in their calculation. Notably, within the sink sidewall layer, the local Reynolds' number may be less than critical (see Chapter 2), while the opposite is true at a slightly greater radius. By assuming the existence of a theoretical Ekman layer thickness, errors (over-estimation) of 30-35% are possible within the

sink side-wall layer. The usual technique of observing Ekman layer instability has been to place a probe at one of the innermost radii, and increase the local  $Re\#$  (Tatro [1966], Green [1968]) to the critical value. Using this technique, the radius of the observed "critical" Reynolds number for instability onset may be underestimated. Most authors do not give the actual radius of observed instabilities, but mention that it is "close to the sink". To obtain accurate onset criteria, one must profile both the interior and Ekman layer flow to ascertain the maximum Reynolds' number position for each configuration. Increasing the flux at a random fixed position adjacent to the sink is a misleading method for observing instabilities.

## CHAPTER V

## Wave and Instability Phenomena

We now turn our attention to time dependent flows. As has been observed by previous workers, instabilities may occur in the Ekman layer for certain parameter ranges. These may be centrifugal instabilities and other linear or non-linear instabilities. An oscillation or wave phenomenon observed at a certain location does not necessarily imply that the flow is unstable at that particular place. Oscillatory disturbances may influence the flow at a distance by excitation of inertial waves or by propagating waves in the Ekman layers.

In order to obtain indications of where oscillatory disturbances originate and how they are distributed, a wave amplitude survey was made under varying flow conditions.(Section [5.1]).

Next, spectra of fluctuations were measured in a number of locations and for several values of flux and rotation rates. Section (5.2) describes a hysteresis in the dependence of spectra on flux. We then proceed to a discussion of a low Reynolds number instability observed previously by Arons, Ingersall and Green and analyzed by Stern. (Section 5.3). The remaining sections include a discussion of inertial waves and of Ekman layer instability.

### 5.1 General Oscillatory Activity

To give a picture of the distribution in intensity of oscillations the difference between the maximum and minimum zonal velocities was calculated for each mean flow measurement (fixed probes). This value was then divided by the steady velocity at the same location, and a "wave intensity percentage" was obtained. The results were subject to some estimation error (typically 5-10% for the lowest percentage shown), as they

were optically read from an oscilloscope.

### 5.1.1 Wave Intensity in the Interior and Side-Wall Regions

Table 5-1 shows the wave intensity percentage for four different flow conditions as a function of radial position ( $r$ ) for  $z=12\text{cm}$ . From this chart, the region of greatest wave activity was found within the radial limits of  $r=0.29$  and  $0.45$ . Also observed was a smaller local maximum at larger radii ( $r$  greater than  $0.81$ ). Only at the lowest flux values were the two peaks comparable in amplitude. Upon re-examining figures 4.2 - 4.11, one finds that the regions of high wave activity were those of  $\frac{dr}{dr} = 0$  or  $\frac{dr}{dr} < 0$ . Furthermore, the inner maximum of wave intensity was located in the area of largest local Reynolds numbers in the tank, as discussed in Section 4.3. This is also the region of the most unstable Ekman layers. At the outer maximum, no large eddies, of the type indicated by Caldwell and van Atta (1970), were observed. The increasing wave intensities at larger radii were partially due to the smaller mean velocities encountered within the source sidewall boundary layer.

### 5.1.2 Variation of Wave Amplitude with Height in the Ekman Layer

In a similar fashion to the preceding section, wave intensity was recorded simultaneously with measurements of the mean zonal velocity profiles in the Ekman layer. This technique allowed a comparison of the interior and boundary layer oscillatory activity. To facilitate this analysis, the wave intensity percentage evaluated at an "interior" position (most distant observation from the horizontal tank wall) was subtracted from the values calculated at each of the smaller heights. These residual differences showed significant

TABLE 5 - 1

Interior Wave Activity				
Wave Percentage (Peak-to-Peak)				
ROT(rad/sec):	3.14	5.02	6.28	6.28
FLUX(cc/sec):	1176	1724	765	2272
<u>r</u>	<u>%</u>	<u>%</u>	<u>%</u>	<u>%</u>
.21	2.9	4.2	2.8	5.3
.25	2.8	2.8	2.8	5.4
.29	4.5	4.2	3.7	5.6
.33	3.0	5.6	1.8	8.5
.37	2.8	10.0	2.8	12.8
.40	3.9	9.1	3.0	11.9
.45	2.1	7.2	3.0	10.7
.50	2.6	5.4	2.6	9.0
.54	2.0	7.0	2.6	9.0
.58	2.7	6.2	2.6	9.0
.61	2.6	3.6	2.6	7.3
.66	2.6	4.0	1.3	3.6
.71	2.6	4.0	2.4	3.6
.78	2.4	2.0	2.8	6.0
.81	3.4	4.5	5.8	6.8
.87	4.0	5.2	6.6	7.3

variation with height, and it was thus possible to isolate minima and maxima. Attempts to compare extremum positions to features of the velocity profile, such as critical points in the zonal velocity field, were unsuccessful.

Table 5-2 shows four series of "residual" wave activity (interior wave intensity subtracted) as a function of non-dimensional height. By isolating local minima and maxima from these distributions, and the remaining Ekman layers, an overall view of wave activity is obtained in Table 5-3. The relevant system parameters for each experiment are found in Table 4-2. An initial glance at Table 5-3 reveals a large amount of scatter in the location of extrema. However, by taking account of the mean interior flow conditions (see figs. 4.2-4.11), some similarity can be deduced for different Ekman profiles. The characteristics of the interior are arbitrarily separated into five groupings: two side-wall layers (A, E) a transition zone (B) and zones with absence (C) or presence (D) of positive interior vorticity. Although qualitative, this approach shows the influence of the mean interior flow field in determining the wave activity pattern in the Ekman layer.

As the method of observing wave amplitude is subject to some degree of uncertainty, one cannot infer any precise conclusions.

## 5.2 Wave Spectra

### 5.2.1 Introduction

Although the wave intensities gave an overall view of time dependent motion, a more detailed picture is required. To separate the characteristics of wave frequency components, frequency spectra were calculated. This allowed a description of the frequency components of wave motions at differing locations in the annulus.



TABLE 5 - 2

## Residual Wave Intensity in the Ekman Layer

(Part 1)

PROFILE #1		PROFILE #19	
<u>Height(<math>z/\delta</math>)</u>	<u>Percentage</u>	<u>Height(<math>z/\delta</math>)</u>	<u>Percentage</u>
0.40	4.0	0.42	0.0
0.52	5.0	0.51	+1.0
0.64	5.0	0.63	+2.0
0.77	0.0	0.74	+2.0
0.93	-3.0	0.87	+3.0
1.09	0.0	1.02	+2.0
1.21	-1.0	1.21	0.0
1.37	-1.0	1.42	0.0
1.57	0.0	1.69	0.0
1.75	1.0	2.00	+1.0
2.02	0.0	2.38	0.0
2.25	0.0	2.79	0.0
		3.10	0.0

Error:  $\pm 0.2$ Error:  $\pm 0.2$

TABLE 5 - 2  
(Part 2)

PROFILE #12		PROFILE #25	
0.40	5.0	0.41	-0.1
0.47	-1.0	0.46	-0.1
0.53	-1.8	0.52	-0.8
0.60	3.0	0.59	-0.7
0.66	0.0	0.66	-1.0
0.72	2.0	0.74	-2.2
0.80	0.5	0.87	-1.0
0.85	4.3	0.98	-0.1
0.93	2.6	1.08	-0.2
1.02	0.9	1.22	0.5
1.12	0.9	1.37	0.2
1.26	-0.8	1.56	-0.6
1.46	0.1	1.94	-0.4
1.74	1.1	2.15	0.0
2.04	2.0		
2.50	2.8		
2.94	2.8		
3.38	0.9		
3.82	0.9		
4.58	0.6		
5.63	0.0		

Error:  $\pm 0.3$

TABLE 5 - 3

Height of Maxima and Minima in Residual Wave Activity of the Ekman Layer  
(Part 1)

<u>PROFILE #</u>	<u>LOCAL MAX(<math>\bar{z}/\delta</math>)</u>	<u>LOCAL MIN(<math>\bar{z}/\delta</math>)</u>	<u>LOCAL MEAN IN- IOR FLOW CHARACTERISTICS</u>
1	0.64	0.93, 1.30	A
2	0.64		A
3	0.64	0.92, 1.55	A
4	0.88	1.44, 1.75	B
5	0.49, 0.85	0.58, 1.08	C
6	0.48, 1.01	0.59	C
7	0.48, 0.70	0.59, 1.48	C
8	0.57		B
9	0.51, 0.93	0.70	D
10	0.50, 0.93	0.66	D
11	0.57, 0.84	0.65	D
12	0.60, 0.85, 0.40	0.66, 1.26, 0.53	C
13	0.55	0.64	D
14	0.55, 0.72	0.66	D
15	0.77, 1.25	0.66	D
16	0.93, 2.09	0.50	D
17	0.49, 1.20	0.76	D
18	0.61, 1.29	0.75	C
19	0.87	1.42	C

TABLE 5 - 3

(Part 2)

20	0.62	0.70	C
21	0.53, 0.83	0.62	B
22	0.57	0.49	B
23	0.66, 1.03	0.51	B
24	0.40, 1.35		B
25	0.59, 1.22	0.52, 0.74	E
26	0.50, 0.73	0.58	E

KEY: A: Sink Side-Wall Boundary Layer.  
 B: Transition Region between A/C and D/E  
 C: Zero Vorticity Region  
 D: Positive Vorticity Region  
 E: Source Side-Wall Boundary Layer

The local Reynolds number, as defined by Tatro (1966), Faller (1965) and others, is included with each spectra in order to delineate any change that may have been attributed to previously predicted instability mechanisms. The experiments were planned so as to include a wide range of both Reynolds and Rossby numbers. These non-dimensional parameters were calculated assuming an interior potential vortex and thus derivable from system constants. They are as follows:

$$Re_L = \frac{S \delta}{2\pi R \nu \delta} = \frac{S}{2\pi R \nu} \quad (\text{equation 5.1})$$

$$E_L = \frac{S}{2\pi R^2 \Omega \delta} = \frac{S}{2\pi R^2 \nu^{1/2} \Omega^{1/2}} \quad (\text{equation 5.2})$$

where  $Re_L$  = local Reynolds number

$E_L$  = local Rossby number ( $Ro_L$ )

$S$  = volume flux in cc/sec.

and the other variables as previously defined. The rationale for using this derivation was the inability to measure the local boundary layer thickness and circulation profile for each of the spectra. An analysis of the actual velocity (non-dimensional) values (e.g., figures 4.2-4.11) showed that using the ideal profile for calculating the zonal speed was subject to a substantial error. The theoretical relations employed in equation 5.1 provided a means of cancelling the Ekman depth dependence. However, in equation 5.2, this was not true. By assuming the theoretical Ekman layer thickness, overestimates of up to 30% in  $\delta$  were possible (see section 4.2), but generally, 15% was typical.

The inertial frequency limit,  $2\Omega$  (Greenspan [1970]) was used to non-dimensionalize the wave frequencies. Frequencies above this limit were observed only in the region close to the sink. A typical spectral output showed the relative energy as a function of wave frequency in hertz. The energy scale was generally in arbitrary units (au), unless otherwise specified. Analysis using the auto-correlation computer was performed in the A.C. mode, and thus liable to a low frequency cutoff, from D.C. to 0.016 Hz (0.032 Hz double channel). As the typical rotational frequency was 1 Hz, this limitation was not crucial. Operating on the D.C. mode often lead to an excessive amplitude for zero frequency and a poor signal-noise ratio at higher frequencies.

All data were recorded on the eight-track magnetic tape recorder. Simultaneously, a short record of each signal was displayed on a 4-channel pen recorder.

### 5.2.2 Spectra Distortion and Hysteresis

The initial experiments (not shown here) produced a number of spurious spectra. This was attributed to the mean flow field being in a state of transition. By letting the fluid "spin up" and more crucially, allowing the rotation rate to stabilize, this shortcoming was alleviated. To avoid any gradual shift in the tank's angular velocity, delays much longer than the spin up time were required.

As mentioned in Appendix II, it was possible for large external disturbances to alter the mean and transient flows. Thus a distorted spectra resulted, when insufficient care was taken to avoid extraneous exterior forcing. This influence was significant only for

observations at the smaller radii. More specifically, the disturbances were apparent only in the region of constant circulation, radially adjacent to the sink side-wall layer. The perturbations were amplified in the high Rossby number zero vorticity flow field, which existed adjacent to the sink sidewall layer.

The spectra were found to depend on the time history of the flux, in the sense that a hysteresis effect was observed. Although unreported by previous workers, this phenomenon may have distorted their instability onset criteria. The hysteresis feature was noted during a series of transient flux experiments. Simply stated, on increasing the flux, a large amplitude wave appeared at a particular Reynolds number, and the wave did not disappear until the Reynolds number was far smaller than the onset value. In the spectra of figure 5.1 this feature is readily observed. The arrows (not  $2\Omega$ ) indicate whether the flux was reached by either an increase or a decrease from the prior setting. A quick appraisal shows that after the influence of a higher flux, the wave pattern is altered so as not to return to its previous state. Comparing spectra at a flux of 1451 and 1588 cc/sec. for ascending and descending changes, portrays this difference. Furthermore, the dominant wave amplitude was greater for fluxes lower than the original 1451 cc/sec. This implies that by imposing a higher flux rate, changes were effected in the flow conditions to such an extent, that on returning to an identical flux the dynamics have been altered. A simple analogy of this feature from mechanics would be the static and dynamic friction which differ for identical forcing, dependent on whether the object is





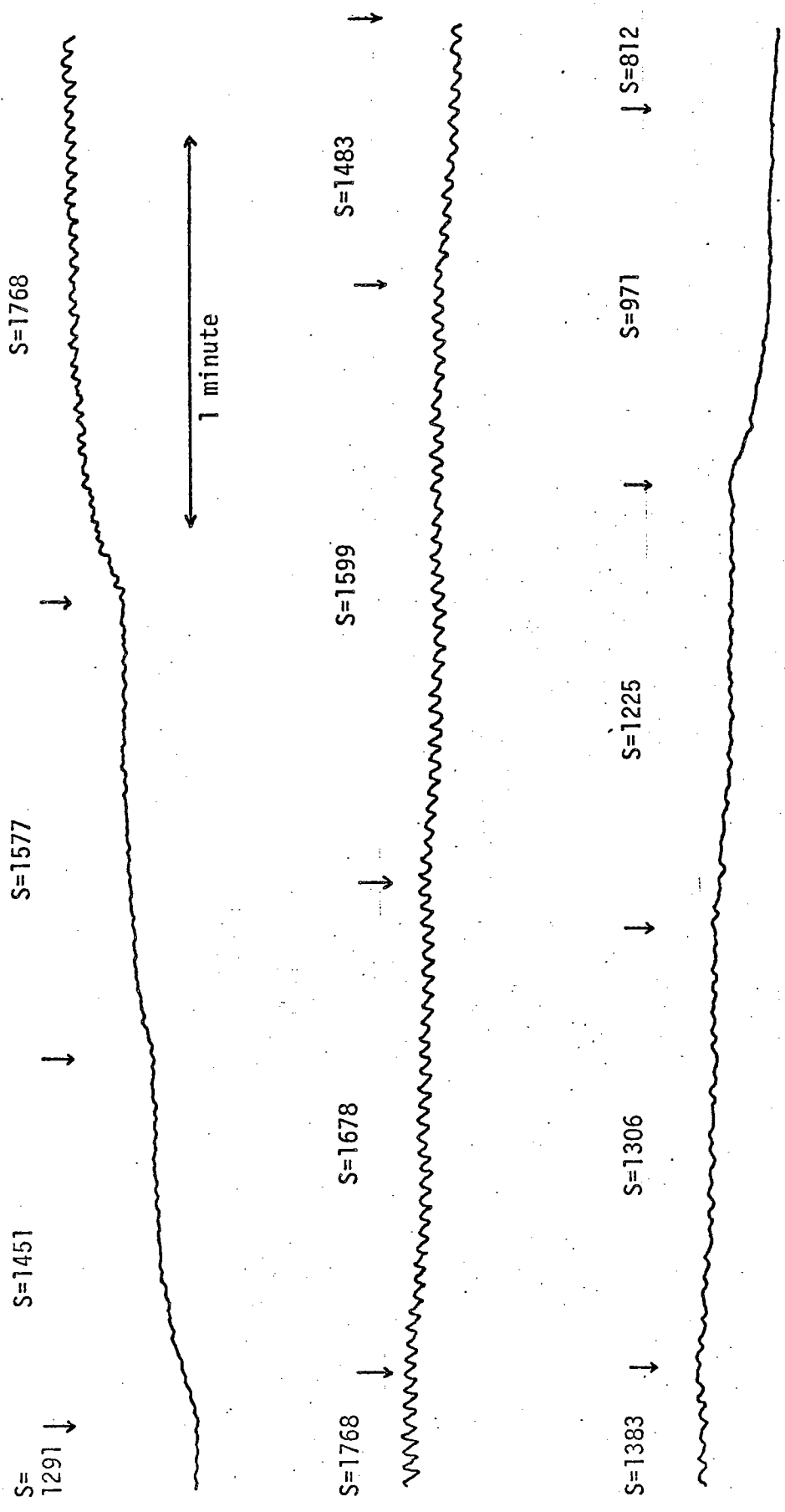
stopped or moving. Similarly, Coles (1965) in a Couette flow study found that the transition to turbulence occurred at a higher Rossby number than that at which it would disappear when conditions were reversed. Since a finite amplitude disturbance can exist and be unstable in a flow Reynolds number less than the initial value for production of infinitesimal disturbances, the present hysteresis results are explainable.

To obtain a more general view of this feature, the onset and demise of a certain wave was studied as a function of flux. Figure 5.2 shows the actual voltage response from the anemometer (with low amplification to give a wide mean flow range for differing volume flux). In this record, the wave onset occurred between 1577 and 1768 cc/sec., whereas on lowering the flux, a significant wave was observed to a value of 1225 cc/sec. These graphs clearly display the role played by hysteresis. Later, it will be shown how the observed frequency of some inertial waves changes with flux, but the hysteresis effect will nevertheless be apparent. The rotation rate in figure 5.2 was constant at 2.64 rad/sec. (which gave a somewhat higher Rossby number than typical in most of the present work). Since this feature is a non-linear effect, we expect it to be more apparent at the lower rotation rates.

The permanence of the hysteresis results was established by observing the configuration over an extended interval of time.

### 5.3 The "Body-Boundary" Modes

As mentioned in Chapter II, Stern (1960) had predicted the existence of an axisymmetric instability dependent both on local Reynolds



$\Omega = 2.64$  rad/sec      All Fluxes (S) in cc/sec.

$r = 0.73$

FIGURE 5.2

HOT WIRE VOLTAGE OUTPUT SHOWING HYSTERESIS EFFECTS

number and system Taylor number (reciprocal Ekman number). Both Arons, Ingersoll and Green (1961) and Stern (experimentally) found waves, with appropriate wave-lengths, satisfying the above constraints. Using a source-sink annulus, Hide (1968) also found ring-like stationary disturbances under certain conditions (even with slightly non-uniform depth). In explaining the wave's appearance, small differential temperature gradients ( $10^{-2}$ ) have been suspected of producing the observed structure. The reason why such temperature influences should be band limited is not discussed by any of the authors. In the present work, waves with some of these characteristics were routinely observed. The typical Taylor numbers were far greater than the critical value predicted by Stern. In comparing, it must be remembered that his theoretical work was directed to finding a lower limit for onset, rather than the observed values inherent for the higher modes. Examples of the detected waves are seen in figures 5.1 and 5.2. In these examples, the probe was located at a radius of 17.8 inches ( $r = .73$ ).

Initially, the spectra work focused on the inertial waves generated by class A and B (higher  $Re\#$ ) Ekman layer instabilities. Generally, with an increasing local velocity, one anticipates a Doppler-shift (due to advection) of the observed inertial wave frequency, as follows (Greenspan [1968]):

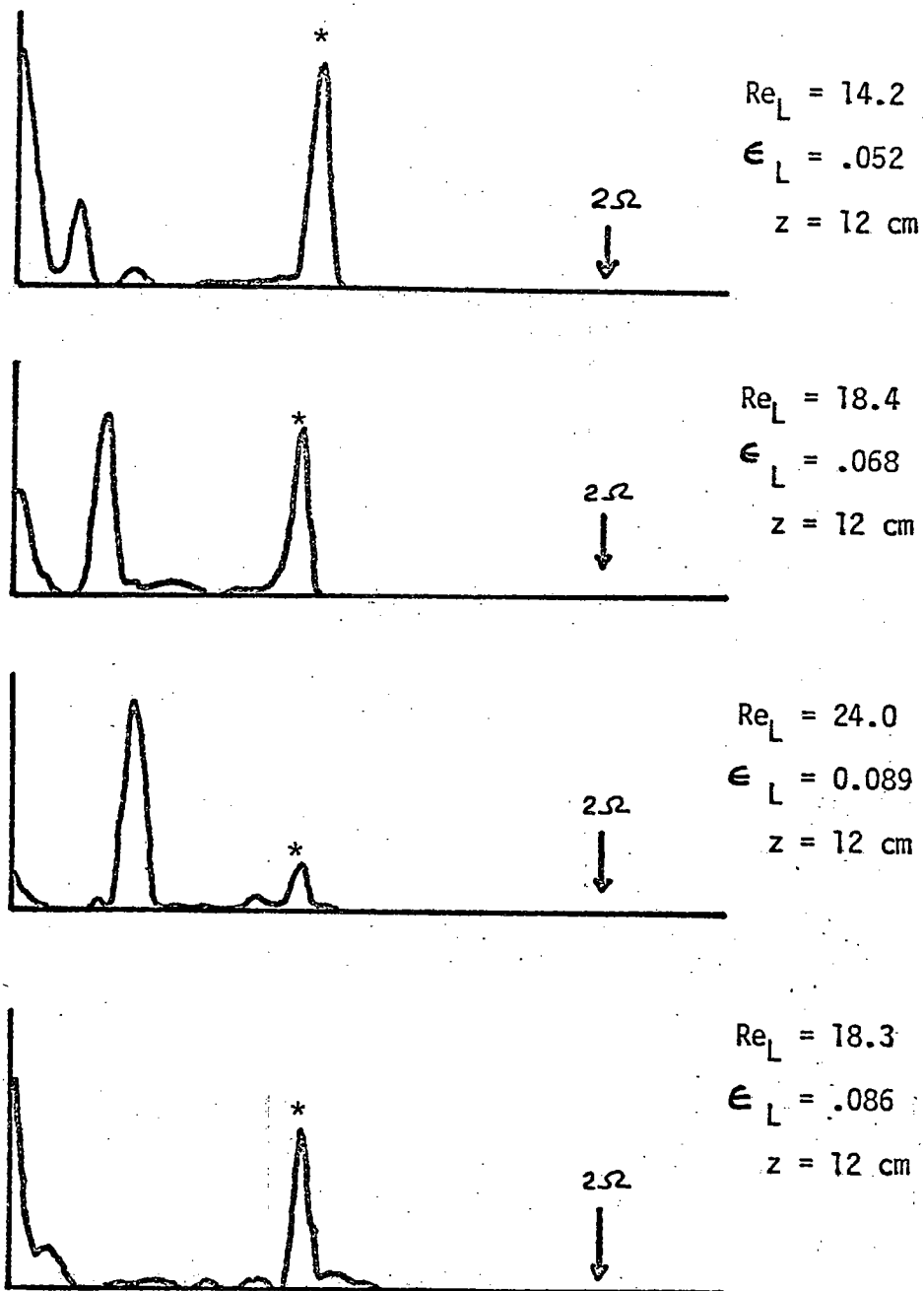
$$\sigma_{obs} = \sigma_0 + \epsilon_{sys} \vec{U} \cdot \vec{k} \quad (\text{equation 5.3})$$

where  $\sigma_{obs}$  = observed wave frequency (non-dimens)  
 $\sigma_0$  = unadvectioned wave frequency (n.d.)  
 $\vec{U}$  = advection velocity (n.d.)  
 $\epsilon_{sys}$  = system Rossby number  
 and  $\vec{k}$  = wave number vector (n.d)

Although the dominant wave in figure 5.1 (at lower fluxes) suffers an amplitude change, no frequency shift for increasing values of  $\vec{U}$  is observed. If the wave structure was axisymmetric (i.e.,  $\vec{U} \cdot \vec{k} = 0$ ), for a basically zonal interior flow, no Doppler effects would be observed.

A careful analysis of spectra at the larger radii (small Re#) showed similar axisymmetric waves, all of which had a non-dimensional frequency (with respect to  $2\Omega$ ) of  $0.52 \pm .01$ . This value was independent of Rossby number. However, the amplitude of these disturbances was found to depend critically on the local Reynolds number. While an approximate upper Re# limit was established, it was not possible to determine a lower one, because the vacuum system monitor was not operable at the required smaller fluxes. Figure 5.3 shows a number of spectra, for different parameter ranges, in which these low Re# waves were present, they are identified by asterisks.

For comparative purposes, a chart showing the previously reported work, present results, and the critical Taylor number found by Stern is shown in figure 5.4. From this diagram we can conclude that the occurrence of these waves does not depend critically on Taylor # (at least in higher Ta# range) and that the Reynolds numbers obtained presently are significantly larger than those of Arons. Although Arons' results were generally in a  $Re_L$  \*range of 1.6 to 3.6, he



\* : Wave Observations

FIGURE 5.3

SPECTRAL REPRESENTATION OF LOW REYNOLDS NUMBER WAVES

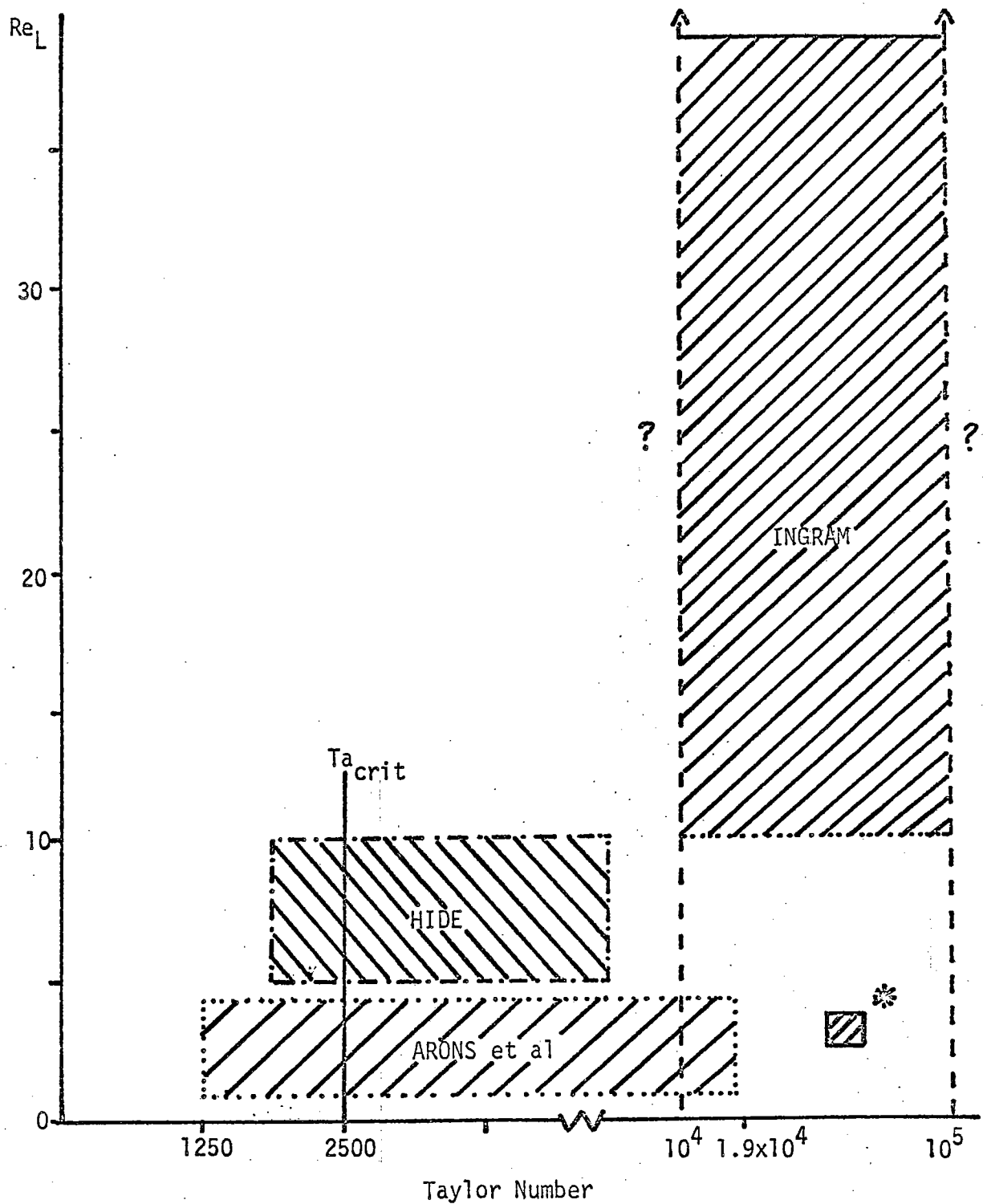


Figure 5-4. Observed Low Reynolds Number Waves.

mentions having observed an indication of waves up to a value of 10. A slight difference in the comparisons can be attributed to the method of the  $Re\#$  computation, which are related as follows:

$$\frac{Re_L^*}{Re_L} = 2 \left( 1 - \frac{R^2}{a^2} \right) \quad (\text{equation 5.4})$$

where  $Re_L^*$  = Arons et al (1960) local  $Re\#$   
 $Re_L$  = local  $Re\#$  as defined in eq. 5.1  
 $R$  = local radius (dimensional)  
 $a$  = outer tank radius.

It is important to note that the results quoted by Arons are all minimum  $Re\#$  for the occurrence of waves, and therefore do not preclude a similar wave structure at higher values. Hide (1968), using a relation identical to equation 5.1, found the waves in a Reynolds range of 5-10, for Taylor numbers from 1700 to 6800. The starred data in figure 5.4 were observed with a reversed radial flux. This paralleled Aron's work to some extent, since he used a centrally located funnel for fluid injection. There was no sink to remove the water. All of the values quoted in the present work are those of occurrence, rather than minima. The question marks in figure 5.4 imply an arbitrary boundary, as no experiments were performed past these limits.

The most interesting result of the present work is the existence of an upper limit, past which these low Reynolds number waves decrease to insignificant amplitudes. It is notable that no definite upper

Re# limit has been reported previously in the literature. This maximum value in Re# was found to be approximately 35.0. In contrast to recent Ekman layer instability work, the Reynolds # range of these waves is much lower than the "pure" boundary waves reported by Faller (1963) and others, where critical values of  $Re\#_L = 50-100$  are typical. It may be important to note that the low Reynolds number waves occurred only for small system Rossby numbers (less than 0.15).

Although the present wave observations were taken in the interior of the tank, the local Ekman layer characteristics under these conditions, are also of interest. Profile #18 in Table 4-2 is a suitable example. The observed boundary layer thickness of this profile was the only one recorded, that was larger than theoretical prediction. The wave intensity chart (Table 5-3) shows this Ekman layer profile to have the wave characteristics of a zero vorticity interior.

Since the interior vorticity structure played a definite role in the Ekman layer characteristics, it is expected to assume an equally important control over the Stern (low Reynolds number) waves. This influence was readily apparent in the wave observations. In fact, any significant departure from a zero vorticity interior (see fig. 4.2 - 4.11) inhibited the "Stern" wave production. This accounted for the failure to observe waves in some regions where the  $Re\# - Ta\#$  constraints were satisfied. The absence of waves adjacent to the source agrees with previously reported work.

To further investigate the ring-like structure of these waves, cross-correlations between probes at the same radius (but azimuthally separated) were taken. Without exception, the waves showed no phase lag between the two positions. Thus, by combining the av-



ailable results, "Stern" waves were found to be prevalent and of an entirely different nature than the inertial waves discussed by Green (1968), Tatro (1966) and others. Surprisingly, previous work with the higher  $Re\#$  instabilities fails to report the existence of these "Stern" waves, although conditions were suitable in many cases. It would seem that their attention was focused solely on the inner radial positions.

Additionally, Arons found (not detected in the present work) small zonal waves, which formed on the concentric rings, at the higher fluxes and lower viscosities (higher  $Re\#$  range). However, he was unable to specify any onset criteria. The present results do differ from Arons' work substantially in one area, that is in time-dependence. Although previous authors mention the "slow" motion of these waves, a definite radial fluctuation is noted in the observed waves, with frequency 0.52 (non-dimensional). Both cross-correlation techniques and Doppler shift results authenticate the waves' ring-like structure. We are left with the conclusion, that the wave structure is almost identical to that previously reported, but not stationary. Since the probe executes a concentric path, stationary axi-symmetric waves would not be detected in any case.

#### 5.4 A Series of Representative Spectra of Velocity Fluctuations.

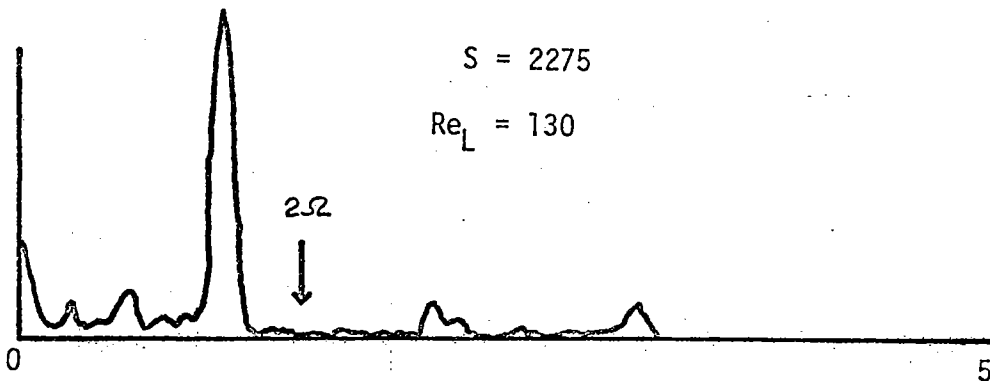
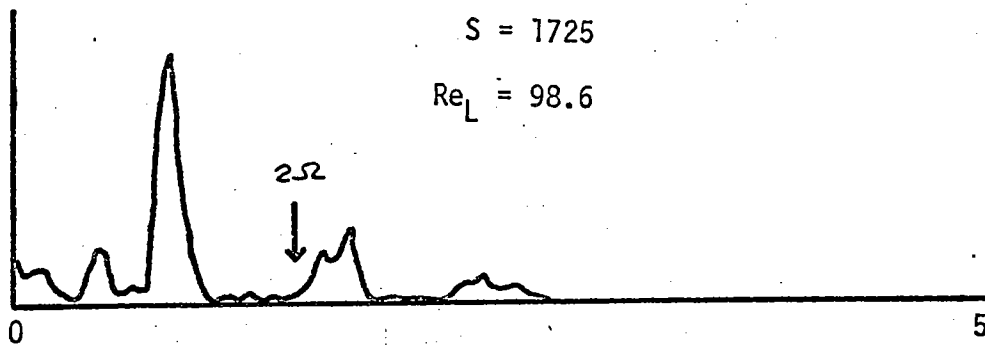
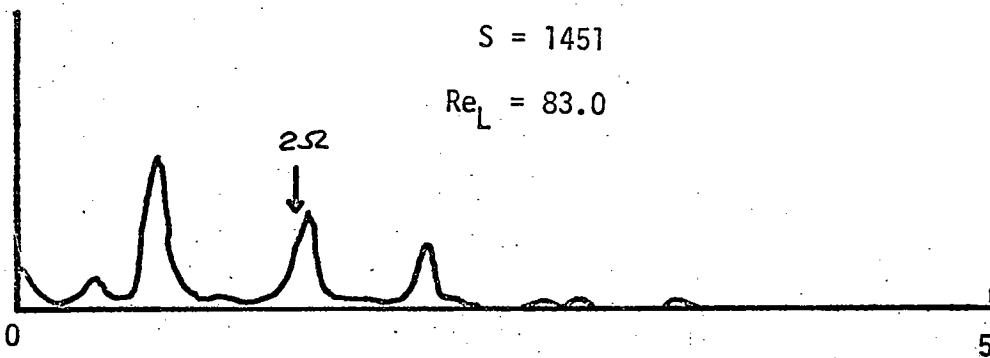
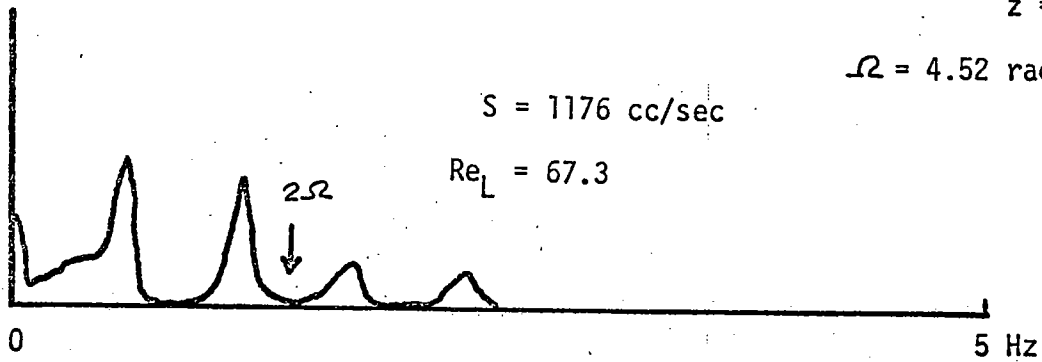
Looking at all the spectra, it was difficult to separate specific features. For this reason, a particular series recorded at a constant rotation of 4.52 rad/sec. with varying flux and position, were analyzed rigorously. According to Green (1968), we should expect the dominant wave peaks of these

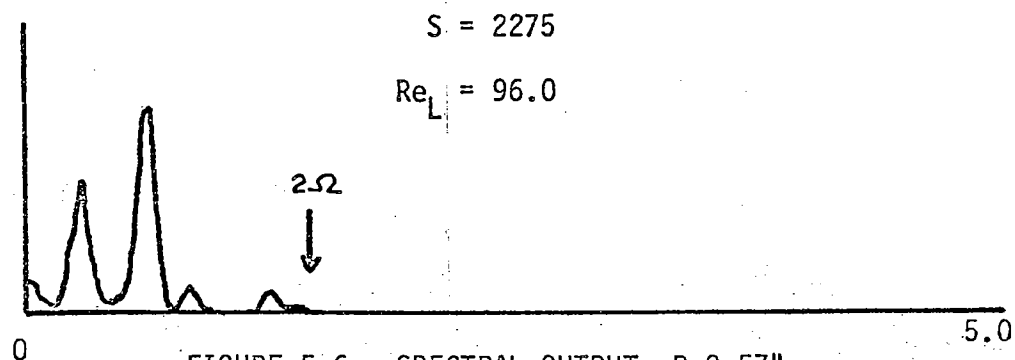
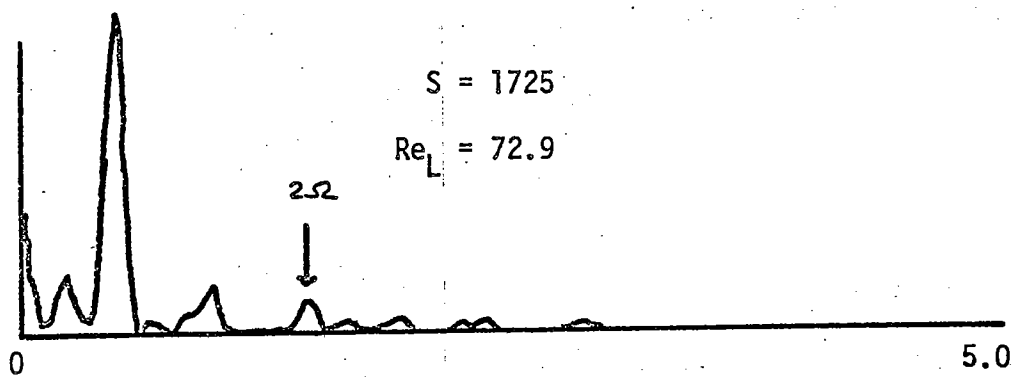
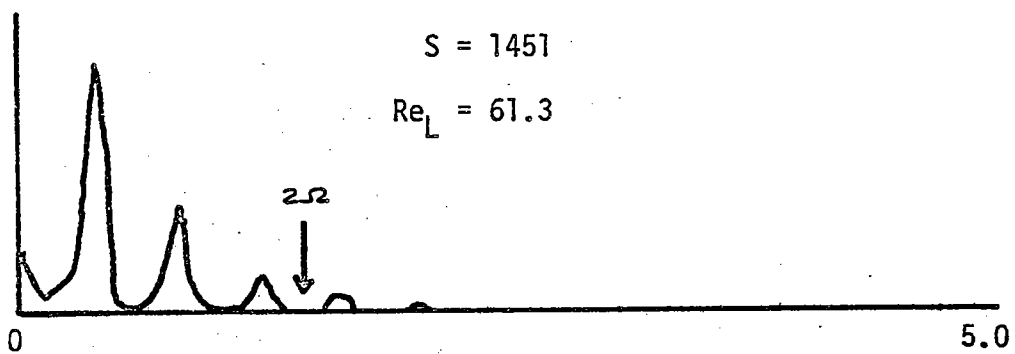
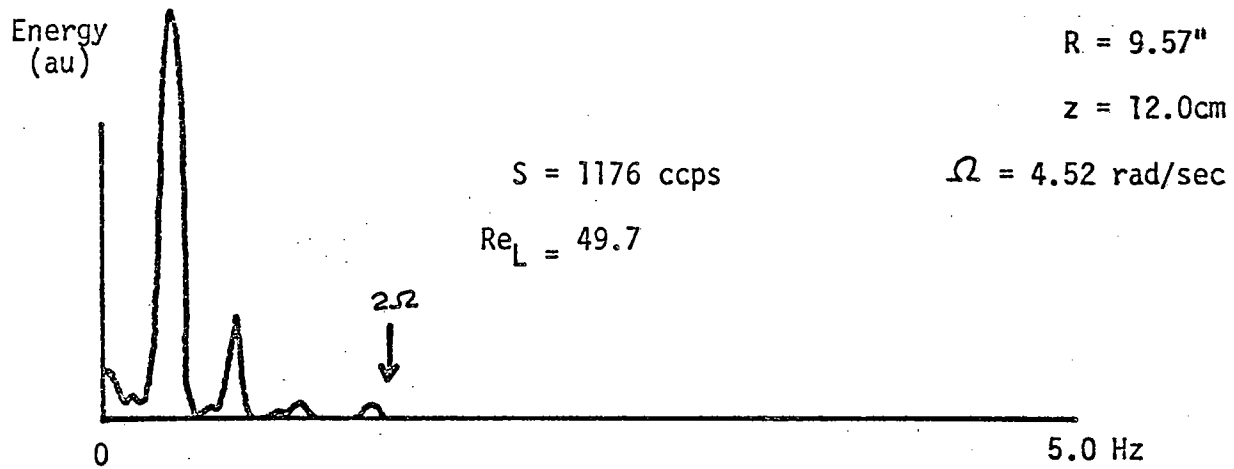
spectra to be frequency invariant with radius, for conditions of constant flux and rotation. Implicit in this finding is that the inertial waves are axisymmetric, and thus unaffected by the differential Doppler shifting of the radially structured zonal flow. In a later work, Green and Mollo-Christensen (1970) found that the wave frequency increased linearly with system Rossby number, indicating non-axi-symmetric waves. From their results, such a response is verified, but as the parameter range was limited, only further work could test its generality. This was accomplished by varying the flux, to obtain a complete range of Reynolds and Rossby numbers. The observed pattern was similar to the findings of Green and Mollo-Christensen for the small  $\epsilon_L$  ranges, but generally, a more complex (although regular) dependence was present.

Figures 5.5 - 5.10 show for individual radii, the influence of a flux increase on spectral characteristics, for constant rotation. These observations were recorded at the mid point ( $z = 12\text{cm}$ ) of the tank interior. The inertial frequency limit ( $2\Omega$ ) is marked on all figures. As a means of comparison, figure 5.11 presents the same flow conditions as shown in diagram 5.7, but within the Ekman layer (at a height of 1.0mm). Summarizing the positional influence, figure 5.12 combines the individual spectra for varied radii in the case of constant flux. This allows a view of any radial variation of the dominant waves under otherwise uniform conditions. From these spectral results, the dominant wave peaks at  $R = 9.57''$  ( $r = 0.39$ ) and  $13.80''$  ( $r = 0.57$ ) are seen to be essentially frequency invariant. Generalizing from all the observations, inertial waves whose frequency is independent of radial position were found

Energy  
(au) $R = 7.07''$  $z = 12.0$ 

cm

 $\Omega = 4.52$  rad/secFIGURE 5.5 - SPECTRAL OUTPUT,  $R=7.07''$

FIGURE 5.6 SPECTRAL OUTPUT,  $R=9.57''$

Energy  
(au)

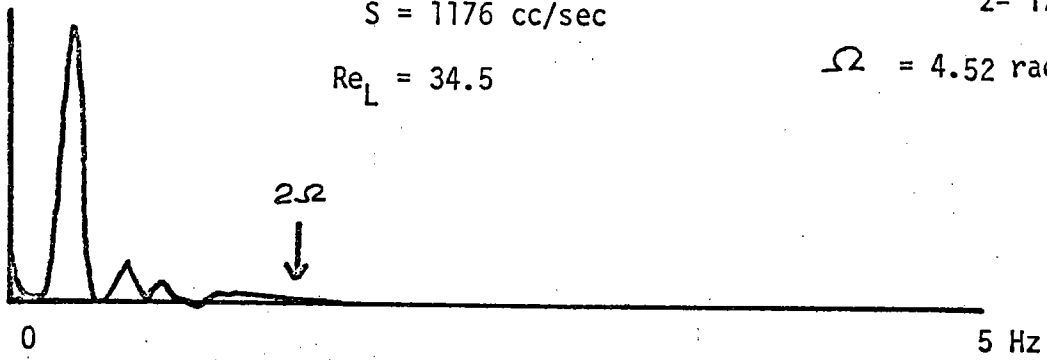
$R = 13.80''$

$z = 12.0\text{cm}$

$\Omega = 4.52\text{ rad/sec}$

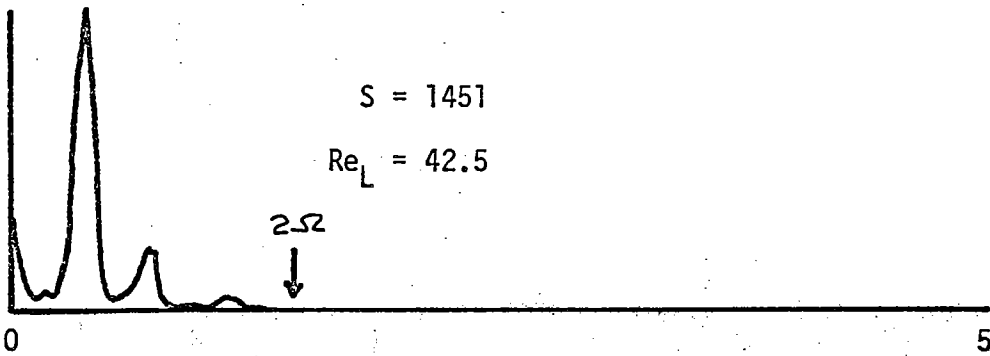
$S = 1176\text{ cc/sec}$

$Re_L = 34.5$



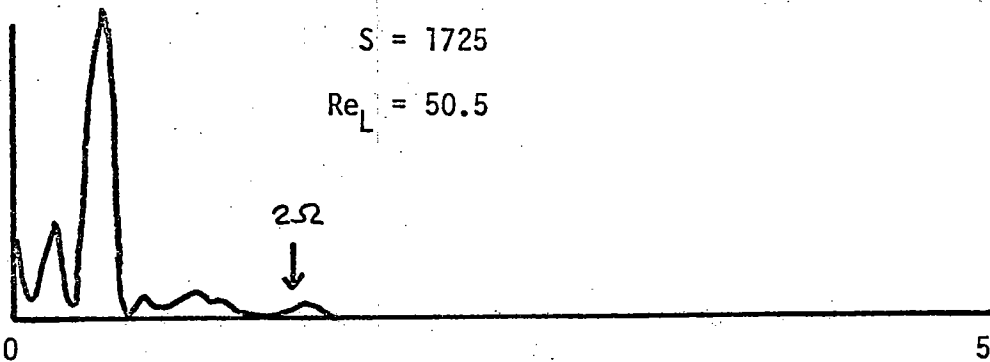
$S = 1451$

$Re_L = 42.5$



$S = 1725$

$Re_L = 50.5$



$S = 2275$

$Re_L = 66.6$

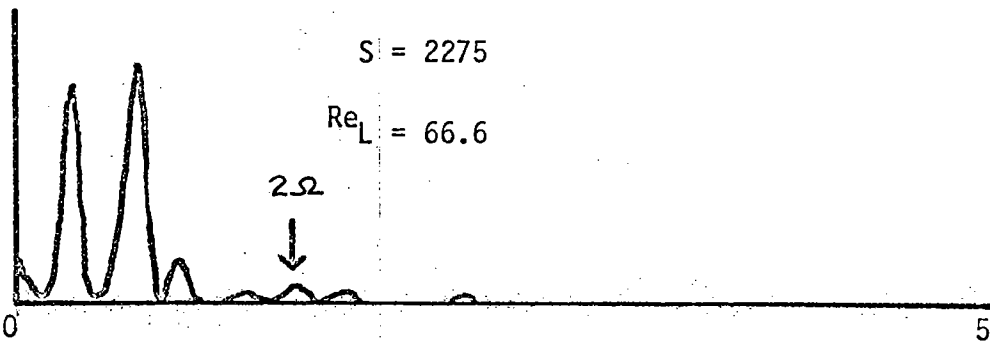
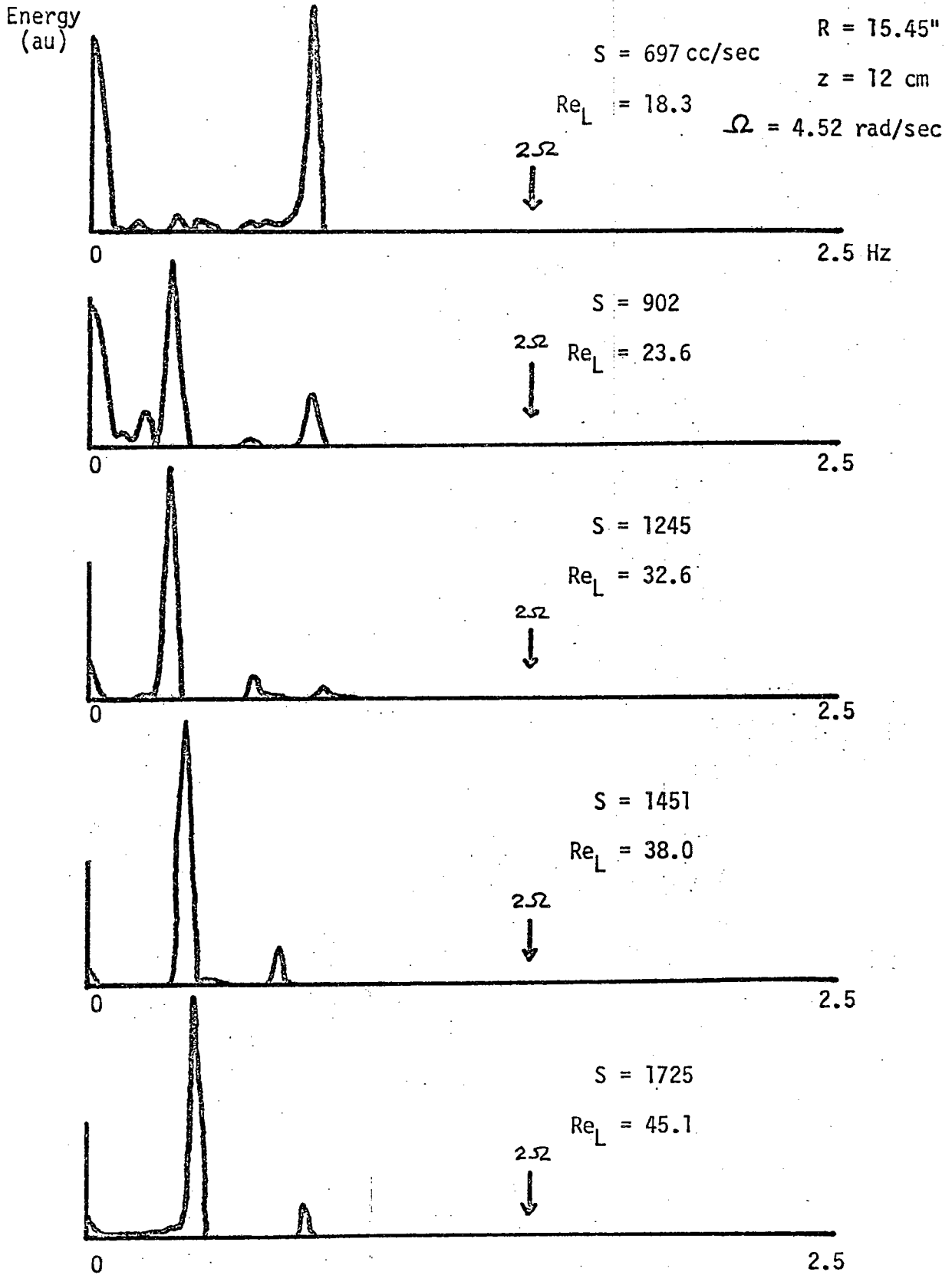
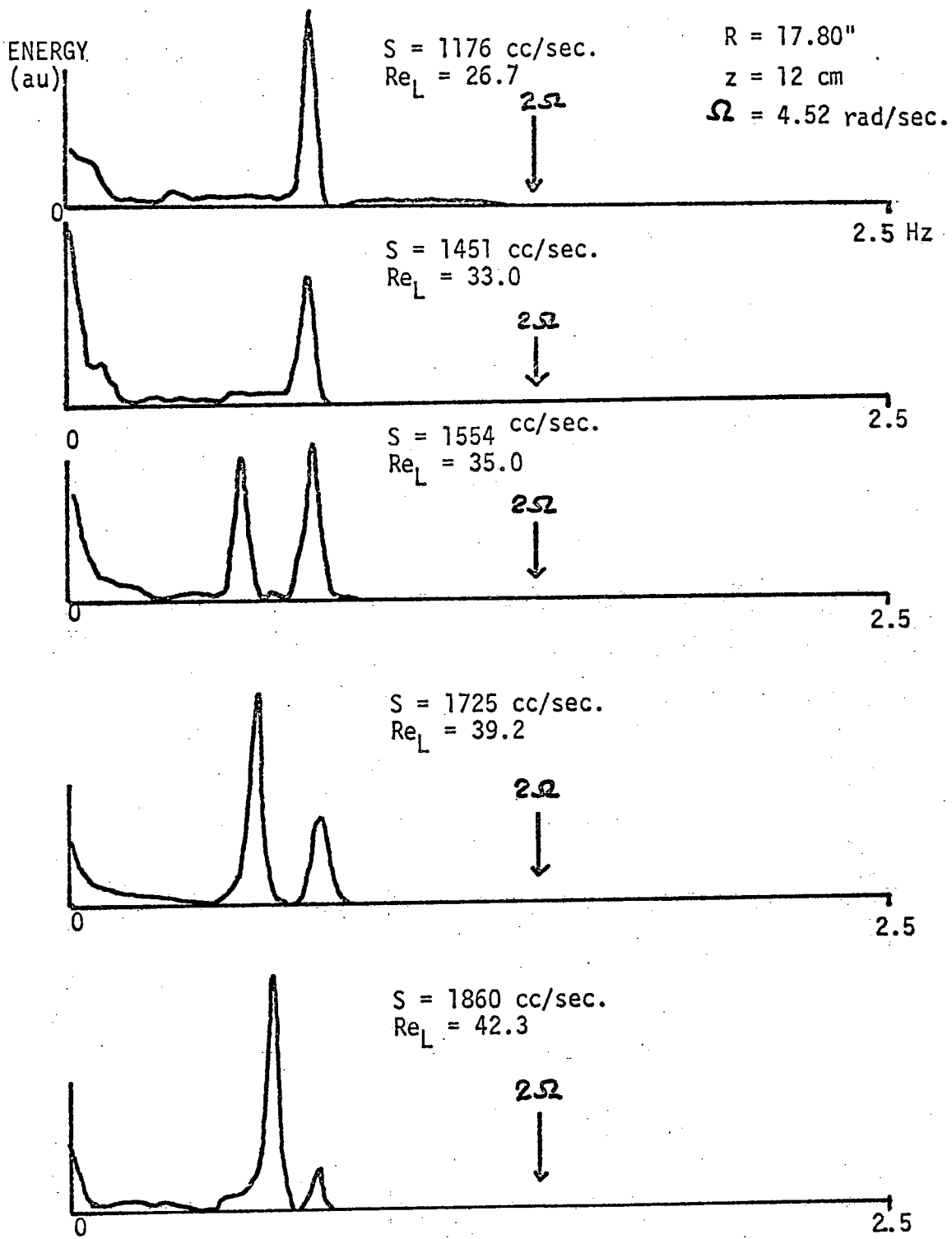
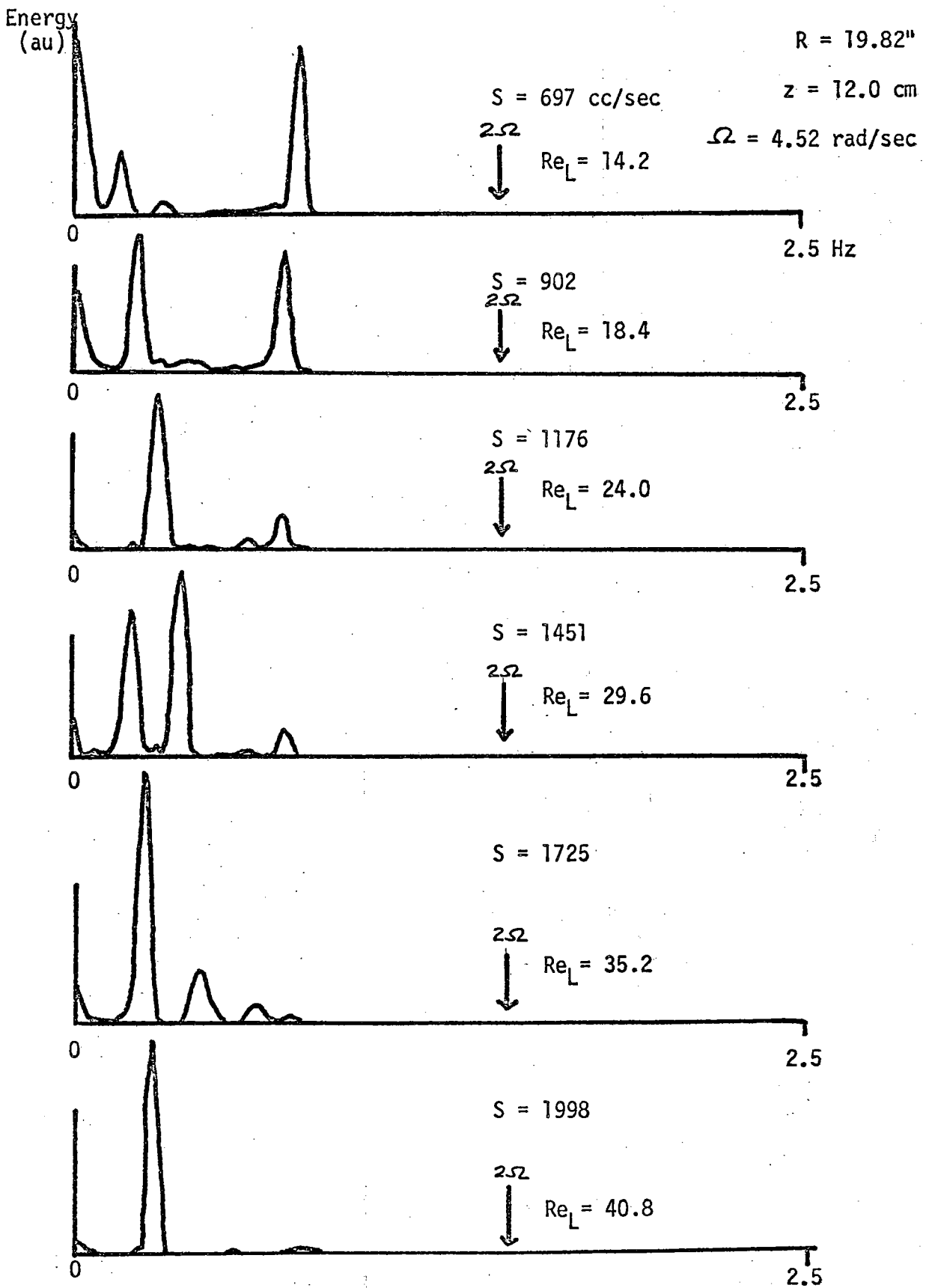


FIGURE 5.7 SPECTRAL OUTPUT,  $R=13.80''$

FIGURE 5.8 SPECTRAL OUTPUT,  $R = 15.45''$

FIGURE 5.9 - SPECTRAL OUTPUT,  $R = 17.80''$

FIGURE 5.10 - SPECTRAL OUTPUT,  $R=19.82''$



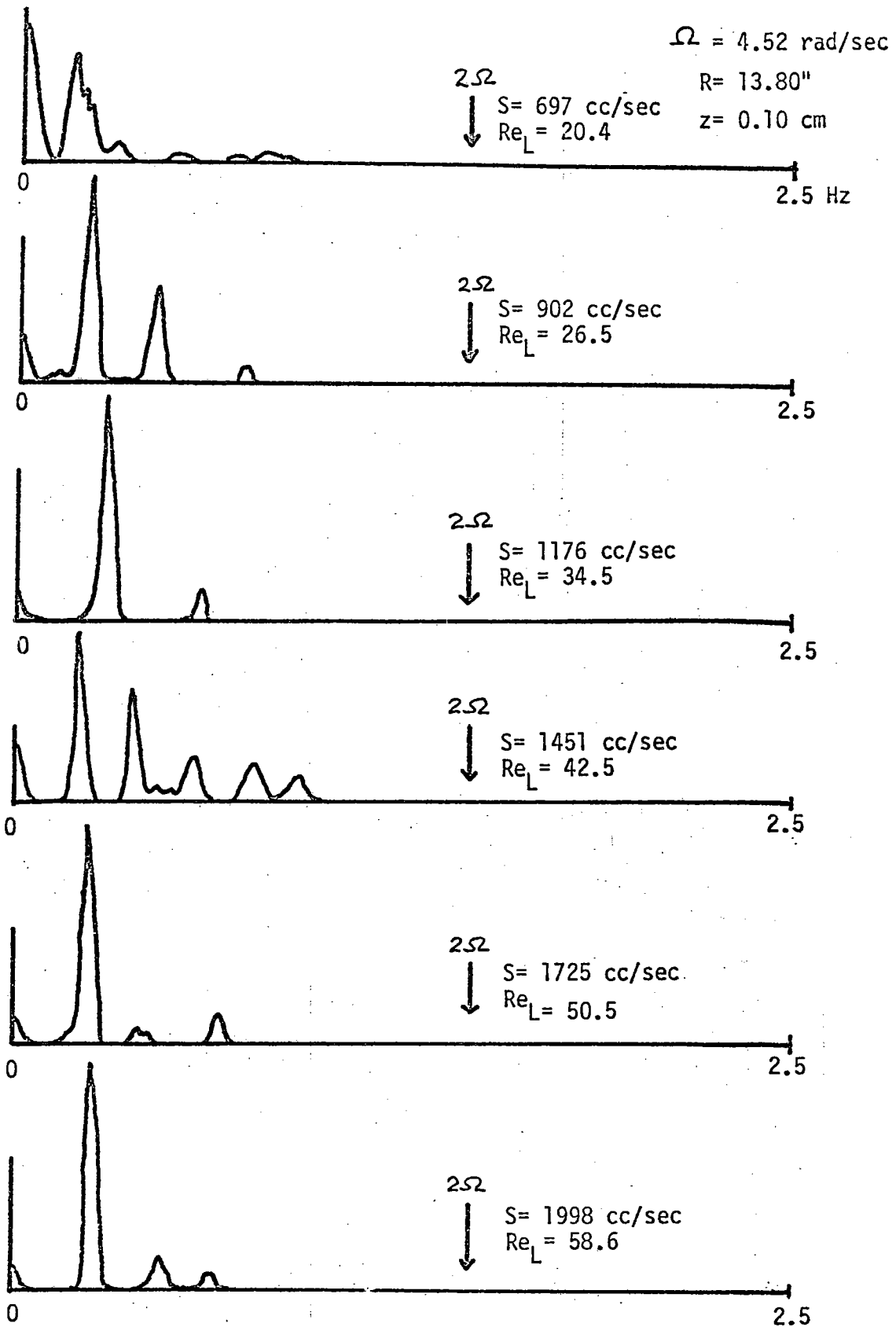


FIGURE 5.11 - SPECTRAL OUTPUT,  $R=13.80''$ ,  $z=0.10 \text{ cm}$

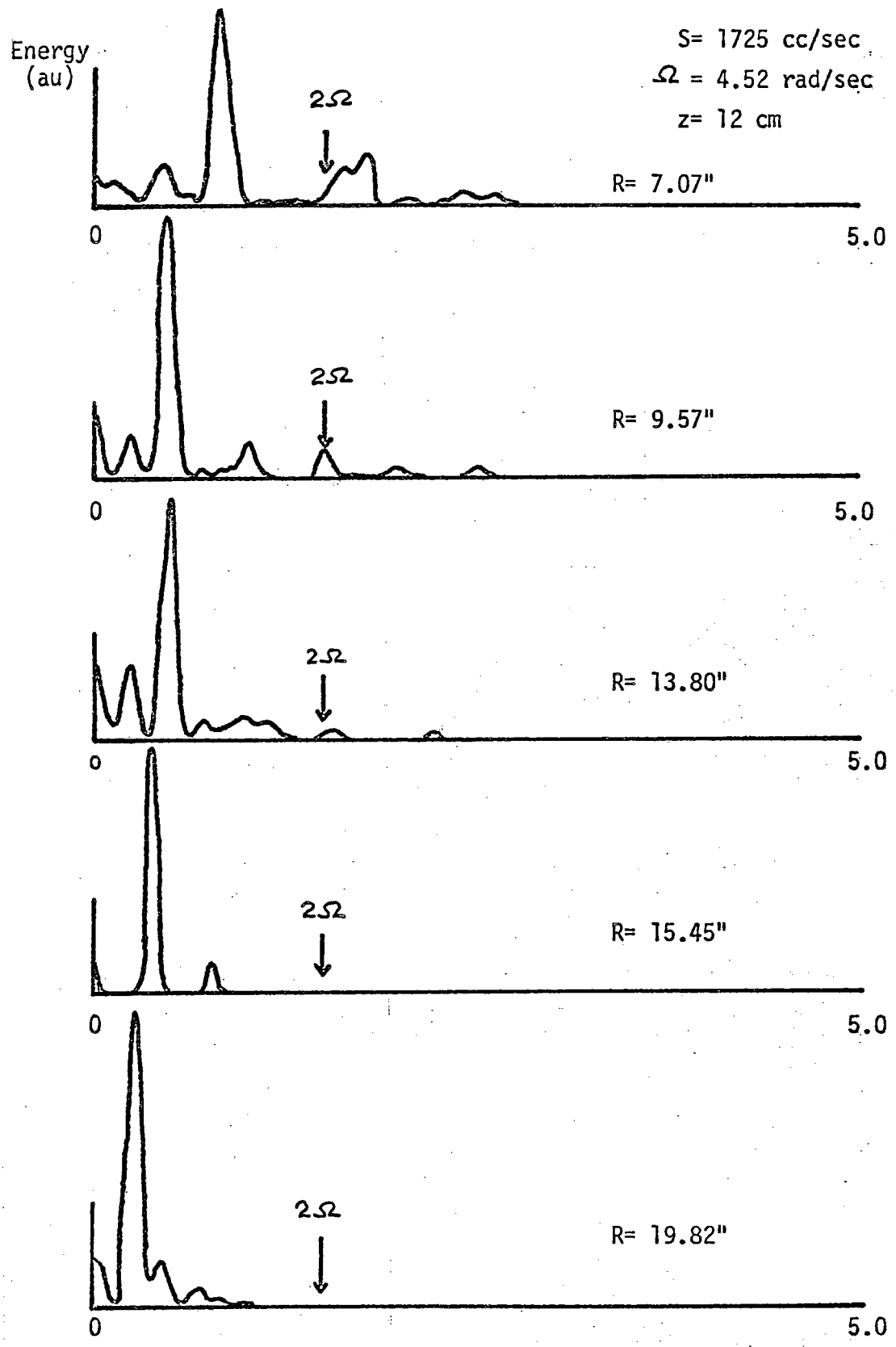


FIGURE 5.12 - SPECTRAL OUTPUT FOR CONSTANT FLUX, 1725 cc/sec.

only in the mid-radial observations (e.g.,  $r = 0.39, 0.57$ ). This range coincides with the region of increasing  $\Gamma$  (see figure 4.8).

The results also show, that for increasing flux, the frequency of the dominant waves grew linearly with flux over a limited range at the larger radii. In these cases, a lower frequency wave superceded (in amplitude) the originally dominant one, at some specific flow rate. This change can be very abrupt, with the transition of energy to lower frequencies being accomplished over a narrow range of flux. For example, in figure 5.10, the transition to a lower frequency occurs between 1451 and 1725 cc/sec. In contrast, figure 5.7 shows that under identical flow conditions (at a smaller radius) no such transition was recorded, although the final two spectra do suggest an imminent change above 2275 cc/sec.

The present results were compared with those of Green and Mollo-Christensen, by plotting non-dimensional frequency (with respect to  $2\Omega$ ) against system Rossby number. The system Rossby number is defined as follows:

$$\epsilon_{sys} = \frac{S}{2\pi R_0^2 v^{1/2} \Omega^{1/2}} \quad (\text{equation 5.5})$$

where the parameters are as previously defined. The resulting graph is shown in figure 5.13. Excluding the low Reynolds number waves (of section 5.4) which are readily separable by their constant frequency and lack of Rossby number dependence, the remaining points form a series of lines. Additionally, some observations with constant radius, but changing rotation, (not shown) demonstrate a similar multiple line response. It can be discerned from the diagram how Green and Mollo-Christensen with a limited number of points, may have found one line

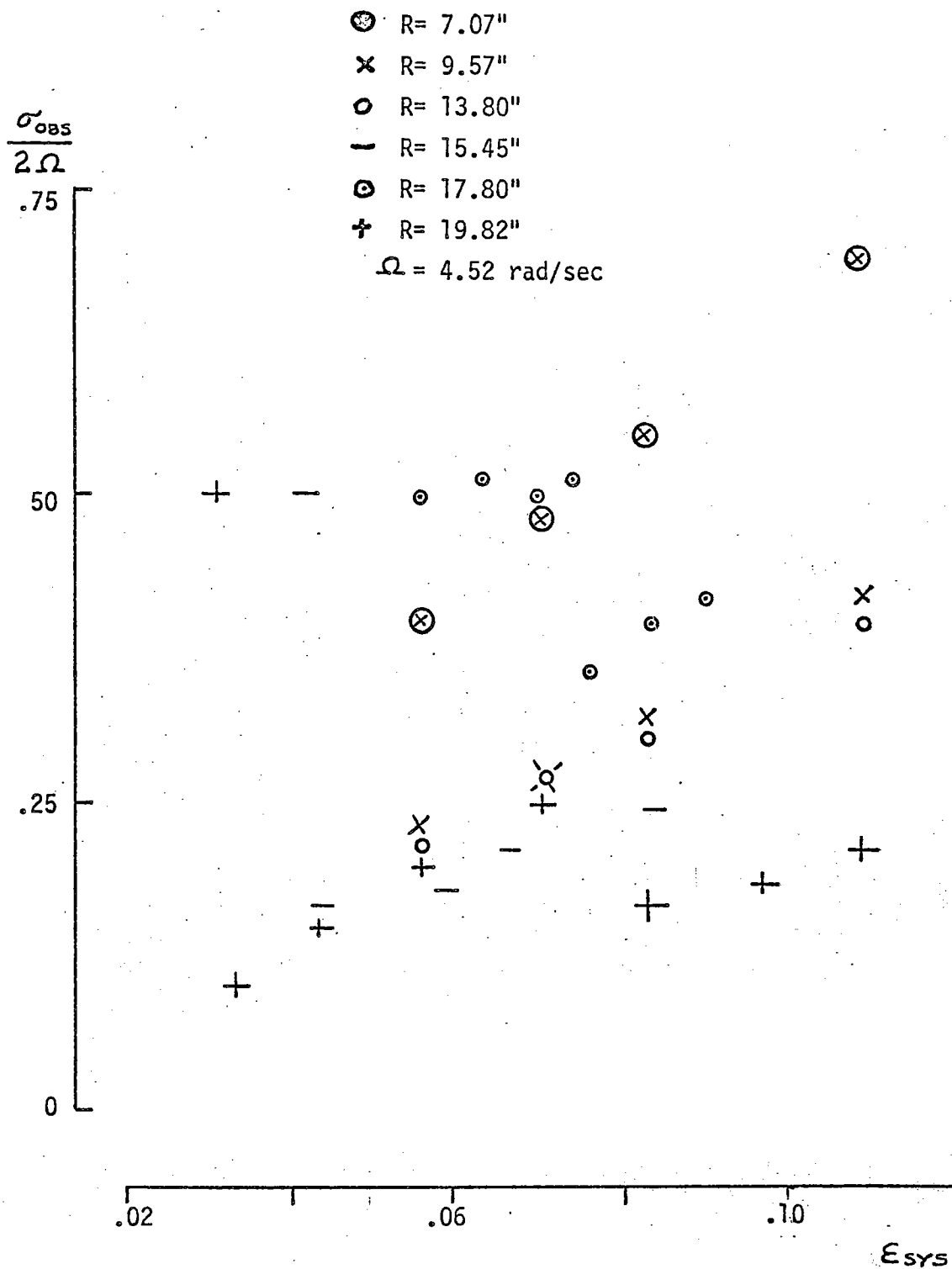


FIGURE 5.13 - COMBINED SPECTRAL RESULTS vs. SYSTEM

ROSSBY NUMBER

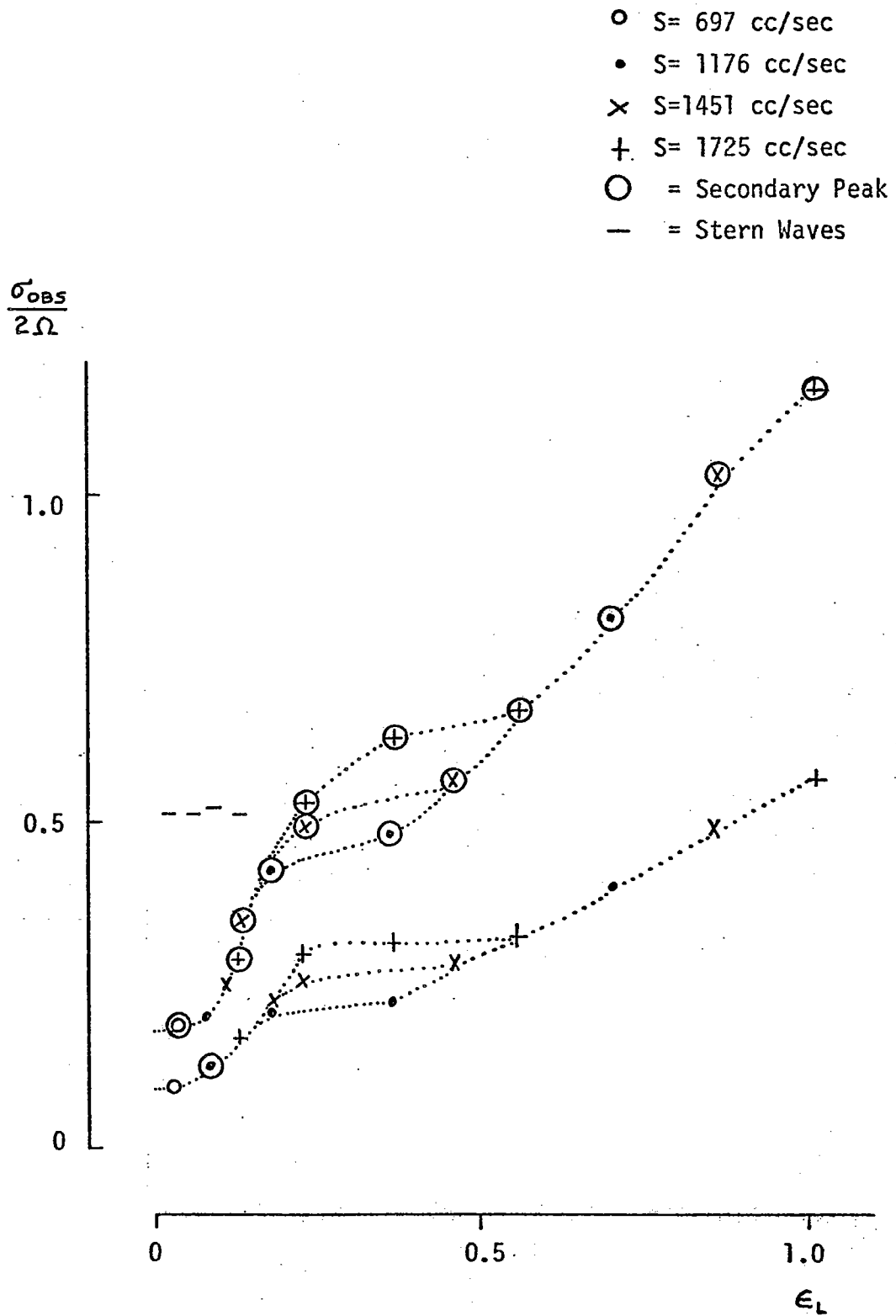
to satisfy their results. In general, the slopes obtained were nearly constant and the same order of magnitude (and sign) as their work (correction was made for different non-dimensionalization). It must be remembered, however, that Green and Mollo-Christensen utilized a single radius and a narrow flux range in plotting their graph.

An overall view affords the following comment: the observed waves can be axi-symmetric or non-axi-symmetric, the latter being the predominant by far. In the past, "Stern" waves may have been misinterpreted as axi-symmetric waves produced by the Class A instabilities. The observed frequency of both waves is invariant with radius. However, the low Reynolds number wave is a local phenomenon, dependent on suitable conditions in the interior and the Ekman layer, whereas an axi-symmetric inertial wave may be ubiquitous.

Although some systematic variation of  $\sigma/2\Omega$  with  $\epsilon$  is apparent in figure 5.13, it is difficult to explain the dynamics from this picture. A more systematic representation of the results was obtained by plotting the observed wave frequency versus the local Rossby number,  $\epsilon_L$ , for contours of constant flux. In figure 5.14, the values graphed in fig. 5.13 were re-plotted with this change of abscissa. Also included in this diagram were the second largest amplitude peaks from each spectra. These points are designated by an enclosing circle. Even at first glance, the results separate into distinct groups, some of which are inertial waves whose frequency increases (not always linearly) with  $\epsilon_L$ , and another set made up of the "Stern" waves, which are independent of  $\epsilon_L$  (and not of present interest). Excepting the middle Rossby number range, the wave frequencies fall on two lines. By back-extrapolating these lines to zero Rossby number, the unadvected

inertial wave frequencies are obtained (.09 and .18 in this case). This follows from equation 5.3. The branching of each line is only an artifact of calculating  $\epsilon_L$  from the theoretical velocity profile. As we have seen in Chapter IV, the circulation profile showed greater distortions from theory for increasing fluxes. In actual fact, for the mid Rossby number range shown in figure 5.14, the zonal velocity was almost constant with radius for each of the higher fluxes. It can be readily seen how Green (1968) observed a wave, whose frequency did not change in the mid-radial positions, and erroneously concluded that it was axi-symmetric. Since the observed frequency of the two inertial waves detected in figure 5.14 was influenced by differential advection, we can assume that they were non-axi-symmetric in nature (see equation 5.3). By changing the rotation rate, for a constant flux and position, the additional points obtained coincide with the two lines of figure 5.14. In the small  $\epsilon_L$  range we found the possibility of either the low or the high frequency wave being dominant in amplitude. The increasing amplitude of the second vertical mode affords the simplest explanation.

In an attempt to relate the pattern found (specifically the changes to lower frequency) in figure 5.14 to another system parameter, the observed frequency values were compared to  $Re_L$ . At the  $Re_L$  values of 56 and 125, which were obtained for onset of the types A and B Ekman layer instabilities (Tatro [1966]), no significant change of wave frequency was observed. This is expected, since the "local" Reynolds number (within the Ekman layer, under the probe) may not be the correct parameter to explain recorded inertial wave activity. Realizing that an unstable Ekman layer produces inertial waves having a positive radial component of group velocity (Green and Mollo-

FIGURE 5.14 - OBSERVED FREQUENCY vs.  $\epsilon_L$

Christensen [1970]), the existence of instabilities at some smaller radii would seem sufficient to produce motion at an outer position.

By incorporating the results of Chapter IV and section 5.1, the optimum region for initial instability generation is found at the junction of the sink side-wall layer and the interior. From Table 4 - 1, a typical value of this junction is taken to be  $r = 0.25$  ( $R = 6.1''$ ). By calculating the local Reynolds number ( $Re_J$ ) at this radius and plotting the wave frequencies against  $Re_J$ , figure 5.15 is obtained.

An analysis of figure 5.15 shows two transition Reynolds numbers. The first  $Re_J$  change took place at 52, when the low Reynolds number waves were superceded by inertial waves at  $r = 0.63$  and  $0.81$ . A similar transition at  $r = 0.73$  did not occur until  $Re_J \sim 92$ . Significantly, a second transition, amongst the inertial waves at  $r = 0.81$ , occurred at approximately the same value of 92. In view of the assumptions used in computing  $Re_J$ , it would seem unwise to directly relate these transitions to the Ekman layer instabilities.

In summary, the wide diversity and similarity of interior spectra, as reported previously, can be explained by comparison with the measured local Rossby number. The observed inertial wave frequencies will differ for varying tank aspect ratios. Furthermore, care must be taken to differentiate between the local low Reynolds wave and inertial waves.

## 5.5 Wave Spectra Within the Ekman Layer and Related Interior Motion

### 5.5.1 Reynolds Number Dependence of the Ekman Layer Spectra





The wave spectra observed in an Ekman layer have been found to depend critically on the local Reynolds number. By observing these wave motions on an oscilloscope, Tatro (1966) noticed a significant change in structure for certain flow configurations. He attributed the alteration to the Class A and B Ekman layer instabilities, occurring at  $Re_L = 56$  and  $125$ . The Rossby number dependence of the critical Reynolds number was judged to be linear by Tatro, as follows:

$$Re_L^A = 56.3 + 58.4 \epsilon_L^A \quad (\text{equation 5.6})$$

$$Re_L^B = 124.5 + 3.66 \epsilon_L^B \quad (\text{equation 5.7})$$

where the superscript indicated the instability class.

Caldwell and van Atta (1970) reexamined the onset criteria established by Tatro. They found a corresponding  $Re_L$  for the Class A wave onset, but were unable to detect the presence of any Class B waves (higher  $Re\#$ ).

The present work includes a wide range of local Reynolds number, at four radial positions. By comparing spectra at different heights within the Ekman layer, a significant change in the relative size of wave amplitude was observed.

In the lower Reynolds number range, figure 5.16 shows eight spectra taken at  $R = 14.70$  ( $r = .61$ ), for three different heights. For the two lowest fluxes (and  $z = .06\text{cm}$ ), the large spectral peaks correspond to the lowest Reynolds number "Stern" wave. As was apparent in the results of section 5.4, a lower frequency wave grew sufficiently in amplitude, for  $Re > 35$ , to become the dominant peak. The fre-

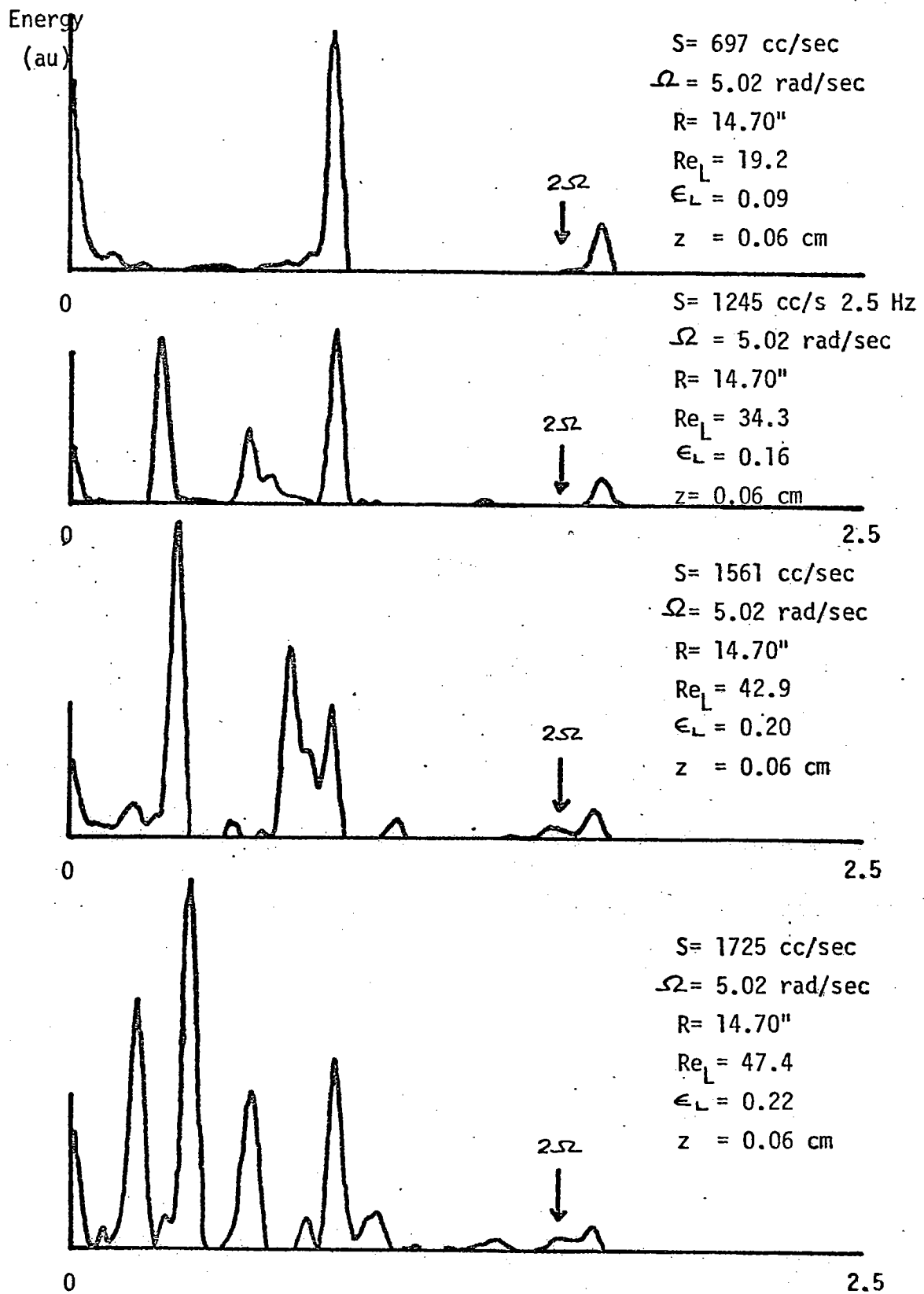


FIGURE 5.16A - LOW REYNOLDS NUMBER EKMAN LAYER SPECTRA.

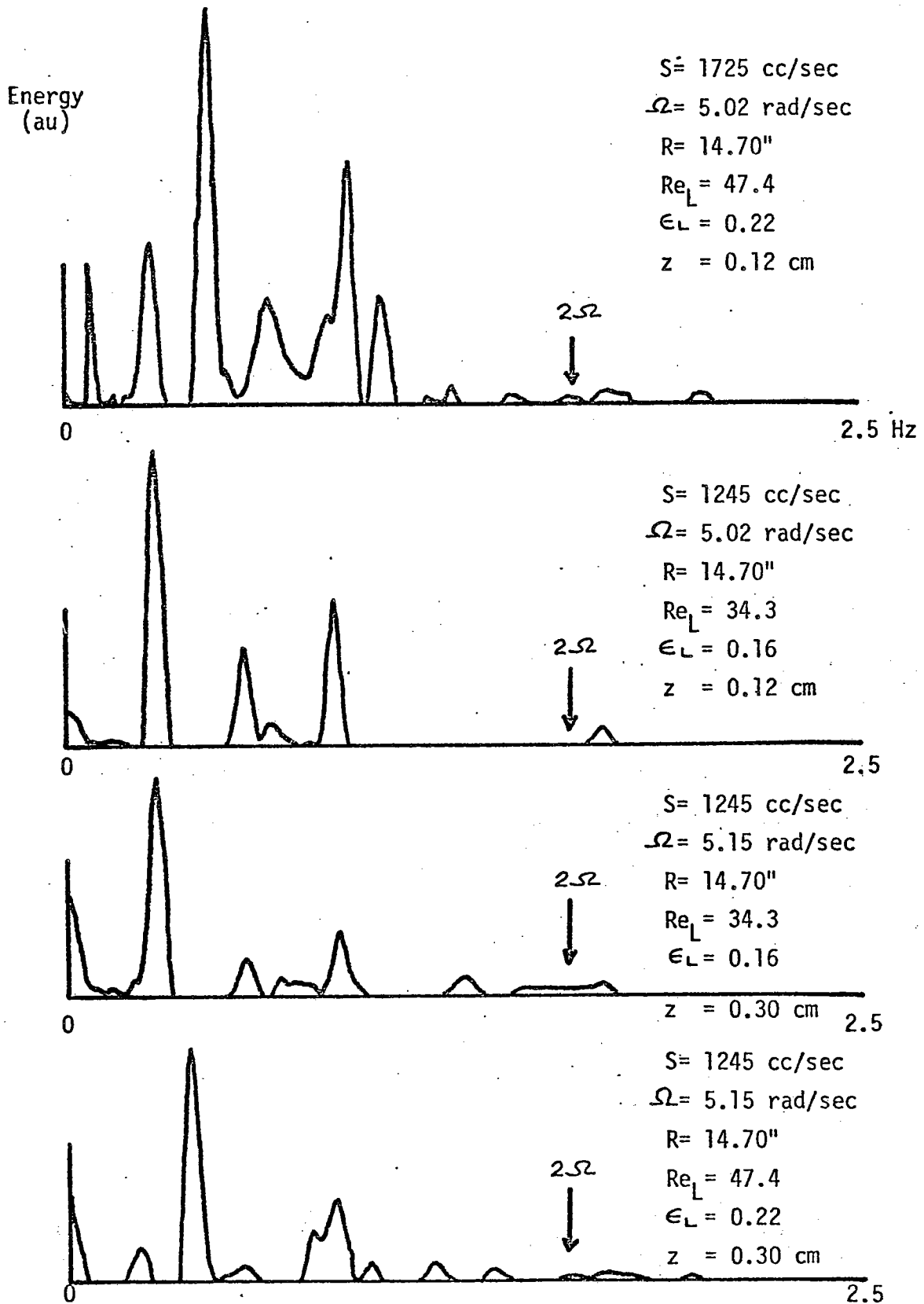


FIGURE 5.16B - LOW REYNOLDS NUMBER EKMAN LAYER SPECTRA.

quency of this wave increased with larger fluxes, as a result of Doppler shifting. The most significant feature apparent in the spectra is the continuous decrease of the "Stern" wave amplitude with distance from the lower wall. A comparison of the results for a flux of 1245 cc/sec., shows a rapid wave attenuation at  $Z = 0.30\text{cm}$ . This finding agrees with the results of section 5.3. From this finding, we assume that the interior vorticity structure inhibits the Stern wave appearance. The height dependence of the other waves in the spectra consists essentially of relative amplitude changes amongst the secondary peaks.

The above results include no  $Re_L$  values within the critical ranges, as defined by equations 5.6 and 5.7. This omission was intentional in order to exhibit the typical wave motion found within a supposedly "laminar" Ekman layer (see Greenspan [1968], figure 6.5a). For greater values of  $Re_L$ , the observed wave motion undergoes a rapid change, as seen in figures 5.17 and 5.18. However, this transition differs noticeably from the results of Tatro (1966). The contrasting wave traces can be explained by his lower signal amplification and incomplete removal of the mean velocity component.

The spectra of the above wave traces (fig. 5.17) are found in figure 5.19. The two large waves apparent in each spectrum changed their relative amplitudes, so that the lower frequency wave was dominant at the highest  $Re\#$ . This transition, occurring for  $Re_L > 62.7$ , is similar to the frequency shift mentioned in section 5.4. For the same Reynolds number range, wave energy with frequencies above  $2\Omega$  was observed. For all higher  $Re\#$  observations in the Ekman layer, energy was found above this inertial frequency limit. Although

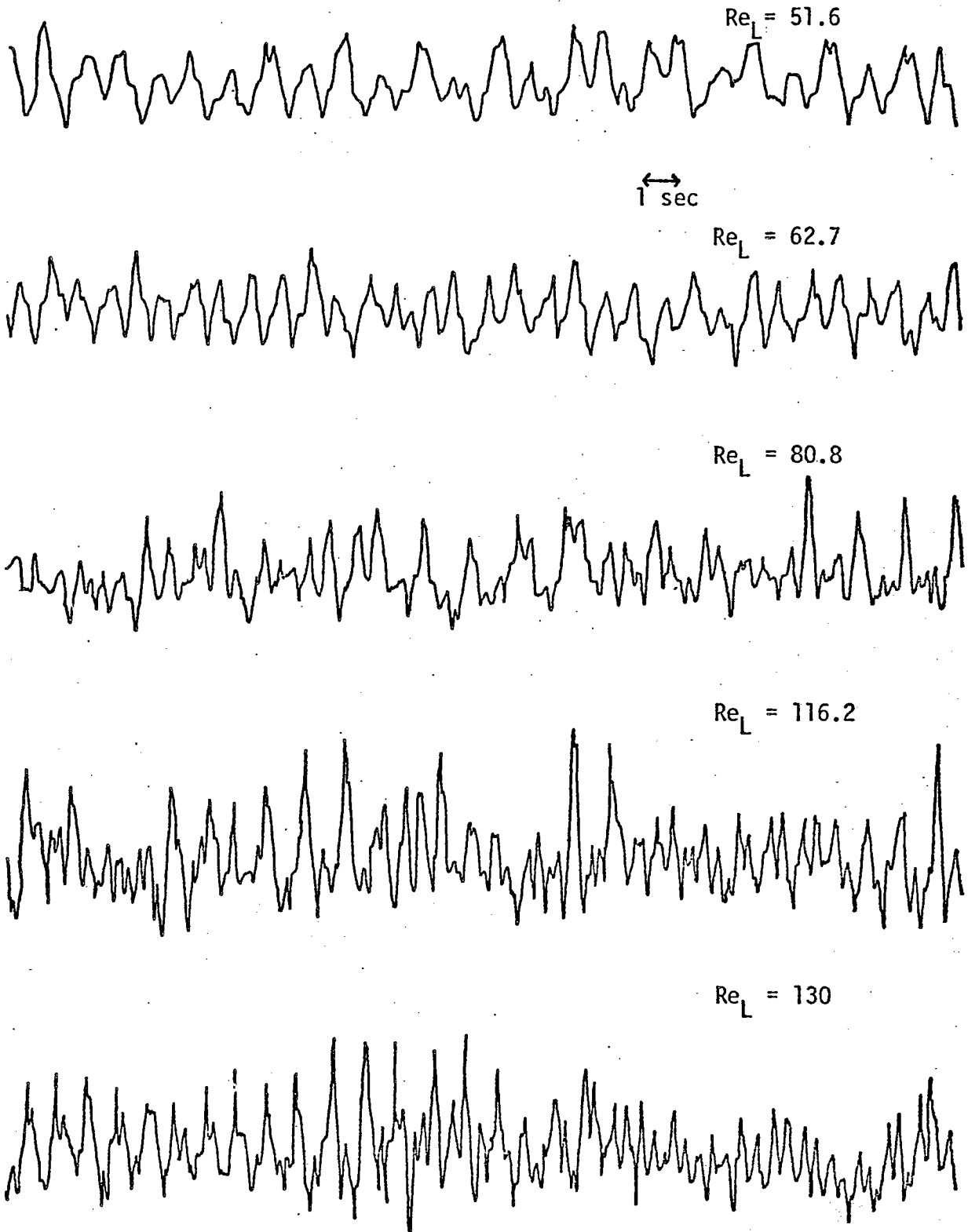


FIGURE 5.17 - HOT WIRE VOLTAGE OUTPUT

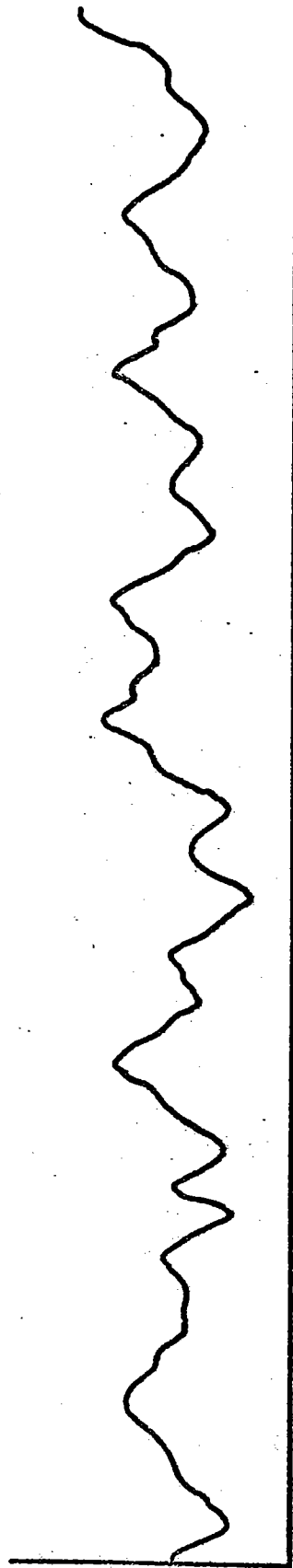
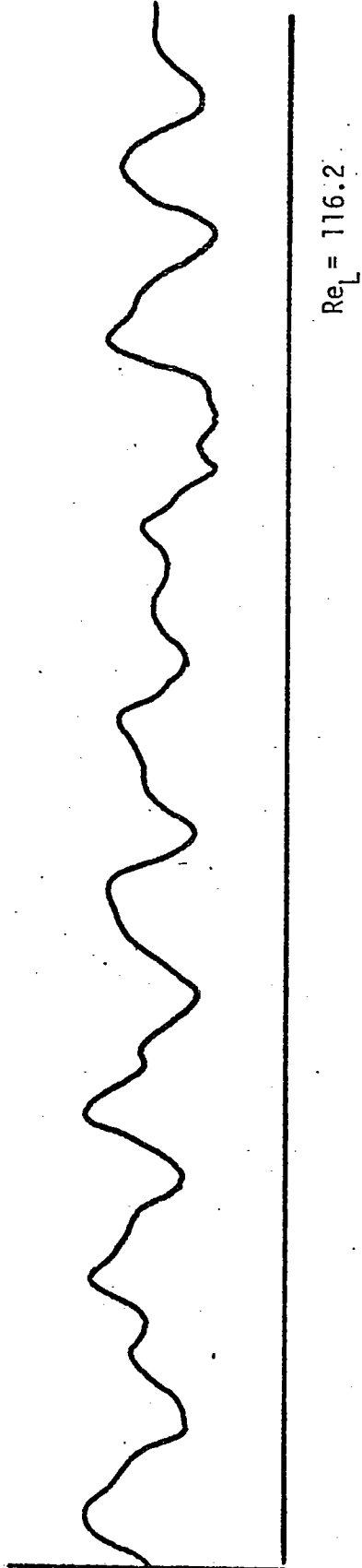
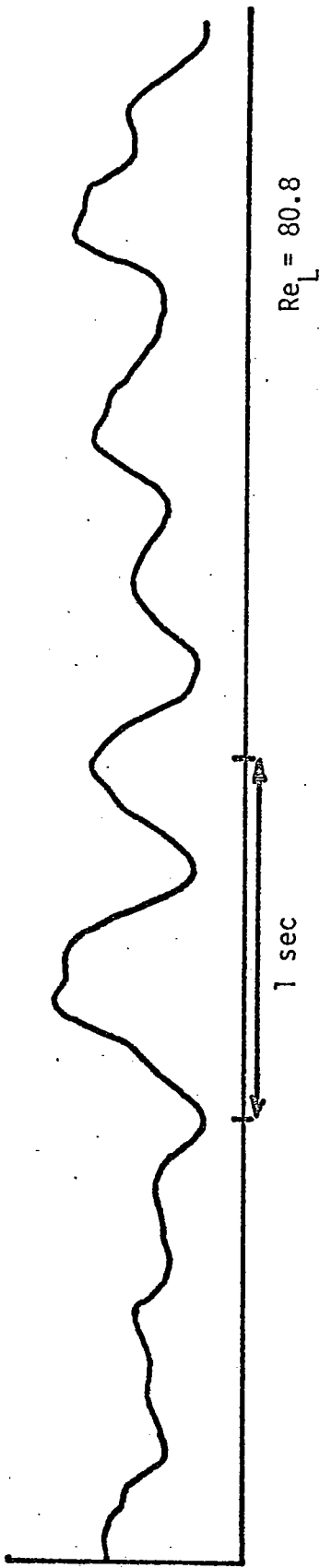


FIGURE 5.18 - EXPANDED TIME SCALE (HIGH  $Re$ )  $Re_L = 130$

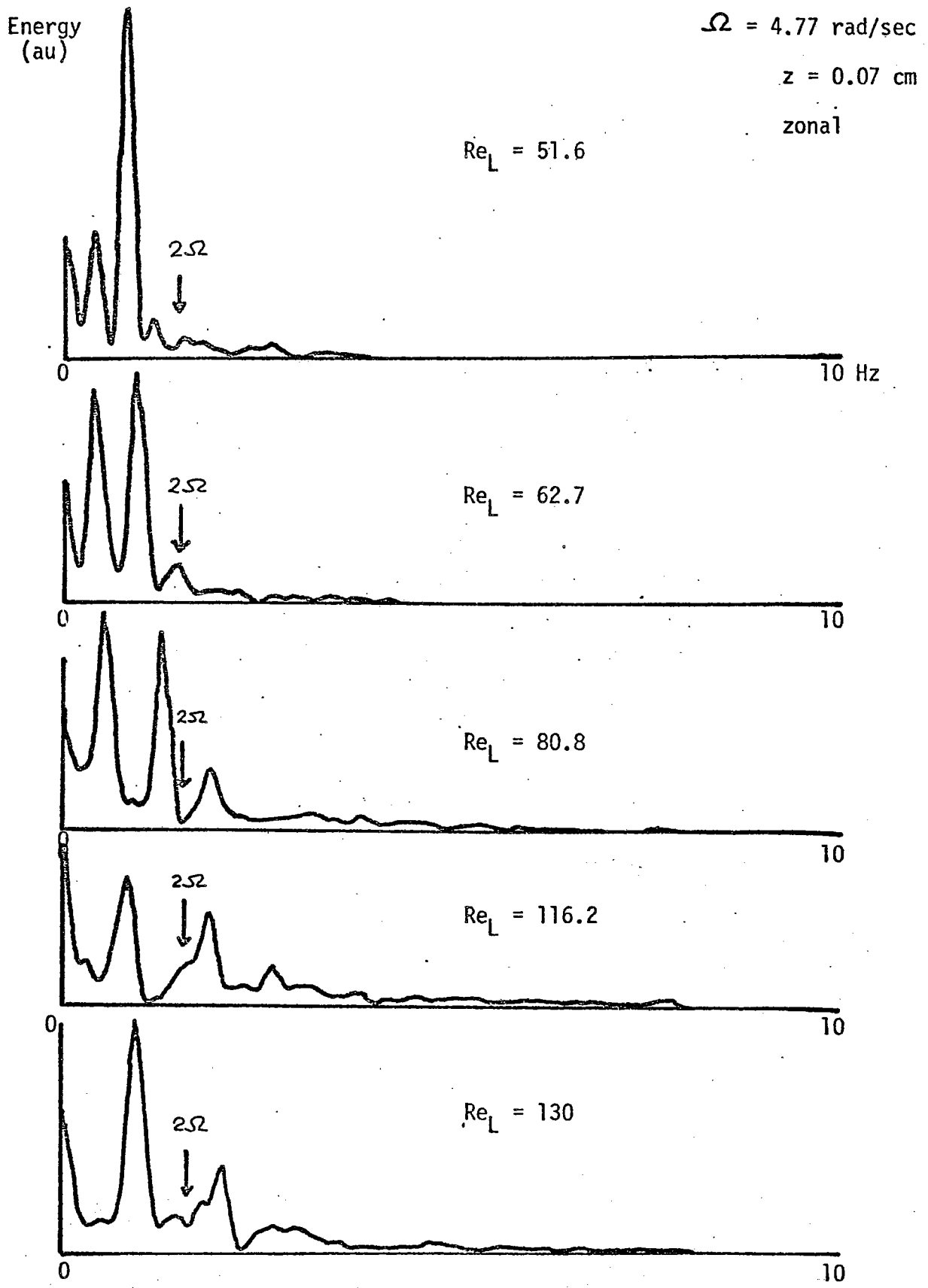


FIGURE 5.19 - EKMAN LAYER SPECTRA, R = 6.00"



the theoretically calculated  $Re_{\#}$  overestimates the actual value by approximately 40%, the motion observed at  $Re = 116.2$  is certainly in an actual Reynolds range greater than 56.

Additional results taken for larger  $Re$ , are depicted in figure 5.20. In contrast to all previous spectra, two of the records were obtained with the hot wire aligned to give maximal response for radial directed flows. The most interesting feature of this series is a large peak (slightly above  $4\Omega$  in frequency) observed with the radial probe at  $z = 0.21$ cm. The remaining spectra show only a minor amplitude wave at this frequency.

A further series of observations was taken deep within the sink side-wall boundary layer, at a radius of 4.50" ( $r = 0.185$ ). These spectra, shown in figures 5.21 and 5.22 include a theoretical  $Re_{\#}$  range of 80 to 360. Since the measured velocities and Ekman layer thicknesses are substantially smaller in the side wall layer, the ideal  $Re_{\#}$  overestimation is great (of order 60%). In the  $Re_L$  range of 80.8 to 233, the dominant peak is found to vary little from a frequency of  $4\Omega$  (independent of  $Re_L$  and  $\epsilon_L$ ). Above  $Re_L = 233$ , the frequencies change, but are still greater than  $2\Omega$ . These waves may correspond to those mentioned by Green and Mollo-Christensen, which had frequencies in the range of  $2\Omega$  to  $4\Omega$  (they show no spectral results). The sink side wall boundary layer was the only region in the tank to have no significant waves with frequencies below  $2\Omega$ .

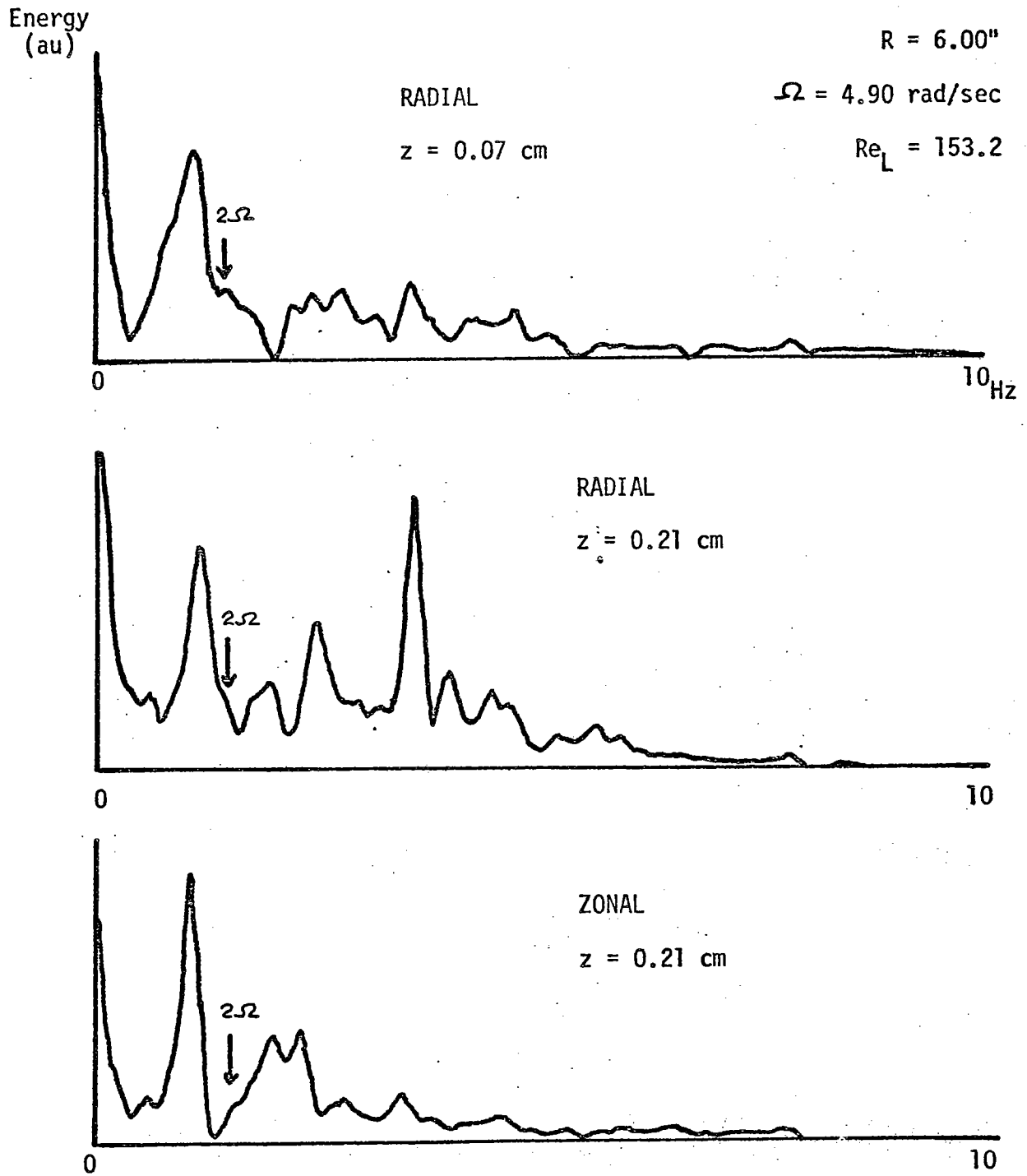
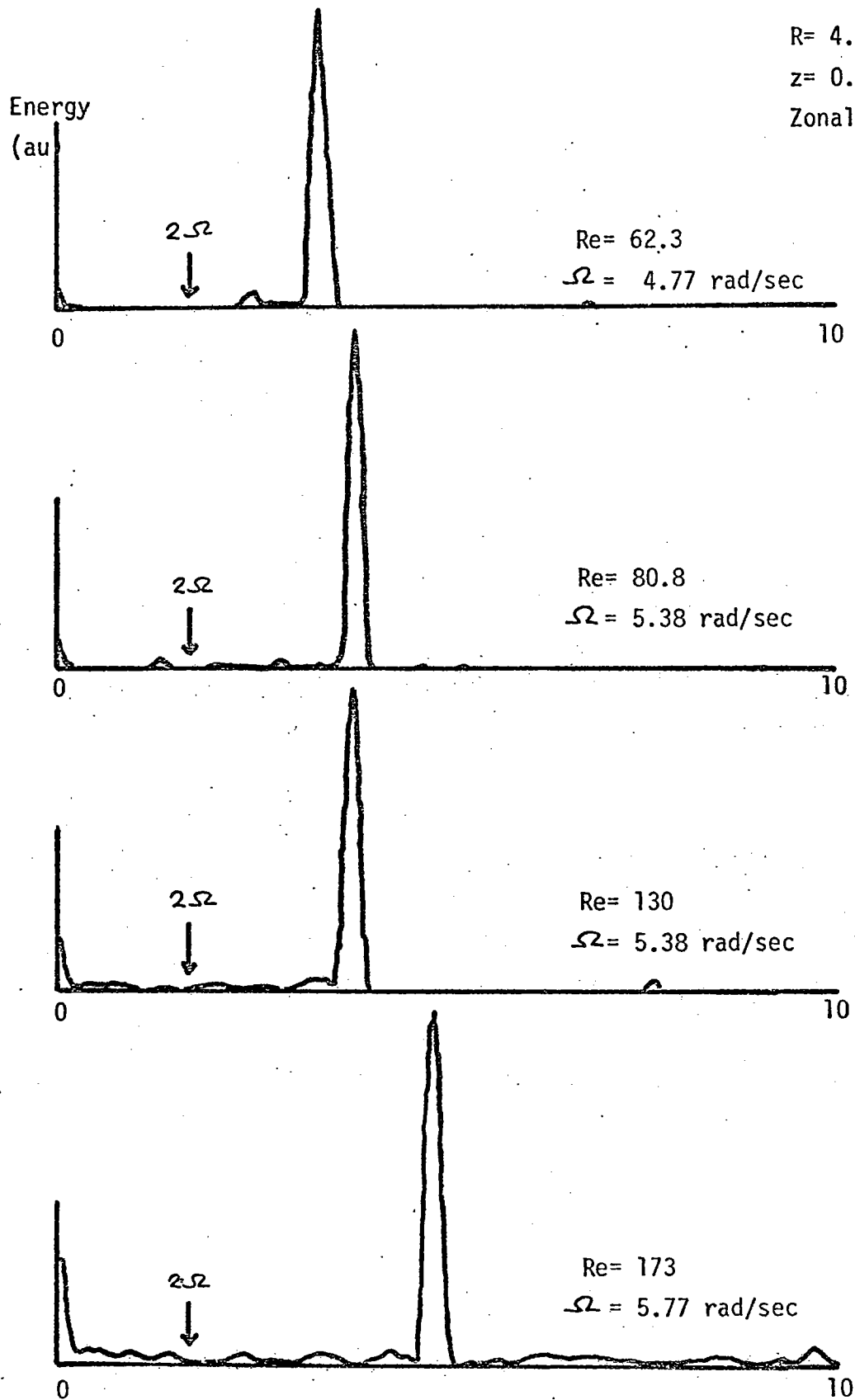
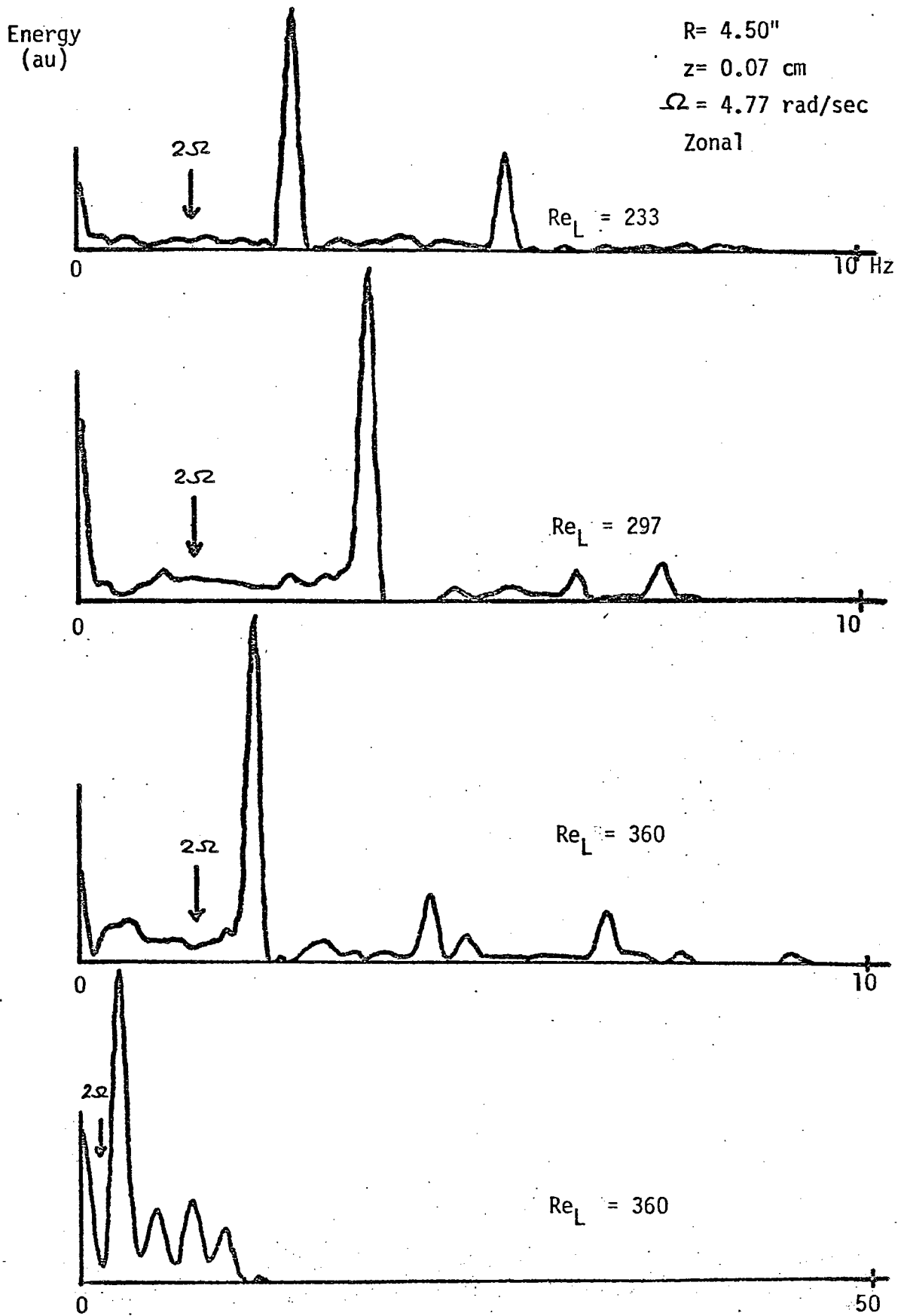


FIGURE 5.20

EKMAN LAYER SPECTRA,  $R = 6.00''$

FIGURE 5.21 - EKMAN LAYER SPECTRA:  $R = 4.50''$

FIGURE 5.22 - EKMAN LAYER SPECTRA,  $R = 4.50''$

We now turn to a short discussion of some previous Ekman layer wave studies in source-sink annuli. The work of Tatro (1966), and Caldwell and van Atta (1970) is found most relevant to the present results. Their primary aim was to delineate the onset criteria for the Class A and B Ekman layer instabilities. Figures 5.23 and 5.24 illustrate their results. Tatro separated his results into two classes of instabilities by linear fitting techniques. On comparing the actual points shown in his diagram to those of Caldwell and van Atta, a striking similarity is found for  $Re \leq 130$ . In contrast to Tatro, Caldwell and van Atta used a least squares fit of Faller and Kaylor's (1966) onset criteria. By extrapolating their curves to zero Rossby number, the critical Reynolds number was obtained. Both Tatro and Caldwell and van Atta find this number to be slightly above 56. Furthermore, Caldwell and van Atta claim that no class B waves were apparent in their results. As both figure 5.23 and 5.24 display a similar distribution of points about the  $Re_{crit} = 125$  line, it would seem their differences lie in definition and not in the dynamics.

In the present work, profiles # 1, 2, 3, 4, 7, 9, 11, 13, 14, 15 and 17 (of Table 4 - 2) are found to exhibit characteristics of the class A instability. The observed wave motion in these profiles was substantially larger (by a factor of 3) than in all others. A similar technique (wave amplitude) was used by Tatro and Caldwell and van Atta to estimate onset of the instability. The amplitude increase noted by Caldwell and van Atta is essentially the same as found presently. However, the most interesting comparison can be found among the local Reynolds numbers. From the theoretical

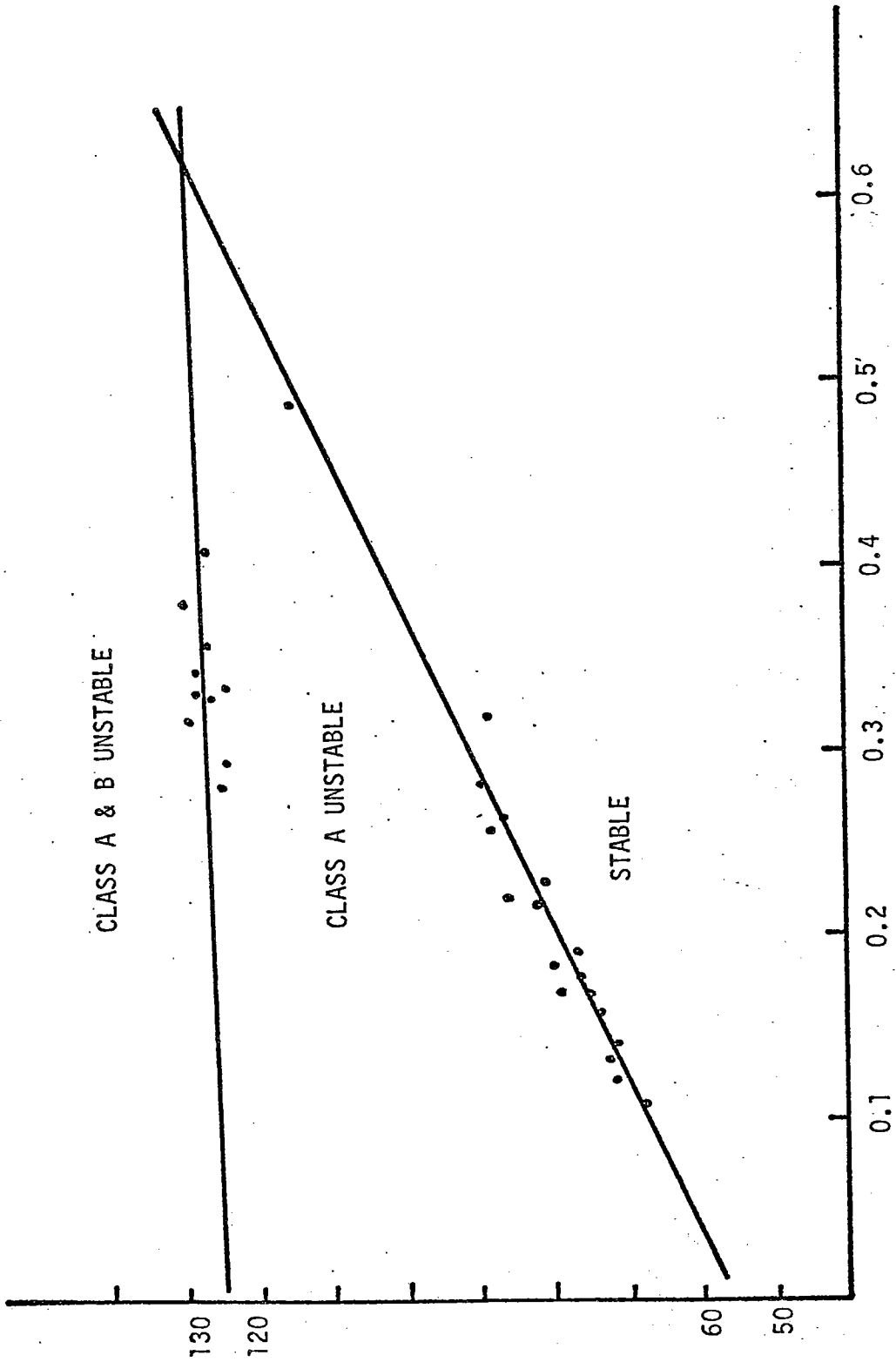


FIGURE 5.23 - CRITICAL REYNOLDS NUMBER VERSUS ROSSBY NUMBER FOR EKMAN LAYER INSTABILITIES (TATRO)

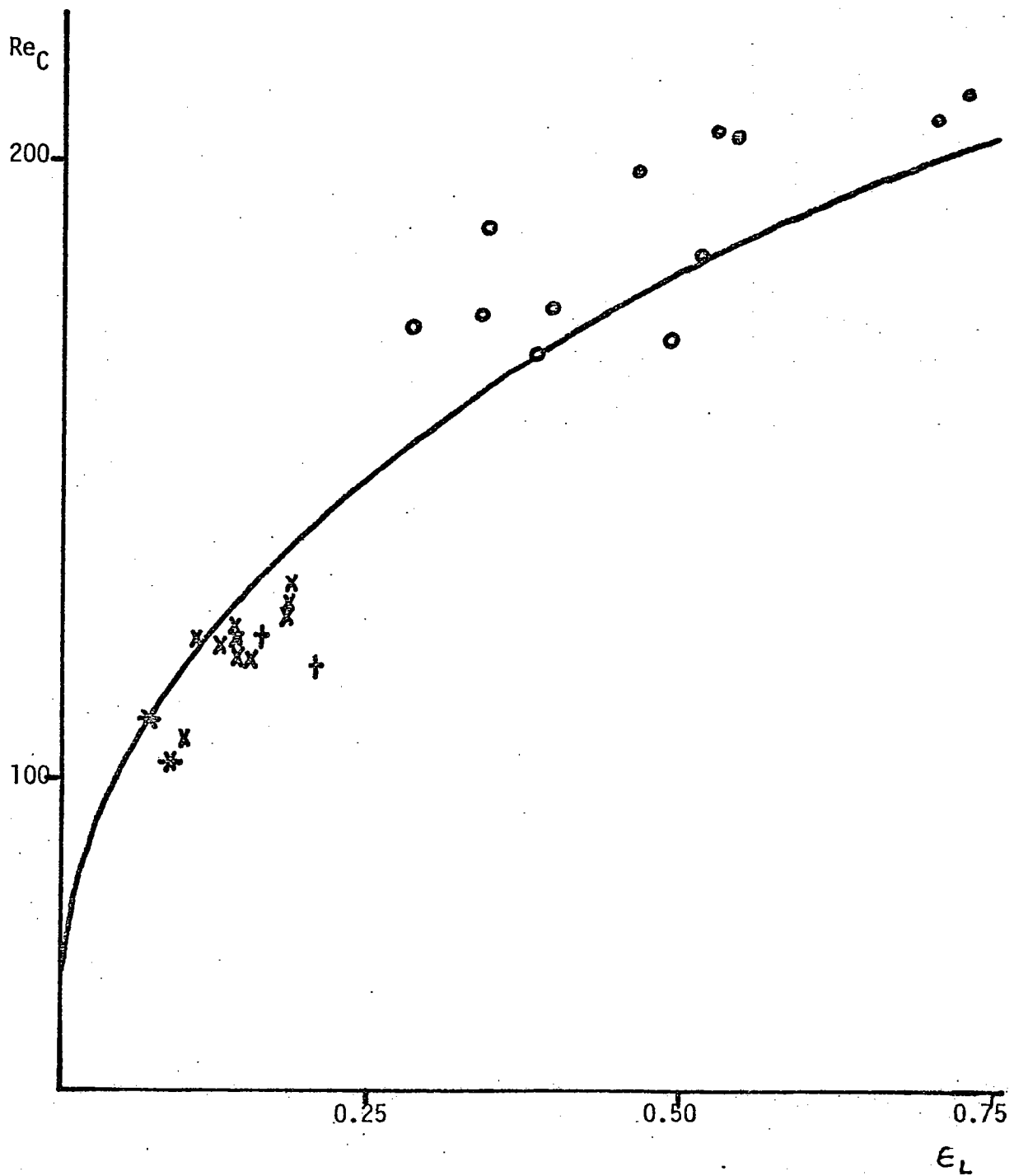


FIGURE 5.24

CRITICAL REYNOLDS NUMBER VERSUS ROSSBY NUMBER FOR EKMAN  
LAYER INSTABILITIES (CALDWELL & VAN ATTA)

values shown in Table 4-2, we find  $Re_{crit}$  is of order 50. The measured values were substantially lower (by one-half). Comparable  $Re_{crit}$  values in the work of Tatro (1966) and Green (1968) were much higher, resulting from their overestimation of the Ekman layer thickness.

The spectra of velocity fluctuations for Ekman layer profile #2 (see Table 4-2) was shown in figure 5.20. In this figure, at  $Z = 0.21\text{cm}$ , we assume the large amplitude high frequency peak corresponds to the class A instability. In a similar fashion, the spectral results shown in figure 5.21 are representative of Ekman profile #1.

Figure 5.25 shows a spectral representation of Ekman layer instability onset observed by Caldwell and van Atta. A comparison of these results with all of those obtained presently, reveals a marked difference. The dominant wave frequency in figure 5.25 is approximately  $10\Omega$ . In contrast, figures 5.20 and 5.21 exhibit dominant peak frequencies between 4 and  $5\Omega$ . Similarly, Caldwell and van Atta's wave frequency is essentially invariant with increasing flux. The only comparable wave dependency on flux is found in fig. 5.21 and 5.22.

Caldwell and van Atta also found an onset of turbulence in the Ekman layer for  $Re > 148$  (see figure 5.25). At this Reynolds number their observed spectrum became quite broad. To test this response in the present work, two spectra in a very high Reynolds range were obtained, as shown in figure 5.26. Allowing for a small overestimation in the  $Re$  value, the results were found to be definitely within Caldwell and van Atta's turbulent range. However, the present results displayed an orderly onset of turbulence, with all the harmonics and sub-harmonics having grown to equal amplitude. This "slow"



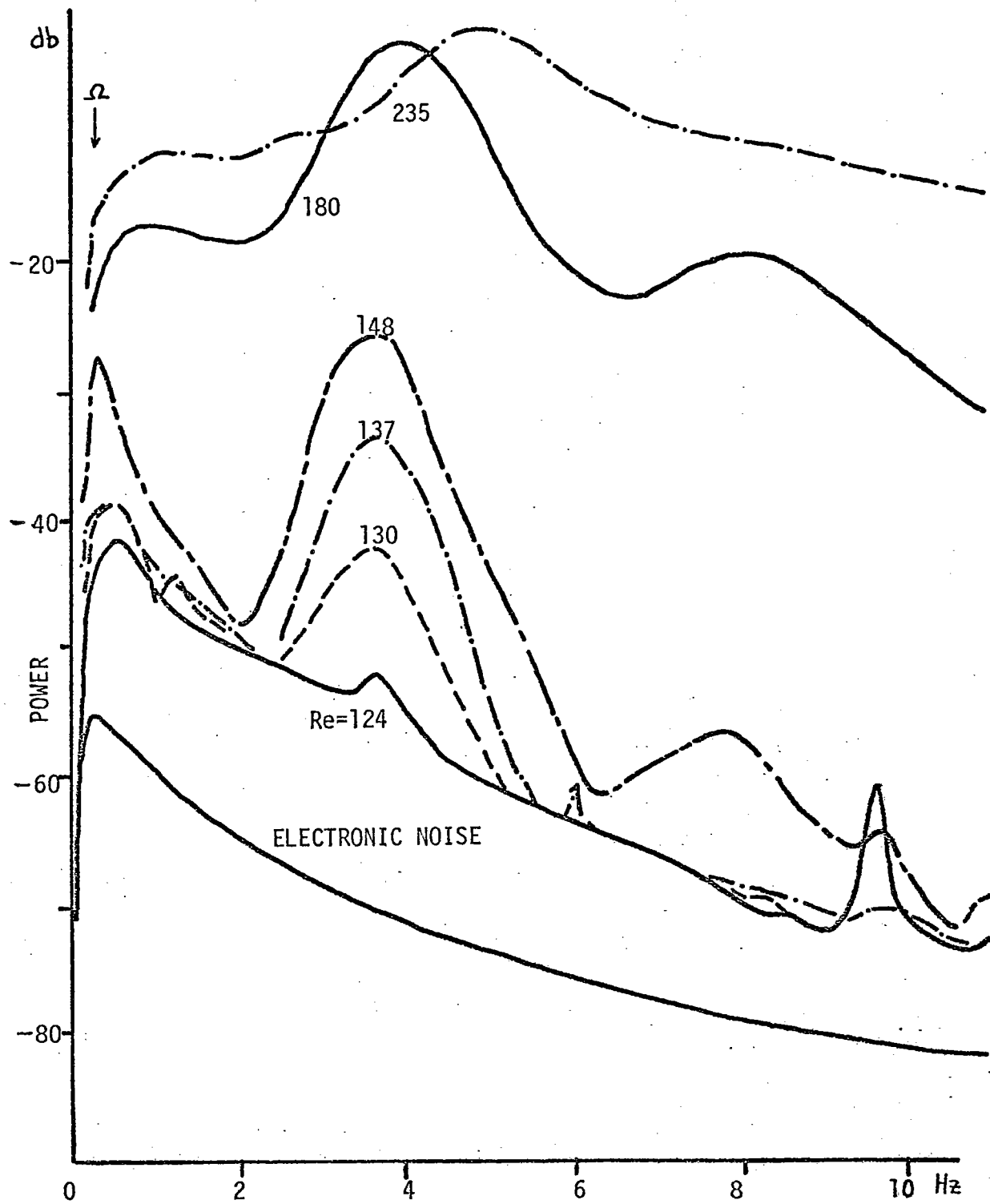


FIGURE 5.25 - EKMAN LAYER SPECTRA (CALDWELL AND VAN ATTA)

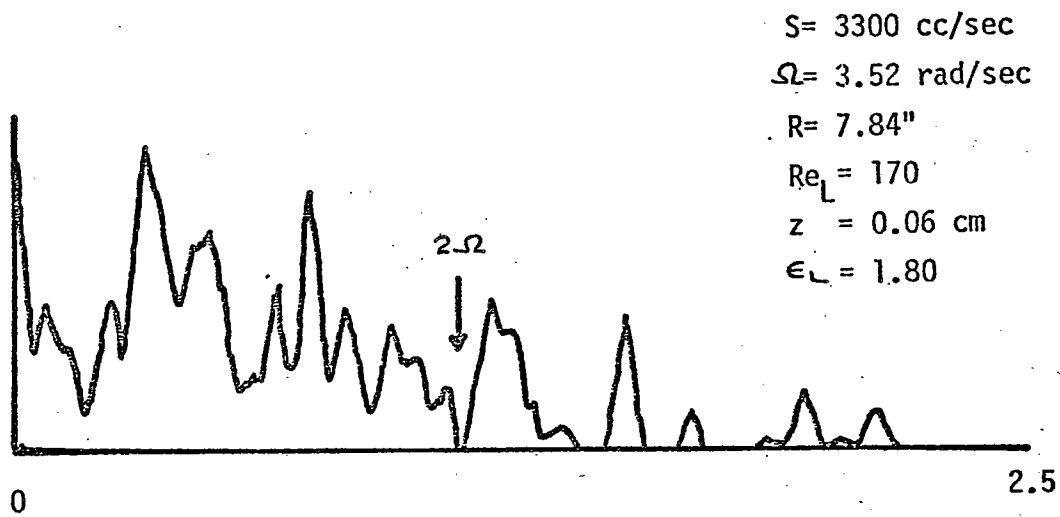
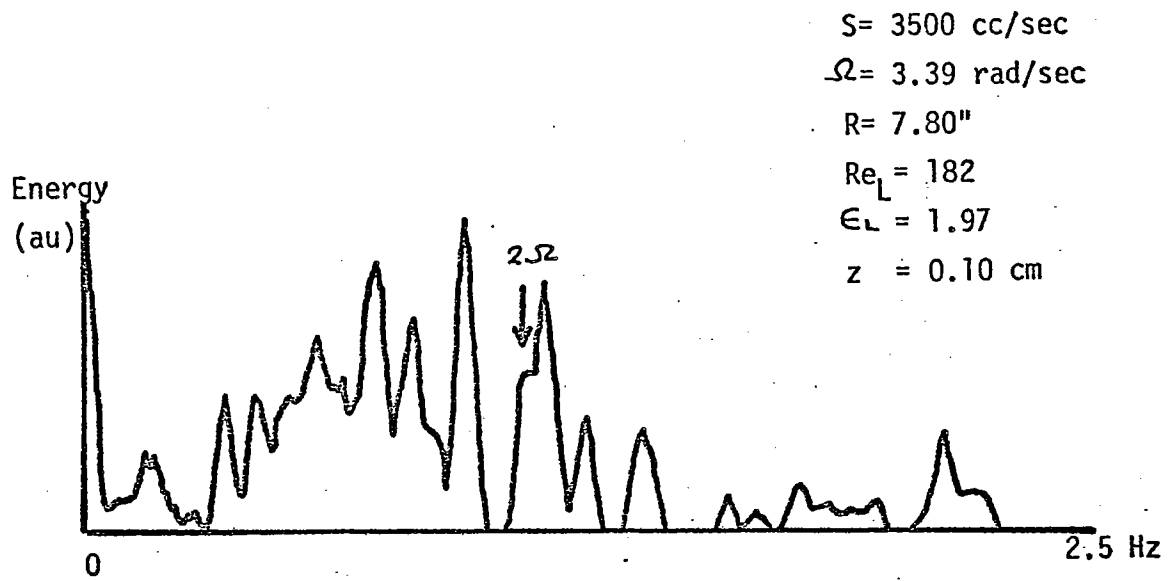


FIGURE 5.26 - EKMAN LAYER SPECTRA FOR HIGH REYNOLDS NUMBER FLOW

transition to turbulence may be related to developing non-linear modes (Ffowcs Williams, Rosenblat and Stuart, [1969]). A relevant example is found in the Taylor instability work of Coles (1965).

### 5.5.2 Comparison of Interior and Ekman Layer

#### Spectral Results.

According to Green and Mollo-Christensen (1970) similar spectra (the actual spectra is not presented) should be expected within an unstable Ekman layer as well as at an interior mid-tank position. It is not clear in their discussion whether oscillations of frequency greater than  $2\Omega$  were also predicted at the interior position. However, a comparison of figures 5.5 - 5.10 and 5.11 shows that at mid radial positions, similar inertial wave frequencies were observed in the interior and the adjacent Ekman layer. This frequency invariance with radius in the interior, was explained in section 5.4, as resulting from non constant circulation profiles. Also, the dominant inertial wave in the interior was readily perceived within the Ekman layer (see figures 5.7 and 5.11) at the same radius. As Green and Mollo-Christensen located their sensors at  $r = .37$  and  $.63$  (inner probe within Ekman layer), results obtained at these positions would be almost identical in dominant wave frequency (see section 5.4).

To further examine this dependency, another series, for larger  $Re\#$ , is shown in figure 5.27. The interior probe ( $r = 0.89$ ) was located within the outer Stewartson layer. The spectra exhibited few peaks of similar frequency. For  $Re_L = 64.2$ , only one peak was clearly transmitted to the outer radius. For the two higher  $Re\#$  comparisons,

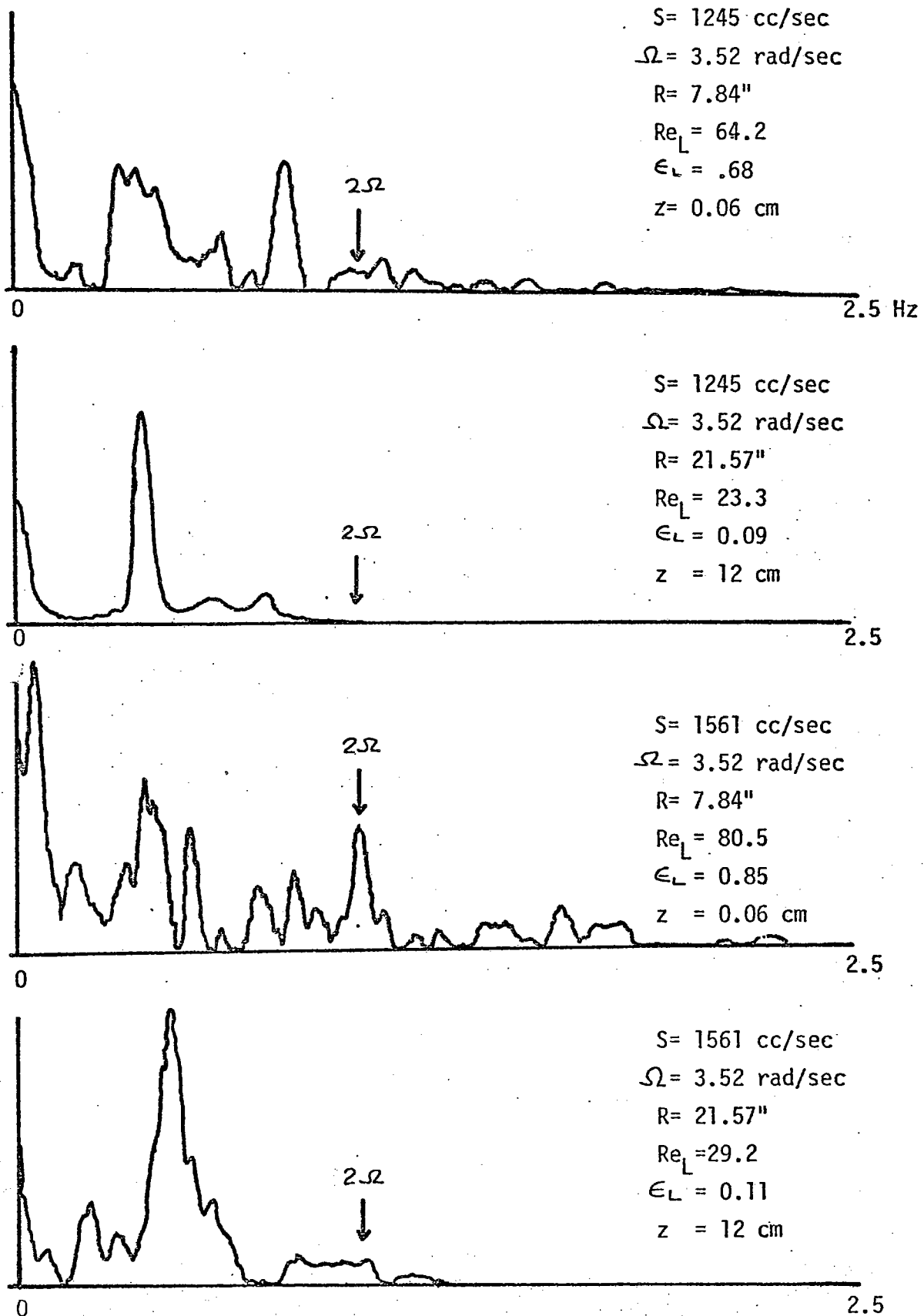


FIGURE 5.27A - INTERIOR AND EKMAN LAYER SPECTRAL COMPARISON

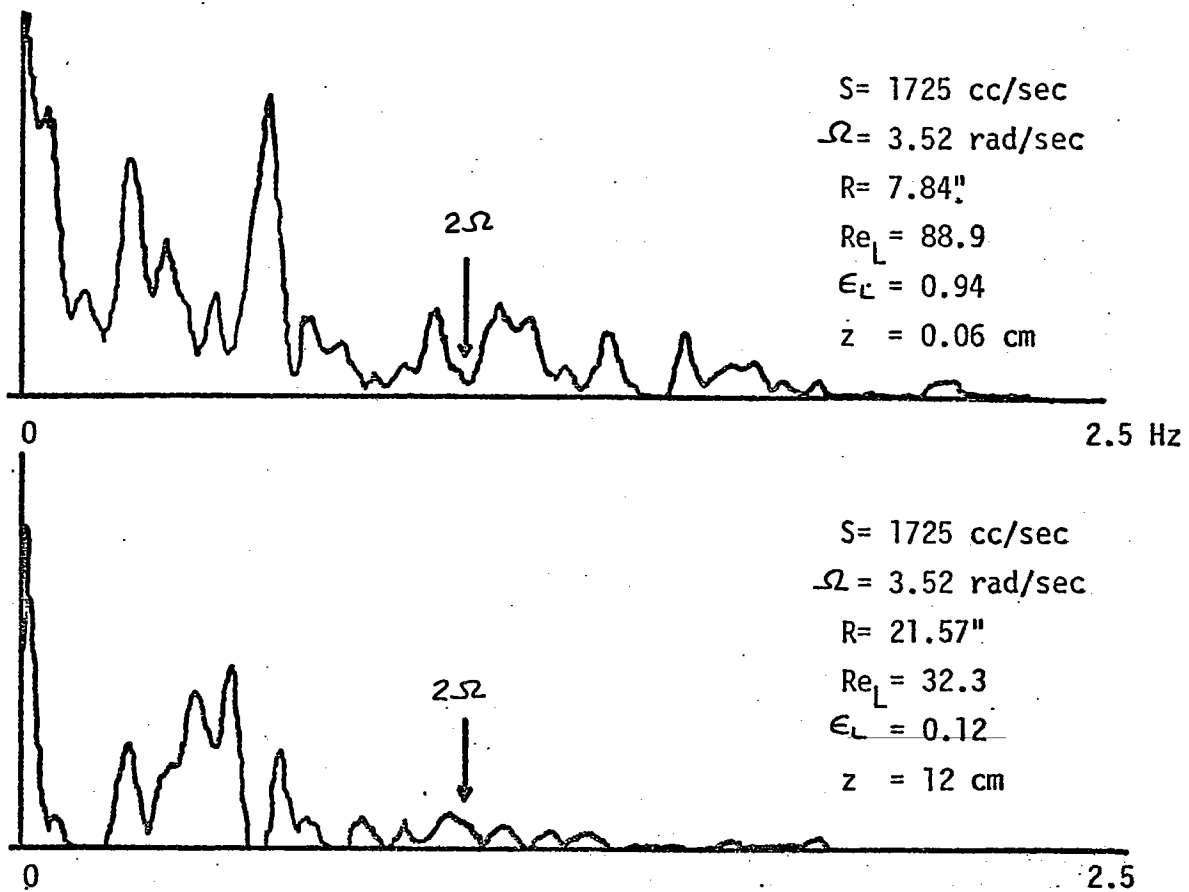


FIGURE 5.27B - INTERIOR AND EKMAN LAYER SPECTRAL COMPARISON

only two low frequency peaks were found at both locations. This is not surprising, since the radial distribution of similar frequencies in the first series was limited to  $r < 0.65$  (in general). It should be remarked, that the absolute amplitudes of the waves shown at  $R = 21.57''$  (Fig. 5.27) were much lower than their equivalents at  $R = 7.84''$ . Only a much larger amplification brings the two wave sets to comparable size. Two additional comparisons (not shown) for  $S = 697$  and  $903$  cc/sec., produced no wave activity at the outer location. This implies that the wave amplitude was less than .01% of the mean flow.

One can conclude from these comparisons, that the inertial waves generated by instabilities in the Ekman layer will be observed at most mid-tank locations ( $r = 0.35 - 0.65$ ). Furthermore, the inertial wave activity above the Ekman layer is usually observable in the spectra (some peaks) taken deep within the boundary layer. Green and Mollo-Christensen's results were within the radial range mentioned above. It appears that they are observing the inertial wave activity of the interior, which may have been generated at some other radius.

#### 5.6 Measurement of Azimuthal Wave Number by Cross Correlation

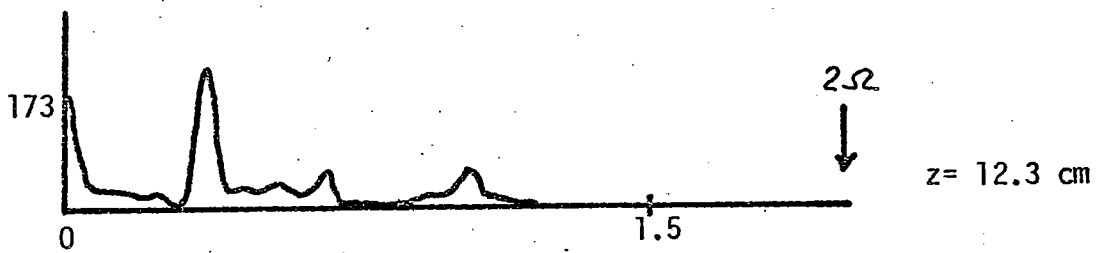
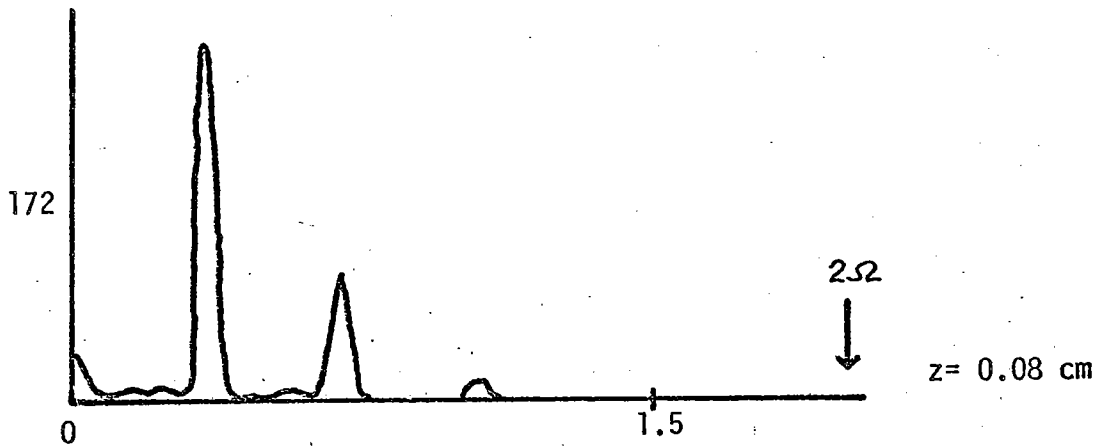
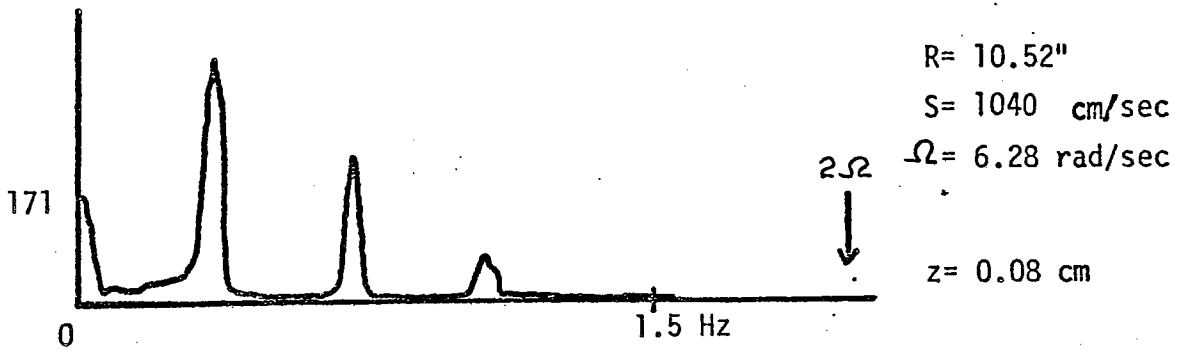
To obtain the azimuthal wave numbers for some of the non-axisymmetric waves, two probes were placed at the same radius, but separated zonally by a known angle. The cross correlation was measured as a function of the relative delay time between the signals recorded at the two positions. Thus the phase difference and therefore the azimuthal wave number could be determined. Additionally, the azimuthal wave structure in the Ekman layer and its relationship to the interior motions

were studied. For most interior correlations, the probes were  $60^\circ$  apart. When using only two probes, a definite separation of progressive and retrogressive modes was not possible in all cases.

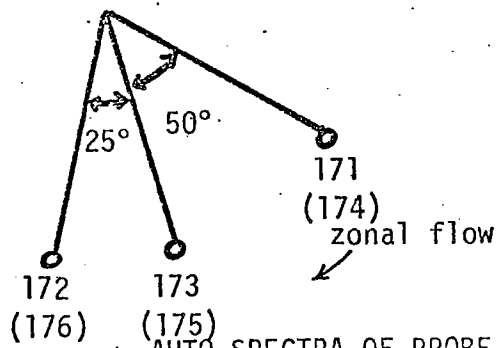
The auto-spectra results for one of the three cross correlation measurements is shown in Fig. 5.28. The probe configuration had two sensors at a similar height within the Ekman layer and an interior hot wire located between them. The parenthesized spectra numbers show placement for the second series. The third series (Fig. 5.29) used only two probes, one of which was in the Ekman layer, while the other was placed at varying heights in the interior. All other correlations (interior) were taken with the probes separated by  $60^\circ$ . Table 5-4 is a chart of cross correlation results with the pertinent experimental conditions listed. The wave class designation divides progressive and retrogressive, whenever possible. Two values are given when the choice is uncertain.

In the Ekman layer, the dominant wave was found to be axi-symmetric for both cases observed. The correlations between waves in the boundary layer and the interior at  $R = 13.80''$  showed a constant time lag for the three different heights. The "Stern" waves (cross correlations #14 and #15), were found to be axi-symmetric in the interior. The final correlations showed the non-axi-symmetric to be compatible in modal number. The dominant waves had a retrogressive direction with  $m = 3$ , whereas, the secondary peaks were either progressive  $m = 1$  or retrogressive  $m = 5$  azimuthal waves.

By using an extended probe in conjunction with a fixed hot wire, it was possible to estimate the radial wave length. Of the three runs taken, the wave length varied from 4 to 6 cm, but on the average was 5cm. The rotation rate was 4.52 rad/sec. and the fluxes varied from 1000 to 1500 cc/sec. ( $R = 12.0''$ ).

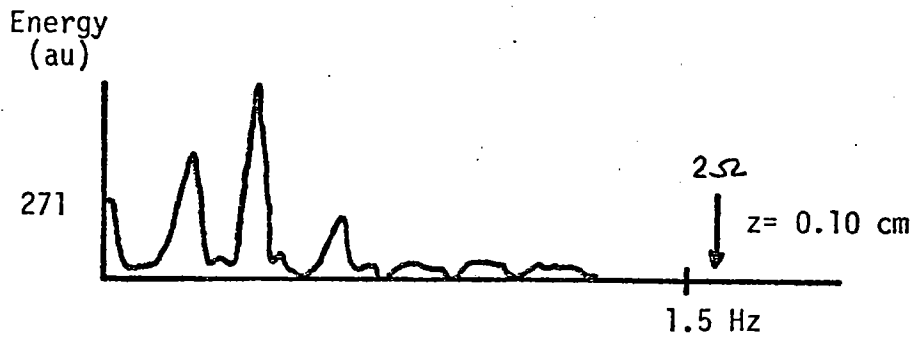


PROBE CONFIGURATION

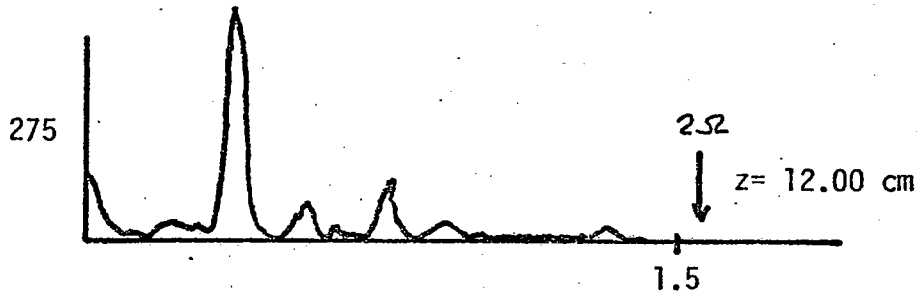
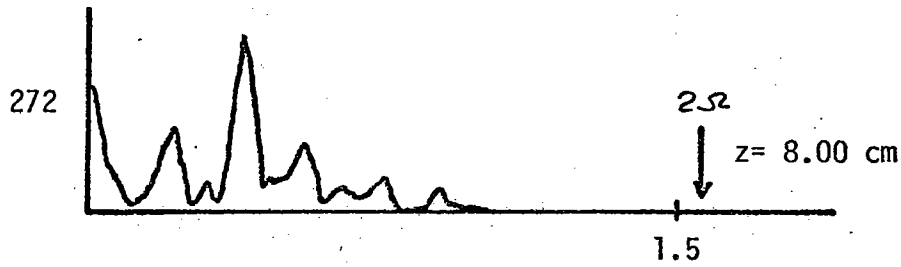
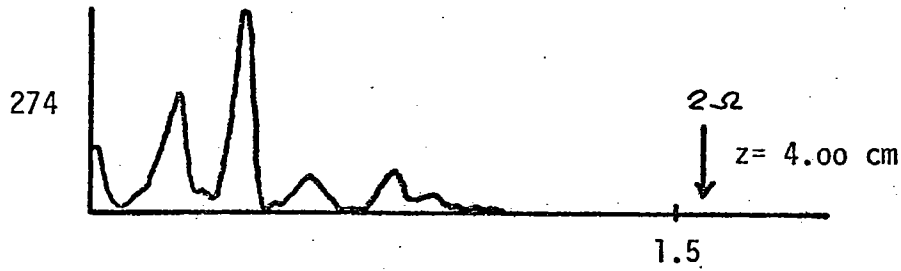


AUTO-SPECTRA OF PROBE OUTPUTS DURING  
 FIGURE 5.28 - CROSS CORRELATION MEASUREMENTS: EKMAN LAYER





$R = 13.80''$   
 $S = 1312 \text{ cc/sec}$   
 $\Omega = 5.02 \text{ rad/sec}$



PROBE CONFIGURATION

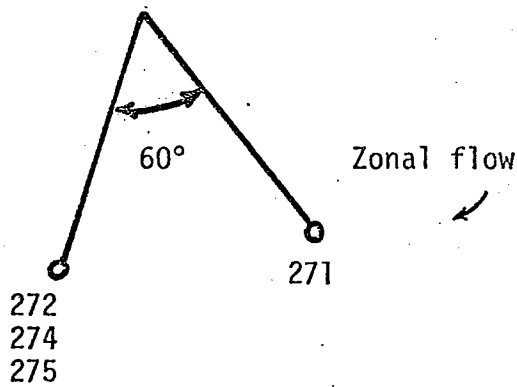


FIGURE 5.29  
 CROSS CORRELATION CONFIGURATION:  
 VERTICAL SEPARATION

TABLE 5 - 4

## CROSS-CORRELATION RESULTS &amp; AZIMUTHAL WAVE NUMBERS

#	FLUX(cc/sec)	ROT(r/s)	Radius(in.)	A		B		$\sigma$ (cps)	$\Delta\tau$ (sec)	m
				Spectra#	z(cm)	Spectra#	z(cm)			
1	1040	6.28	10.52	173	.08	171	.08	.34	0.0	0
2				172	.08	171	.08	.68	0.38	
3				173	12.3	171	.08	.34	0.47	
4				173	12.3	171	.08	.68	0.43	
5				173	12.3	172	.08	.34	0.53	
6	1561	6.41	10.52	174	.08	176	.08	.51	0.00	0
7				174	.08	175	12.3	.51	0.30	
8				175	12.3	176	.08	.51	0.31	
9	1314	5.02	13.80	271	.10	272	4.0	.21	1.30	
10				271	.10	272	4.0	.38	1.47	
11				271	.10	274	8.0	.21	1.36	
12				271	.10	274	8.0	.38	1.44	
13				271	.10	275	12.0	.38	1.52	
14	697	4.52	15.45	278	12.0	279	12.0	.74	0.00	0

TABLE 5 - 4  
(Continued)

15	903	4.52	15.45	280	12.0	281	12.0	.74	0.00	0
16	1245	4.52	15.45	286	12.0	287	12.0	.25	1.91	3(R)
17				286	12.0	287	12.0	.51	1.52	1(P), 5(R)
18	1451	6.85	15.45	290	12.0	291	12.0	.37	1.19	3(R)
19				290	12.0	291	12.0	.77	0.99	1(P), 5(R)
20	1715	4.52	15.45	284	12.0	285	12.0	.36	1.44	3(R)
21				284	12.0	285	12.0	.74	1.12	1(P), 5(R)

KEY:  $\Delta T$  : Time delay for maximum correlation (Signal A delayed with respect to B)

m : Azimuthal wave number

P : Progressive

R : Retrogressive

## CHAPTER VI

### Discussion

The results of the previous two chapters showed a remarkable interdependence between the steady and oscillatory motions. We found that the introduction of an Ekman layer instability at some radius in the annulus led to interior wave motions and in certain cases, to a change of the steady circulation profile. These alterations of the steady flow were found to influence the observed time dependent flow characteristics.

In this chapter, we will attempt to explain some of the more prominent features of the observed flows. In section 6.1, the changes in steady circulation are compared to previous results in differing geometries and to a non-linear modification of geostrophic flow, postulated by Greenspan.

The following section (6.2) discusses the alternate mechanisms available for producing interior disturbances with characteristics similar to those predicted by Stern. In section 6.3, the generation mechanism and the observed frequency of inertial oscillations is related both to the governing flow parameters, and the steady circulation field.

A summary of the boundary layers observed adjacent to both the horizontal and vertical walls in the annulus and their dependence on flow parameters is found in section 6.4.

In section 6.5, the various results are combined into an overall picture of the flows expected in a rotating source-sink annulus. The observed changes are found to have a critical dependence on flow parameters.

Finally, the relevance of the present work to geophysical phenomena and its possible extensions are discussed in sections 6.6 and 6.7.

### 6.1. Interior Circulation Profile

We found in Chapter IV, that for increasing values of flux, the circulation profile at mid-radial positions deviated greatly from theoretical prediction. Ideally, the interior circulation should be constant with radius. In contrast, the present circulation values showed a linear increase with radius, for higher system Rossby numbers (above 0.05). However, this feature was found only between the radial limits of  $r = 0.35$  to  $0.70$ .

Both Fultz (1959) and Malkus (1968) have observed the appearance of similar steady zonal flows, resulting from non-linear effects. Fultz's experiment used an interior disk to force inertial oscillations in a cylindrical tank. The interior motion was observed through the use of dye techniques. A much clearer view of this rectified geostrophic flow was obtained by Malkus in a precessing sphere, using aluminum flakes. In this case, the steady zonal current was observed to change direction several times over the radius of the sphere.

Greenspan (1968) had postulated that this feature may result from a non-linear interaction of a single inertial wave with itself to provide a steady zonal current and an oscillation at twice the basic frequency. However, in a later paper, Greenspan (1969) found that the principal non-linear interaction of inviscid inertial modes does not produce a resonant response in the steady geostrophic circulation. He concluded that only a combination of viscous and non-

linear effects within the boundary layer can provide a mechanism for development of the observed steady interior circulations.

The presently observed circulation changes could be explained by a similar dynamics. However, no definitive analytical work in this area has been reported. The principal cause of the generated steady currents which develop from oscillatory disturbances seems to be non-linear processes within the viscous boundary layers. In the present case, it implies that a linear treatment of the observed flows is valid for  $\epsilon_{\text{SYS}} < 0.05$ . In our annular configuration we do not expect the reversing flows observed by Malkus at "critical" latitudes in his sphere. The "critical" latitude in the annulus can be found only in the corner region.

## 6.2. Low Reynolds Number Waves at the Outer Radii.

At the outer radial positions (but not adjacent to the source wall) an axi-symmetric wave motion was observed at low Reynolds numbers. The frequency of these waves was found to be slightly greater than  $\Omega$  (actually  $1.04\Omega$ ) in all cases. Previous observational work in annular tanks has exhibited slowly moving axi-symmetric instabilities at lower Reynolds numbers. Furthermore, some of their observed wave features corresponded to predictions of Stern's (1960) Ekman layer instability study. Presently, waves with similar characteristics were detected (as discussed in section 5.3) and thought to be the same phenomena. A large attenuation of wave amplitude was noted for the higher Reynolds numbers.

Another possible explanation for the observed structure is found in the shear flow instability work of Busse (1968). He

distinguished between two mechanisms for instability. If the total angular velocity decreases with increasing radius, the Rayleigh (1920) stability criterion for axi-symmetric disturbances can be violated. Taylor vortices in the case of circular Couette flow are an example of this instability. A different kind of instability occurs as a wave propagating in the azimuthal direction and corresponds to the instability of parallel shear flow in a non-rotating system.

In an unpublished work (see Busse [1968]), Hide found that by differentially rotating (at  $\Omega(1 + 4\epsilon)$ ) a concentric disk in the upper wall of a rotating (at  $\Omega$ ) cylinder, non-axi-symmetric disturbances travelled along the resulting shear layer. For the typical Ekman numbers of the present work, Hide found the instability to occur for  $\epsilon > 0.02$ . Similar disturbances were not observed in the present experiments.

In the literature, the spin down experiments in a rotating cylinder are the most comparable to the present observations. During spin down, the inner fluid continues to move at the original rotation rate for a short time, thus replicating to some extent the radial profile seen in figures 4.2 - 4.11, at the outer radii. In his spin down experiments, Greenspan (1968) found axially symmetric Taylor vortices near the outer wall in the initial stages. Although some features of the low Reynolds number wave are similar to this instability, a direct analogy to Couette flow is not possible. The lack of a rigid inner cylinder and the characteristic frequency of the waves prohibits an exact comparison.

### 6.3. Inertial Oscillations

Inertial waves were frequently observed in the fluid interior. Their detection at a specific radial position was a function of the local Reynolds number, or more specifically the onset of Ekman layer instabilities at an inner radius. When  $Re_J$  ( $Re_L$  at  $R = 6.00''$ ; see section 5.4) was below 48, no interior waves were observed. However, for  $Re_J = 50$ , inertial oscillations were recorded at all interior radii less than  $12.5''$  ( $r = 0.51$ ). Furthermore, no significant wave motion was observed at  $R = 15.45''$  and  $21.00''$  until  $Re_J$  had surpassed 61 and 75, respectively. The first appearance of these waves corresponded to the initial instability of the Ekman layer. We observed (in section 5.5) that this instability occurred for  $Re_L \sim 50$ . As the maximum Reynolds number for the tank was found to be close in value to  $Re_J$ , this generation mechanism is further confirmed. The absence of inertial waves at outer positions can only be attributed to a loss of wave energy, this resulting from reflections at the horizontal walls.

In section 5.6 we found the typical radial wave length of the dominant inertial wave to be 5cm. Incorporating the other cross-correlation results with this value, we obtain the  $(r, \theta, z)$  wave numbers as  $(10, 3, 1)$  for the dominant wave and  $(10, 1, 2)$  for the secondary peak. Calculating the non-dimensional frequency of such inertial waves gives values of 0.09 and 0.18. Significantly, these frequencies correspond to the extrapolated (non-advective) wave frequencies in figure 5.14. Although other modes exist (with much lower amplitudes), we find the two dominant waves to be standing inertial oscillations



with the above wave numbers. The axial wave numbers were inferred from the observed frequencies, as no actual measurements were taken.

Although the wave length of the Class A Ekman layer instabilities was not measured presently, Tatro (1966) has observed it to be  $28\delta$ . Since  $\delta = 0.18\text{cm}$  for the results of section 5.4, a typical wavelength is estimated to be 5.2cm. This length corresponds to radial wavelength of the generated inertial wave. Also, we might expect the azimuthal wave number of the generated inertial oscillations to be small since the Class A waves are found by Tatro to be almost axi-symmetric (i.e., low azimuthal wave number).

The observed inertial oscillations showed frequency shifts at different radii, this resulting from Doppler effects. Previous experimenters have attributed these shifts to the existence of other waves. The results of figure 5.14 discount this hypothesis.

#### 6.4. Boundary Layers

In a theoretical work, Lewellen (1965) found that it was not possible to match an Ekman layer to an interior circulation that decreased with increasing radius. He also found that a constant circulation was weakest radial dependence possible for matching. The presently observed Ekman layers show no consistent change in thickness for varying interior flow conditions. However, the vertical dependence of the boundary layer wave characteristics was found to depend on the radially distributed circulation.

In general, the observed Ekman layer( $\delta$ ) are found to be 80 - 85% of the theoretical scale height. Only in the high Reynolds number range is a significant decrease of boundary layer thickness noted.

Much of the previous work in Ekman layer instabilities has erroneously used thicknesses of two to three times the correct value.

The Ekman layer non-linear modification theories have underlying inconsistencies in their analysis and thus are not subject to comparison.

The existence of sidewall boundary layers at the source and sink confirms theoretical prediction. The characteristic width of these layers was found to be larger than that obtained from linear theory. The boundary layer adjacent to the source is approximately one and a half to two times as wide as that adjacent to the sink. The slight non-linear modification observed on the inner wall boundary layer is not explained by previous non-linear theories. The non-dimensional inner boundary layer width is approximately 0.13, whereas the outer layer is 0.18.

#### 6.5 Flows in a Rotating Source Sink Annulus

The flows observed in a rotating source sink annulus were found to depend critically on the local Reynolds and Rossby numbers. For  $\epsilon_{\text{sys}}$  less than .05 and  $Re_j$  less than 40, a constant interior circulation profile was obtained. The Ekman layer thicknesses were 85% of the theoretically predicted value. The width of the sidewall boundary layer adjacent to the sink conformed to linear prediction, whereas the source boundary was 1 1/2 times this value. The only detectable wave motion was the low Reynolds number wave, which was found to extend through the outer half of the annulus.

A marked change became apparent at  $Re_j = 50$ . At this value, a Class A Ekman instability was observed over a narrow radial range. The introduction of this instability into the flow generated inertial wave motion in the interior with a similar wavelength to that of the Class A waves. These inertial waves were not apparent at the outer radii. However, a small change in the radial dependence of zonal velocity was observed. Through a non-linear interaction of the inertial waves with the Ekman layer, a weak shear layer was produced in the interior. This was evidenced by a linear increase in circulation with radius (over a narrow range). The low Reynolds number waves were found to decrease rapidly in amplitude within the range of this circulation change. The Ekman layer thicknesses were unaltered, except for the area of the instability, in which a decrease was noted. The sidewall boundary layers increased slightly in width for these higher Rossby number flows. The induced Ekman layer divergence produced an immeasurable vertical velocity (1% of zonal velocity).

These changes became more pronounced with increasing Reynolds and Rossby number. For  $Re_j > 75$ , the inertial wave motion was found in all interior areas of the annulus. Although large changes were apparent in the observed frequency of these waves for the different flow rates, the values could be interpreted by incorporation of Doppler effects. In the interior, only two dominant inertial waves were apparent in most cases. On increasing  $Re_j$  past 89, the low Reynolds number was found to exist only as a secondary peak. For  $Re_j > 100$ , the wave had an insignificant amplitude. In this  $Re_j$  range, the shape of the circulation profile did not change with  $Re_j$ .

By greatly increasing the local Reynolds number, an orderly (slow) onset of turbulence was generated within the Ekman layers. However, in the same  $Re_j$  range, a similar response was not detected within the Ekman layer of the sink sidewall boundary layer. At this position, only a single wave similar in frequency to the Class A instability, was observed.

At present, the above description represents the most complete analysis of flow characteristics in a rotating source sink annulus, for linear, non-linear and turbulent regimes. Previous work has failed to simultaneously observe the sidewall and horizontal boundary layers, and their influence on the steady and transient motions of the interior. Through the present work, the relation of Ekman layer instabilities to observed changes in circulation and the internally generated wave structure is elucidated. However, the actual forcing of the inertial waves ( $\sigma < 2\Omega$ ) by the instabilities ( $\sigma > 2\Omega$ ) is not readily solvable. The onset of Class A instability occurs at  $Re_j \sim 50$ . Previous workers have incorporated erroneous Ekman layer thicknesses in calculating the actual value of the critical Reynolds number.

#### 6.6. Geophysical Relevance

The nature of the present experiments lends itself to applications in the area of strong vortices in nature. The actual structure of the Ekman layer and its influence on the interior flows is also a relevant consideration. The laboratory-produced Ekman layer instabilities excite inertial waves which in turn are found to interact in non-linear fashion with another Ekman layer. This produced a

modification of the interior flow. These alterations of the mean flow may be of importance in both atmospheric and oceanic motions. Recently, Brown (1970) has interpreted secondary flows in the planetary Ekman layer as the cause of some observed atmospheric phenomena (such as cloud patterns).

The instabilities noted at the outer radius, as well as the weak internal shear layers, may find application in the study of the geomagnetic field created by motions in the earth's core (Malkus[1967]).

The influence of stratification and higher frequency motions appears to lessen the direct applicability of the steady and transient Ekman layer observations to related oceanic work. However, Gonella (1968) has observed a boundary layer that closely resembles the predictions of linear Ekman theory, under certain climatic conditions.

#### 6.7. Future Work

Although time consuming, detailed observations of the actual interior circulation and the radial distribution of Ekman layer thickness for each spectral result, would be beneficial. This would give an improved delineation of the abrupt changes occurring in the observed motions. Also, further work is needed in the area of instability wave structure. The confusion arising from the work of Tatro and Caldwell and van Atta in classifying the two types shows this necessity. This would also allow a clearer view of the actual generation mechanism of inertial waves.

A further analysis of the low Reynolds number at high system Rossby number could be accomplished by filling the inner radial region of the tank with foam, so as to give a tank aspect ratio of 1. With this configuration, inertial waves would be unable to influence these observations over a wide range of  $\epsilon_{\text{sys}}$ .

The onset of turbulence in the Ekman layer and the transient interior response to changes of flux are topics of much interest and require extensive work.

## APPENDIX I

## Experimental Set-up and Methods

## AI.1 The Rotating Source-Sink Annulus

The basic apparatus used in these experiments is a rotating axis-symmetric annulus with a sink located peripherally on the inner radius. Similarly, a source is placed on the periphery of the outer radius. The source and sink are composed of porous reticulated poly-urethane foam, the latter placed firmly over a porous metal spool and the former cemented to the upper and lower walls at the outer most radius. The upper and lower horizontal surfaces are parallel polished aluminum disks, each of thickness one-half inch. The central spool is attached to a concentric hollow pipe (and the rotation axis), which in turn supports the apparatus and provides an exhaust for the induced flow. A radial pressure gradient is imposed by a vacuum system connected to the termination of the hollow pipe. A schematic plan of the annulus and associated hardware was given in figure 3.1.

The annulus shown is designed to rotate about the vertical line passing through its axis. Careful machining assured that the annulus was axis-symmetric about its rotation axis, thus eliminating extraneous flow disturbances (Thompson, [1968]). The horizontal walls were maintained parallel by four adjustable connecting spacers located at the outer radius.

## AI.2 The Rotation Control

The tank was rotated by means of a DC motor (1/2 hp) connected

to a speed control unit (Minarik SH-63). Rotation rate could be maintained at a constant value for periods up to two hours, with changes less than that resolvable by the counter circuit (0.5%). For comparative purposes, the rotation rate could be reproduced at a later date by use of the fine torque control of the speed unit. As seen underneath the tank in figure 3.1, the rotation rate was measured by a photoelectric counter, tripped by a light source penetrating any one of the fifty evenly-spaced small holes on an aluminum collar. The results were displayed on a pre-set counter.

### AI.3 The Flux Control

The technique of obtaining a substantial range in radial pressure gradients was similar to that used by Green (1968). This subsystem consisted of a calibrated flux meter, baffle, perforated cylindrical sleeve and an axial fan connected sequentially from the hollow exhaust pipe of the tank. The calibrated flux meter consists of a hot wire probe mounted in the wake of a small cylindrical rod extending across the pipe's diameter. The flow passes through a number of rectifying screen before impinging on the rod. Above a certain Reynolds number, a Karman vortex street is formed behind the cylinder, the shedding frequency of which is measureable by the hot wire. Using an American Meter Corporation standard bell-type proof meter (accurate to 0.5%) as an absolute volume flux calibrator, Green (personal communication) found the flux was linearly related ( $\pm 1.5\%$ ) to the shedding frequency. The relation,  $S = 218 + 13.7\eta$ , gave the volume flux  $S$  in cc/sec., when  $\eta$  (shedding frequency) was measured in hertz (for rod diameter 0.182cm). Changes in flux were obtained by altering



the vacuum suction mechanically or by changing the covered area of the perforated sleeve at a constant suction, the latter resulting in a change of the differential pressure provided by the fan. A discussion of the advantages and disadvantages of such a system is found in Green (1968).

#### AI.4 Probe Configurations

For all the velocity measurements, hot wire anemometer probes were used. A great variety of probe configurations were employed, as seen in figure AI.1. The simple (single) hot wires are similar to those used by many previous experimenters. The boundary layer probe, is of similar nature but has a small leg which protects the wire from damage by collision with the boundary and gives an exact vertical reference height. The vertical distance between the hot wire and the bottom of the leg was measured optically with a toolmaker's comparator (accurate to the nearest one-thousandth of an inch). The extended arm probe was built to allow measurements of interior velocity for a wide range of radius under identical operating conditions. The plug-in probes were similar hot wires to those above, but were mounted in plexiglass inserts, which could be positioned in the bottom of the tank. The probe positions noted in figure 3.1 readily shows the possible positions of the different designs. The mobility of the top-mounted probes is seen in figure AI.2, as well as their relative position to those mounted on the bottom plate.

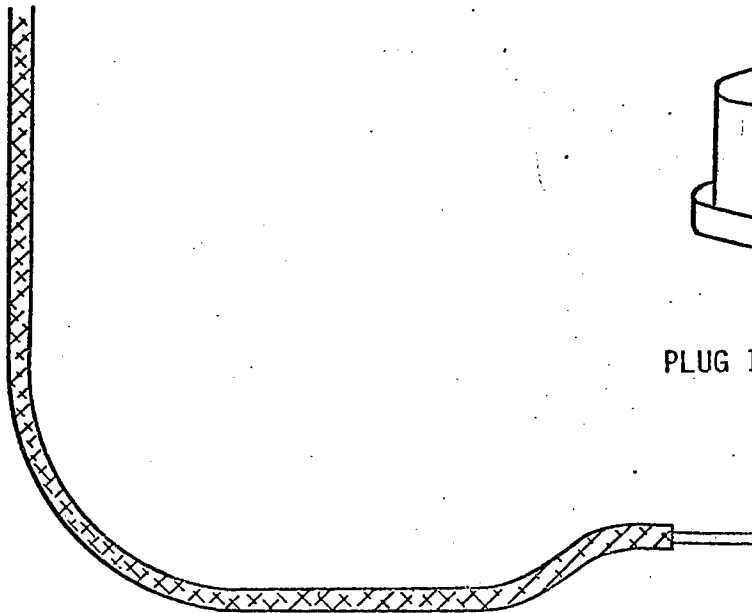
Through the use of mechanical sliprings, small motors were utilized to change the orientation of the top-mounted probes through  $360^\circ$  about their own axis while the tank is rotating. A tank mounted



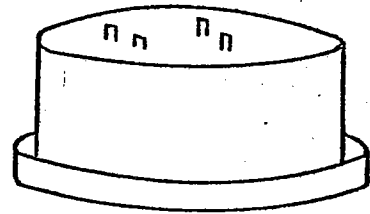
SIMPLE HOT WIRE



BOUNDARY LAYER PROBE  
WITH PROTECTOR



EXTENDED SINGLE HOT WIRE



PLUG IN HOT WIRES

FIGURE APPENDIX I.1 - PROBE DESIGNS

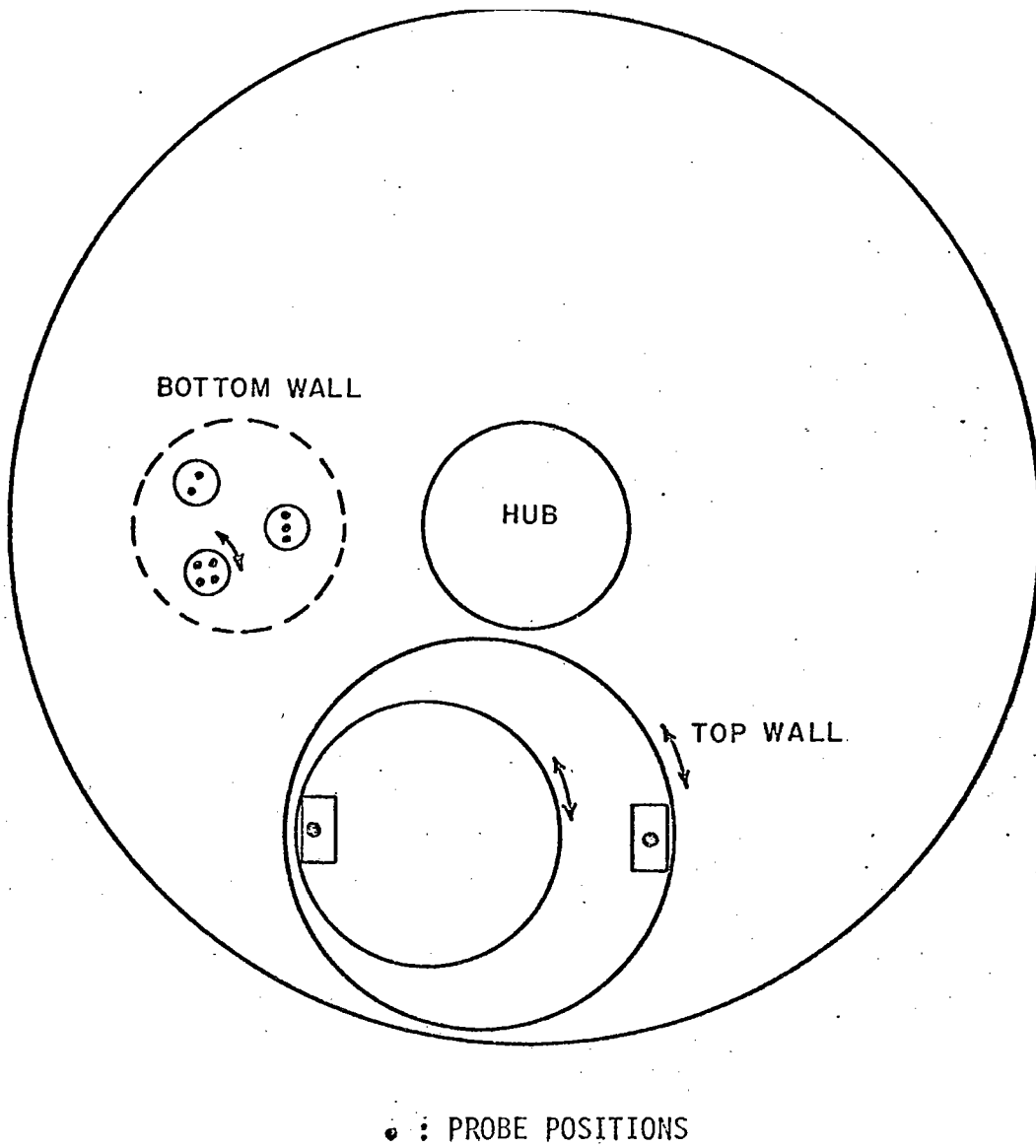


FIGURE APPENDIX I.2 - PROBE MOBILITY

potentiometer was used to measure the angular changes. In a similar fashion, the probes may be vertically raised or lowered, with the height changes measured by a trip switch, each pulse being equivalent to  $3.31 \times 10^{-3}$  mm. This allowed for a thorough examination of the vertical boundary layers, although their thickness was only of order 2mm.

The radial position of the top-mounted probes was calculated using the angular position of the probes relative to the tank surface. The two eccentric inset plates were each divided into 360 degrees, and the angular position of the inner disk relative to a reference point on the outer disk recorded. The position of the outer plate relative to the tank surface was determined by a similar technique. With this set-up, it was possible to calculate an accurate position for both probes knowing the geometrical constants of the tank and the two reference angles. Comparison of these values with those measured manually demonstrated the geometrical method to be far superior, especially at large radii. Positioning of the bottom plug-mounted probes was not amenable to this technique, although their low profile facilitated mechanical measuring. In spite of their mobility, the probes do have limitations in their relative positions. Consequently the top probes cannot occupy identical radii for certain comparative flow studies (cross-correlations). All probe sensors were self-manufactured using 9 micron tungsten wire and have typical cold resistances of order 2 ohms.

#### AI.5 Hot Wire Anemometers and Related Equipment

Throughout this work, DISA Type 55D05, battery operated constant temperature anemometers have been used. These units measured

the amount of power required to keep the probe sensor temperature constant. The forced convective heat loss by flow of air around the probe sensor was calibrated against the velocity of the incident flow. For flow speeds greater than 30 cm/sec. in air, a linear relation was found between the square of the bridge voltage (needed to keep temperature constant) and the square root of the flow velocity. In this velocity range, it was possible to calibrate the probes in a manner similar to Tatro (1966), using a large wind tunnel (figure AI.3). By observing the shedding frequency of various cylindrical rods placed in front of the sensor at different flow velocities, a calibration curve was obtained. This procedure failed in the lower velocity range frequently obtained during the present experiments. Using the basic idea of Almquist and Legath (1965), a new and different type of low velocity wind tunnel was built, as shown in figure AI.4. Essentially, a water and ethyl glycol mixture was forced by a constant pressure head into a sealed erlenmeyer flask, and the evacuated air from the flask was then passed through a number of rectifying straws and screens in a small test section. The sensor to be calibrated was positioned at the end of this section. Baffles were placed at a sizable distance around the sensor and test section to prevent extraneous flows from interfering with the forced flow. By measuring the volume of fluid deposited in the flask during a given time interval, one obtained the flow rate of air through test section. Significantly, this technique gave much more consistent calibrations for velocities of 1 cm/sec. to 100 cm/sec. than other methods. Furthermore, this technique showed that the anemometers can consistently resolve better than 1 cm/sec. in the range of 1 to 25 cm/sec. in air. According to the manufacturers, the DISA units have

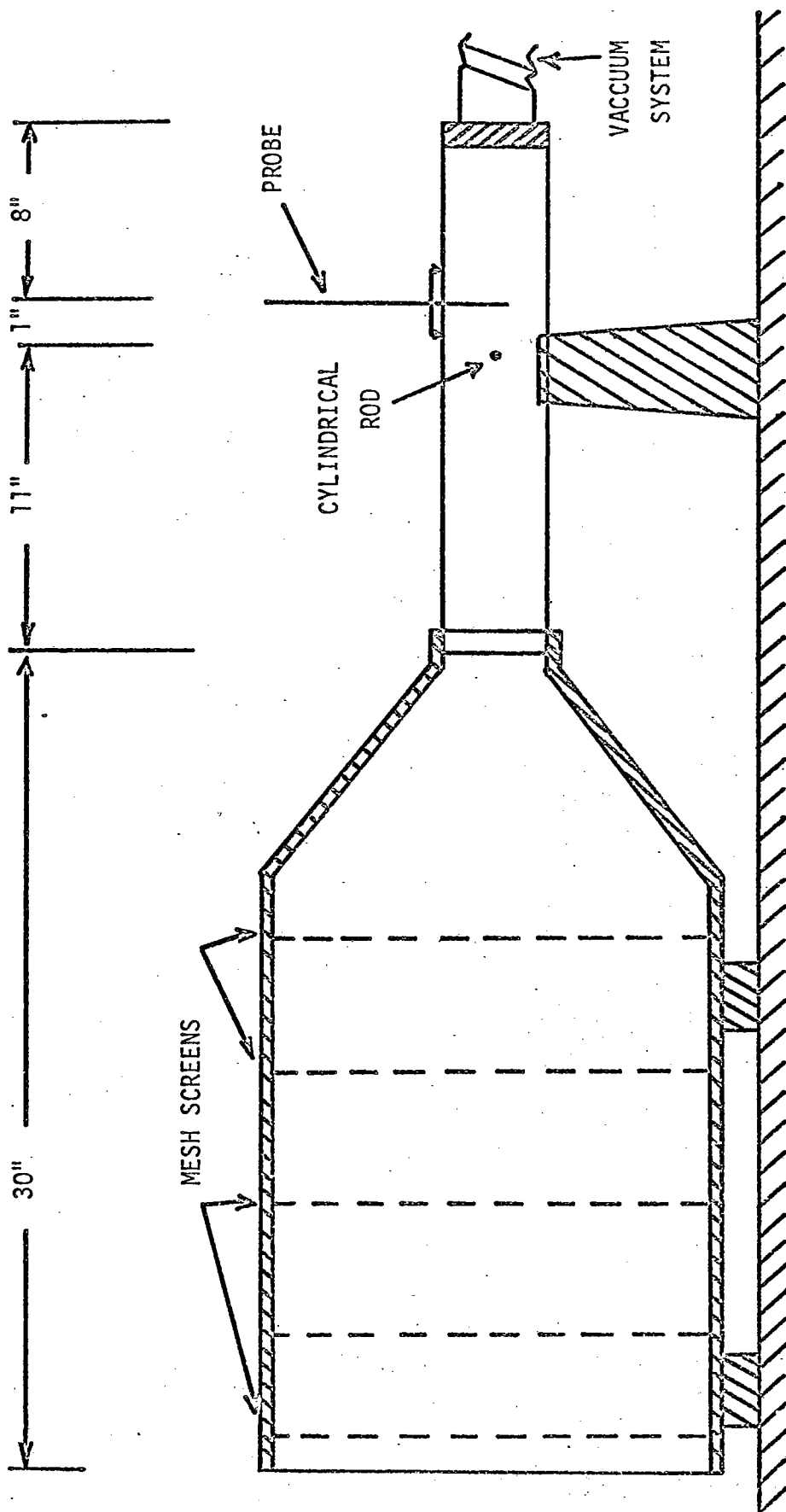


FIGURE APPENDIX I.3 - HIGH VELOCITY WIND TUNNEL

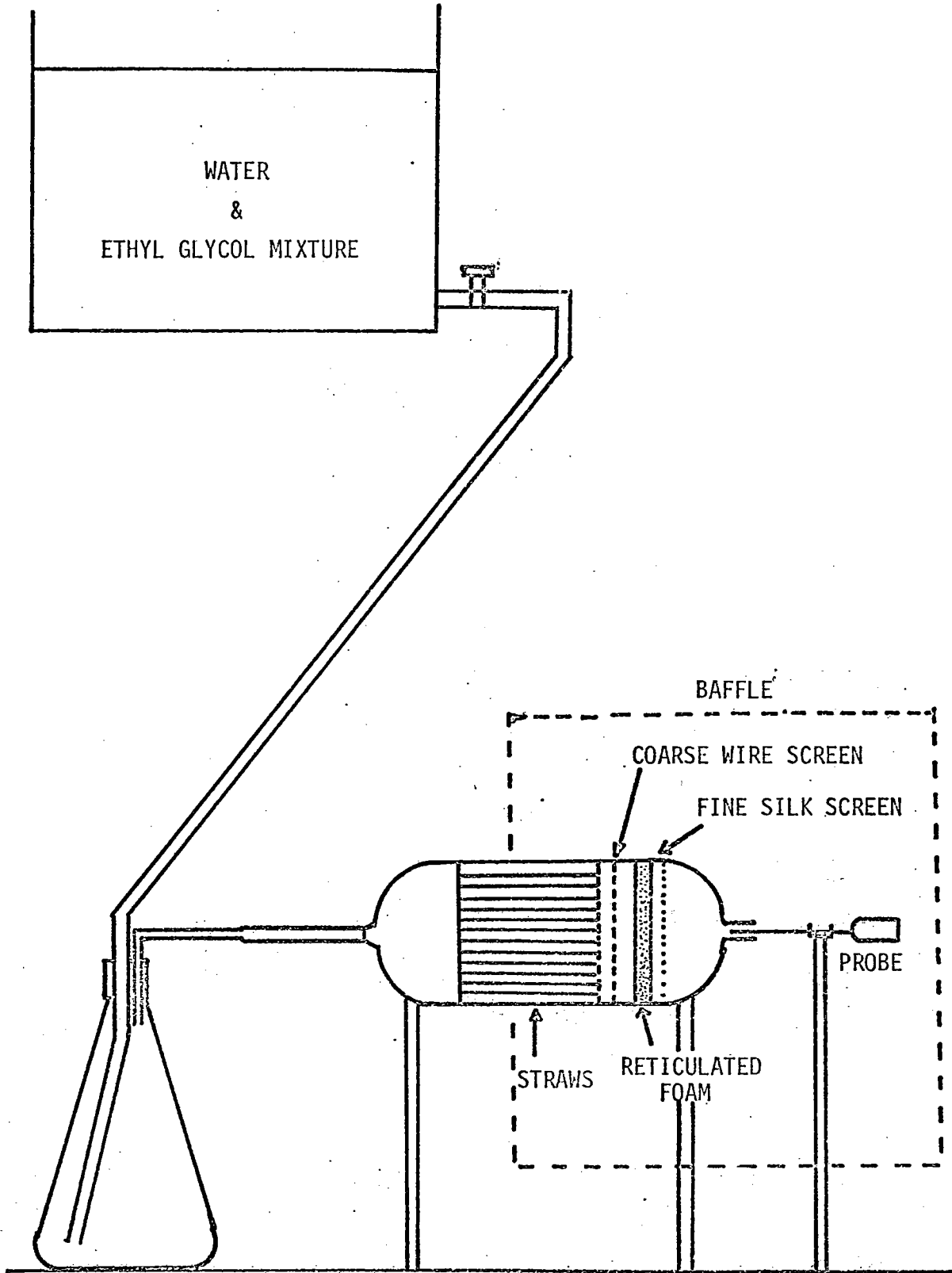


FIGURE APPENDIX I.4 - LOW VELOCITY WIND TUNNEL

an upper frequency limit in the range of 50 kHz for the configuration employed in these experiments.

A schematic representation of the equipment used was given in figure 3.2. The twelve mercury wetted sliprings (Rotocon type MKD13) were electrically noiseless (virtually), which assured that the probe signal was relayed from the rotating frame to that of the laboratory with no loss of clarity.

In order to discriminate small velocities, it was necessary that the zero velocity output of the anemometer (DC voltage) be removed prior to signal amplification. This was accomplished through the use of the bias units. Two types of DC amplifiers were used in these experiments - the Kintel model 190 (six units) and four DANA units. The former have an amplification range of 20 to 1000, whereas the latter, 30 to 1000.

#### AI.6 Auxiliary Equipment

Filters: Five simple low pass R-C filters (40 Hz) were used at the output of the amplifiers and prior to recording stage.

Two Rockwell 1010F Operational Filters were used for low frequency band pass work connected with auto- and cross-correlations.

Correlation Function Computer: The Princeton Applied Research model 101 was used, which allowed a great deal of flexibility and parameter range. Both auto- and cross-correlations were computed. The computer had a frequency range from DC to 250 Hz with an error of less than 1/2%.

Fourier Analyzer: Princeton Applied Research model 102, which



operates in conjunction with the correlation function computer to produce quadrature and co-spectra of the input waves used. The useful frequency range was dependent on the correlator setting, but was of order 0.25 to 495 Hz with less than 1% error.

Tape Recorders: An 8-Channel, Precision Instrument, Model PI-6200, magnetic tape recorder, with three recording speeds was employed. The data were read into the correlator at a speed ten times greater than that of the recording rate. The usual mode of information storage was a tape loop which contained 5 minutes (minimally) of data at the lowest recording speed (.375 inches/sec.).

Function Generator: A low-frequency function generator (Hewlett-Packard model 202A) was used to produce a Lissajous figure, for measuring the shedding frequency of the flux monitoring system for varying rates. It was also employed in calibration tests of the correlator and fourier analyzer.

Pre-Set Counter: A Universal Pre-set counter, model 2019 was used to display the rotation rate and period count, the latter being more accurate.

Oscilloscope: A Tektronix Model 502A Dual Beam Oscilloscope was used to monitor velocity fluctuations and some of the mean velocity data.

X-Y Plotter: A Mosley model 2D-2 X-Y Plotter graphed final spectra, auto- and cross-correlations, as well as the output of the extended probe versus sensor orientation.

Pen Recorder: A Sanborn Model 67-300 four channel pen recorder was used to record voltage fluctuations, transient responses, hysteresis effects, and to check for any long term D.C. drifts in the output.

## APPENDIX II

## Data Collection Methods

## AII.1 Recording of Variables

Typically, the data recorded for each experimental run consisted of the following (see also fig. AI.5),

- (a) Instantaneous voltage output of operating hot wire anemometers, each having a known overheat ratio.
- (b) Rotation rate of the tank.
- (c) Flux rate, as indicated by the "flux" hot wire.
- (d) Ambient temperature of laboratory, to be compared to calibration values.
- (e) Angular position (local coordinates) of top-mounted probes and radial position of those bottom-mounted.
- (f) Orientation of all probes relative to a perpendicularly impinging flat plane tangent to the local radius vector (by potentiometer output).
- (g) Angular separation of all probes in azimuthal direction of annulus.
- (h) Vertical separation of all sensors from the inner side of the bottom aluminum disk.
- (i) Time of measurement.

## AII.2 Mean Velocity Levels

## AII.2.1 Interior and Side-wall Layers

- (a) General characteristics: the measurements of interior flows, with fixed probes, were found to have a critical dependence on ambient temperature. To avoid this unwanted variability, a continuous profile scheme was effected.

(b) Probe location: These runs were made at a height of 12cm from the bottom (i.e., at the vertical midpoint of the tank for numerous radii. The aim was twofold: to quantify the influence of various flow configurations in altering the interior velocity structure, and to describe the side-wall layers. The usual method was to run an experiment at a constant rotation rate for a series of fluxes, and alternately at a constant flux for varying rotation. In this manner, the effect of systematically altering the Reynolds, Rossby and Taylor number could be interpreted.

(c) DC drift: For all probe calibrations and measurements, the output voltage was initially adjusted to zero for a "no flow" condition (i.e., free convection). After the completion of a run, velocity output was rerecorded to verify that no significant dc drift had occurred from the original zero position.

(d) Ambient temperature changes: The influence of ambient temperature changes on any individual series, with single fixed probes, was insignificant. The recorded differences did not exceed 0.2°C. The major difficulty came on comparing a particular series against another set, at a different radius, taken at a later time. In this case, the influence of temperature change was important for the lower velocities, obtained at the outer radii (Rasmussen, 1965). The temperature range experienced over all runs was  $\pm 1.5^\circ\text{C}$  from the mean. According

to Rasmussen, such a fluctuation can introduce changes of approximately 5-10% for the lower velocities, and a smaller difference at higher magnitudes (of velocity). These errors in the radial distribution of velocity were avoided by use of the extended single probe. This sensor allowed for complete mapping of the interior velocity field within a relatively brief time. The influence of temperature change was insignificant during each series. Obviously, the probe must always have a shaft component directed upstream to avoid any spurious wake effects.

(e) Flow direction: The interior mean velocities measured were azimuthally directed. Using a single fixed probe, numerous tests verified that the interior flow was zonal in nature, within the error bounds of the directional sensor (potentiometer). In a more definitive experiment, Tatro (1966) found the interior radial transport to be less than 2% of that predicted for the Ekman layer transport, using an annular configuration.

#### AII.2.2 Ekman layer

(a) General flow characteristics: The steady-state observations taken in the bottom boundary layer were very similar in nature to those of the interior, and thus subject to the same errors. Of course, the importance of vertical positioning in the determination of boundary layer structure was paramount. The Ekman layer

measurements differed from those in the interior, in that the velocities near the bottom of the layer were small, and secondly, the influence of an aluminum plate in close proximity to the probe caused it to respond in an anomalous fashion.

(b) Flow speeds: In a majority of experiments using constant temperature anemometers the velocities were of a much higher magnitude than those encountered presently. Figure 4 of the DISA manual (1969) shows the mean response of tungsten hot wire probe to flows at a varying angle of incidence for a flow of 3000 and one of 6000 cm/sec. On careful analysis of the response for incidence angles approaching  $\pm 90^\circ$  from the perpendicular, the output was found not to be zero, but instead 7 or 8% of the maximum output (for 3000 cm/sec and an overheat of 0.8). This response was due to a "side-wise" forced convection, and became quite influential at lower velocities. At the low speeds encountered in the boundary layer, this discrepancy may account for a "velocity" of up to 40% of the maximum value, recorded at perpendicular incidence with corrections for free convection. This effect was found by using the high-velocity wind tunnel (figure AI.3). The distortion greatly complicated the detection of the small radial component in the Ekman flow. At greater heights in the boundary layer accurate separation of the flow velocity into two directions was a critical function of probe orientation. The small angle formed with zonal

direction was difficult to estimate. For these reasons a majority of the results shown display only the azimuthal component's structure within the Ekman layer. Although it was possible to calibrate each probe for a known flow at a variety of incidence angles in the high velocity tunnel, the low velocity wind tunnel design did not allow such modifications. Thus, in the present case, the low velocities inherent in an Ekman layer were not amenable to calibration as a function of probe direction for small fluxes and/or large radii.

(c) Low speed calibration: The influence of calibrating a probe in a flow, parallel to the probe shaft (top mounted) and thereafter using the sensor to detect flows perpendicular to the holder was unimportant. The differences found by Rasmussen (1965) resulted from the impinging flow (forming various angles with respect to gravity). However, in the present case, the flow was perpendicular to the local gravitational field for all top-mounted probes, both in calibration and operation.

(d) Boundary heat losses: Another influence on recorded voltages in the boundary layer was the proximity effect of the wall. Wills (1962) made an extensive study of such effects as a function of wire diameter, overheat ratio and flow rate. In the present case, the ratio of minimum distance from the wall (leg length) to that of wire radius was 140, and for this value the influence of velocity on the corrections was negligible for

flows greater than 4.5cm/sec. Nevertheless, there was an "extra heat loss", as applied by Dryden (1936), independent of velocity. This influence was felt at distances less than 1.35mm from the plate (for an overheat of 0.7 and wire of diameter  $9\mu$ ) and was largest at the smallest heights. The normal routine for boundary layer observations included running the probe with no flux or rotation from the lowest position to a height, at which changes in apparent heat loss ceased. This correction (in voltage) was then applied to the values obtained under operating conditions. Failure to do this, resulted in an anomalous velocity structure which increased with decreasing height, as found by Green and Mollo-Christensen (1970). Since other workers have used a variety of materials as horizontal walls in their annuli, a short comparative study of the various heat losses is presented in Appendix III.

### AII.3 Wave Motion Analysis

- (a) Signal decomposition: The structure of the fluctuating component was usually complex, consisting of a number of different waves. These signals were decomposed, using an analog fourier analyzer. In these cases, the mean velocity was removed from the signal before amplifying the wave component. Using this method, spectra of wave motions for numerous Reynolds and Rossby number combinations were possible. Similar techniques were employed for readings both within

the boundary layers and the interior. For each recording, the tank was allowed to run for fifteen minutes prior to a five and a half minute recording interval. The spin-up time for the tank was of order thirty seconds. A comparison of spectra taken sequentially for the same flow, showed that after an initial period of ten minutes, the spectra were invariant with time.

- (b) External influences: External influences were significant, and their minimization was crucial for the reliability of spectra. Two prevalent disturbances were quick motions of the experimenter in close proximity to the tank and secondly, the slamming of doors and similar motions. These disturb the flows by producing an abrupt pressure fluctuation on the outer wall. None of the results in the present work were subject to these disturbances.
- (c) Cross-correlations: The signals to be cross-correlated were recorded simultaneously on an 8-track tape recorder. Subsequently, the individual signals were analyzed for their dominant wave energies as a function of frequency. Using accurate Rockwell band-pass filters, waves of a certain frequency were isolated at the various sensors and cross-correlated separately. A description of wave structure was accomplished using this technique.

#### AII.4 Transitory Experiments

In Appendix IV some spin-up and "flux-up" experiments are presented. The time required to change both rotation and flux were short in



duration (usually one second), as compared to the spin-up time ( $T_s = [H^2/\nu\Omega]^{1/2}$ , where H was tank height). The flux was altered using the vacuum motor control, whereas the rotation changes were applied through speed control brake and external mechanical means. This method was limited to "spin down to" or "spin up from" rest, both with and without a superimposed flux. The response was recorded on the four channel pen recorder, each transient being monitored at two different radii. The large inertia of the tank prevented incremental rotation changes.

#### AII.5 General Comments

The segments recorded on a tape loop over an interval of five minutes were analyzed at a speed greater than the recording rate by a factor of ten. This technique had two advantages: greater precision in filtering the signals (i.e. at higher frequencies) and utilization of the fourier analyzer at frequencies much larger than its low cut-off.

All wave traces obtained had voltage rather than velocity as ordinate. Similarly, the fourier analyzed signal was the fluctuating voltage component with the dc level removed. Although there was a non-linear relation between voltage and velocity, the wave size was sufficiently small to preclude any extraneous peaks greater than 4% of the dominant wave amplitude.

All final data were punched onto data cards for use in the IBM 360 digital computer. Both steady and unsteady results were so analyzed, and corrections applied if necessary (i.e., wall losses).

## APPENDIX III

## Wall Proximity Effects

As discussed in appendices I and II, anomalous velocity profiles were obtained when using a hot wire probe in close proximity to a solid boundary. The Exman layer results of both Tatro (1966) and Green (1968) showed this influence to be significant for vertical distances comparable to the boundary layer thickness (2 mm). In contrast, Caldwell and van Atta (1970) observed no heat losses above a height of 0.2 mm. Including the present annulus, we found that three different materials have been used as horizontal walls. Since the substances have differing thermal properties, a comparison of individual influence on a hot wire probe was made.

Table AIII-1 shows the voltage change (from zero) resulting from a hot wire probe positioned 0.64 mm from a flat piece of each test material. The relevant authors are mentioned with the appropriate wall materials.

TABLE AIII-1

Proximity Losses for Various Boundary Materials  
Arbitrary Constant Signal Amplification (X50).

$$z = 0.064 \text{ cm}$$

<u>Material</u>	<u>Voltage Change</u>	<u>Thermal Conductivity (CGS)</u>
(Air)	(0.0)	(.0006)
Plywood (Caldwell & Vanatta)	0.20	.003
Plexiglass (Tatro)	0.32	.002
Aluminum (Ingram, Green)	0.39	.500
Masonite	0.26	.001
Stone	0.44	.056

Although the plywood walls produce the least distortion of those

compared, corrections are still necessary. The most surprising result is the minor difference in losses between plexiglass and aluminum. The contrasting conductive properties of these two materials dictates a different mode of heat loss. Aluminum, being a good conductor, must take the heat away from the area immediately under the probe. On the other hand the plexiglass wall is heated locally and forms a "hot-spot". The free convection field generated by this zone distorts the velocity observations above it. From Tatro's work the influence is found to exist at a height of minimally 2 mm, even with a horizontal velocity field.

From Caldwell and van Atta's findings, it can be surmised that plywood responds in a completely different manner than plexiglass to the presence of a heated probe.

In summary, no systematic difference in heat loss is attributable to the conductive properties of the boundary wall. It should be remarked, however, that the above measurements were taken with no flow. According to Wills (1962), for the typical velocities observed, the results should not differ substantially in heat losses.

## APPENDIX IV

## Transient Response Times

Table AIV-1 shows the experimental data obtained under conditions of changing flux and rotation. The time intervals ( $\Delta T$ ) were measured between consecutive steady state interior mean flows. As a means of comparison, the spin up time (Greenspan and Howard [1963]) for each configuration is included in the chart. The arrows indicate the direction of parameter change.

TABLE AIV-1

## System Response to Step-Function Changes

Flux (cc/sec)	ROT (rad/sec)	Spin Time (sec)	$\Delta T(R=12.4'')(\text{sec})$	$\Delta T(R=18'')(\text{sec})$
0	0 $\rightarrow$ 2.70	37	40	40
0	2.70 $\rightarrow$ 0	37	56	48
902	0 $\rightarrow$ 2.70	37	25	27
902	2.70 $\rightarrow$ 0	37	64	58
1848 $\rightarrow$ 1141	2.65	38	37	39
1114 $\rightarrow$ 1848	2.65	38	37	38
1630 $\rightarrow$ 1081	3.89	31	26	29
998 $\rightarrow$ 1630	3.89	31	26	26
1526 $\rightarrow$ 941	5.52	26	24	24
1040 $\rightarrow$ 1526	5.52	26	21	20
2136 $\rightarrow$ 2410	2.65	38	24	25
1753 $\rightarrow$ 2136	2.65	38	23	23

$$\text{Spin Time} = \left( \frac{H^2}{4\Omega} \right)^{1/2} = \frac{H}{.394\Omega}^{1/2}$$

For spin up from rest, no significant difference in response time was detected at the two probe positions. With no imposed flux, the measured delay time was comparable to the spin-up time ( $T_s$ ), whereas with a constant flux, much shorter lags were observed. A much longer response time (than  $T_s$ ) was recorded in the spin down to rest experiments (no flux). The influence of an imposed flux was to increase  $\Delta T$ .

Only for low rotation and flux were the "flux-up" and "flux-down" times similar to  $T_s$ . Other combinations of the system parameters consistently gave smaller values of  $\Delta T$  (than  $T_s$ ). The observed differences are not readily related to either the Rossby or Reynolds number.

REFERENCES

Almquist, P. and E. Legath (1965): The hot wire anemometer at low air velocities. DISA Information No. 2, 3-4.

Arons, A.B., A.P. Ingersall and T. Green (1961): Experimentally observed instability of a laminar Ekman layer in a rotating basin. Tellus 13, 31-39.

Barcilon, V. (1965): Stability of Anon Divergent Ekman layer. Tellus, 17, 53-68.

Barcilon, V. (1970): Some inertial modifications of the linear viscous theory of steady rotating fluid flows. Phys. of Fluids, 13, 537-544.

Brennecke, W. (1921): Die ozeanographischen Arbeiten der Deutschen Antarktischen Expedition, 1911-1912. Arch. dt. Seewarte, 39, 208.

Brown, R. (1970): A secondary flow model for the planetary boundary layer. J. Atmos. Sci. 27, 742-757.

Busse, F. (1968) Sheer flow instabilities in rotating systems. J. Fluid Mech. 33, 577-589.

Caldwell, D. and C. van Atta (1970): Characteristics of Ekman boundary layer instabilities. J. Fluid Mech. 44, 79-95.

Chandrasekhar, S. (1961): Hydrodynamic and hydromagnetic stability. The Clarendon Press, Oxford.

Coles, D. (1965): Transition in Circular couette flow. J. Fluid Mech. 21, 385-425.

Day, C. and F. Webster (1965): Some current measurements in the Sargasso Sea. Deep Sea Res. 12, 805-814.

Dryden, H. (1936): Air flow in the boundary near a plate. NACA Tech. Report No. 562.

Dudis, J. and S. Davis (1971): Energy stability of the Ekman boundary layer. J. Fluid Mech. 47, 405-413.

Ekman, V.W. (1905): On the influence of the earth's rotation on ocean currents. Ark. Mat. Astr. FYS 2, 1-52.

- Faller, A. (1963): An experimental study on the instability of the laminar Ekman layer. J. Fluid Mech. 15, 560-576.
- Faller, A.J. and R.E. Kaylor (1966): A numerical study of the laminar Ekman boundary layer. J. Atmos. Sci. 23, 466-480.
- Ffwoos Williams, J., S. Rosenblat and J. Stuart (1969): Transition from laminar to turbulent flow. J. Fluid Mech. 39, 547-559.
- Fultz, D. (1959): A note on overstability and the elastoid-inertia oscillations of Kelvin, Solberg and Bjerkness. J. Meteorol. 16, 199-208.
- Gonella, J. (1969): Analyse des mesures de courant et de vent a la bouee-laboratoire (position B). Cahiers Ocean. 19, 855-862.
- Green, A. (1968): An experimental study of the interactions between Ekman layers and an annular vortex. Massachusetts Institute of Technology, Ph.D. thesis.
- Green A. and E. Mollo-Christensen (1970): Laboratory observations of Ekman layer flow. Dept. of Meteorology, Massachusetts Institute of Technology, Report No. 70-4.
- Greenspan, H. (1968): The theory of rotating fluids. Cambridge Univ. Press.
- Greenspan, H. (1969): On the non-linear interaction of inertial modes. J. Fluid Mech. 36, 257-264.
- Greenspan, H. and L. Howard (1963): On a time dependent motion of a rotating fluid. J. Fluid Mech. 17, 385-404.
- Gregory, N., J.T. Stuart and W.S. Walker (1955): On the stability of three dimensional boundary layers with application to the flow due to a rotating disc. Phil. Trans. A 248, 155-199.
- Gustafson, J. and B. Kullenberg (1936): Untersuchungen von Tragheitsströmungen in der Ostee. Sven. Hydr.-Biol. Kom. Sicr. Ny. Ser. XIII. Lund.
- Hide, R. (1968): On source-sink flows in a rotating fluid. J. Fluid Mech. 32, 737-764.

- Hunkins, K. (1966): Ekman drift currents in the Arctic Ocean. Deep Sea Res. 13, 607-620.
- Kelvin, Lord (1880): Vibrations of a columnar vortex. Phil. Mag. 10, 155-168.
- Knauss, J. (1965): A technique for measuring deep ocean currents close to the bottom with an unattached current meter, and some preliminary results. J. Marine Res. 23, 237-245.
- Lewellen, W.S. (1965): Linearized vortex flows. AIAA Journal 3, 91-98.
- Lilly, D.K. (1966). On the instability of the Ekman layer boundary. J. Atmos. Sci. 23, 481-494.
- Malkus, W. (1968). Precession of the earth as the cause of geomagnetism. Science 160, 259-264.
- Pollard, R.T. and R. Millard Jr. (1970): Comparison between observed and simulated wind-generated inertial oscillations. Deep Sea Res. 17, 813-821.
- Rasmussen, C. (1965): The air jet hot wire microphone. DISA Information No.2, 5-13.
- Rayleigh, Lord (1917): On the dynamics of revolving fluids. Proc. Roy. Soc. London, A 93, 148-151.
- Smith, N.H. (1945): Exploratory investigation of laminar boundary oscillations on a rotating disc. NACA Tech. Note 1227.
- Stern, M.E. (1960): Instability of Ekman flow at large Taylor numbers. Tellus 12, 399-417.
- Stewartson, K. (1957): On almost rigid rotations. J. Fluid Mech. 3, 17-26.
- Swallow, J. and G. Bruce (1966): Current measurements off the Somali coast during the southwest monsoon of 1964. Deep Sea Res. 13, 861-888.
- Tatro, P. (1966): Experiments of Ekman layer instability. Center for Space Research, M.I.T. Report No. CSR-TR-66-2.
- Theodorsen, T. and A. Regies (1944): Experiments on drag of revolving discs, cylinders and streamline rods at high speeds. NACA Report No.793.



Thompson, R. (1967): An instability of the flow in a slightly tilted rotating glass of water. Geo. Fluid Dynamics (Woods Hole Oceanographic Institution) Report No. 67-54.

Webster, F. (1963): A preliminary analysis of some Richardson current meter records. Deep Sea Res. 10, 389-396.

Wills, J. (1962): The correction of hot wire readings for proximity to a solid boundary. J. Fluid Mech. 12, 388.

BIOGRAPHICAL NOTE

The author was born in Winwick, England on February 15, 1945. After immigrating to Canada, he graduated from St. Johns High School in June, 1961. Thereafter he received a B.S. degree in physics, June, 1965, and an M.S. in marine sciences, June, 1967, from McGill University in Montreal, Canada. His master's thesis work was a model for predicting the motion of sea ice in the Gulf of St. Lawrence. In the summer of 1967, he obtained Summer Student fellowship from the Woods Hole Oceanographic Institution. The following fall, he enrolled in the Department of Meteorology, at M.I.T. In May of 1970, he married the former Beatrix Wanke.